ABSTRACT

HANSON, JACQUELINE NICOLE. Domain Patterned Ferroelectric Surfaces for Selective Deposition Via Photochemical Reaction. (Under the direction of Robert J. Nemanich.)

In this work, the use of domain patterned ferroelectric materials as a template to direct the assembly of nanostructures via photochemical reactions as well as to direct the assembly of polar molecules is presented. A distinct characteristic of ferroelectric materials is existence of a reversible spontaneous polarization. The direction of the spontaneous polarization can be reversed with the application of an electric field; thus, conductive tip atomic force microscopy (AFM) was employed to "write" nanoscale domain patterns in the ferroelectric and subsequently to visualize the configuration with piezoresponse force microscopy (PFM).

Domain patterned lithium niobate and lithium tantalate, which are known as oxygen octahedra ferroelectrics, were used as templates. These materials exhibit unique surface electronic properties resulting from screening of the bound polarization charge, which dictate local reactivity on the surface. The effect of composition (stoichiometry and doping) on photochemical reactions at the surface is explored. Depending on the composition of the material, deposition can occur on the surface of domains or domain boundaries leading to a "bottom-up" method of nanowire formation. Nanowires of various shapes and sizes can be fabricated, as these parameters are dependent only upon the underlying domain configuration. Domain specific adsorption of polar molecules is achieved by utilizing the pyroelectric nature of ferroelectric materials. Surfaces may also be passivated with these polar molecules; subsequent UV irradiation induces photodecomposition of the molecules, which results in the formation of trenches at

domain boundaries. Additionally, a scanning Kelvin probe microscopy (SKPM) study of the charge distribution on the surface of lithium niobate emphasizes the external screening mechanism and demonstrates the instability and screening of surface charges.

Domain Patterned Ferroelectric Surfaces for Selective Deposition via Photochemical Reaction

by

Jacqueline Nicole Hanson

A dissertation submitted to the Graduate Faculty of

North Carolina State University

in partial fulfillment of the requirements for the

Degree of Doctor of Philosophy

Physics

Raleigh, North Carolina

2007

APPROVED BY:

Laura I. Clarke	Alexei Gruverman
Thomas P. Pearl	Robert J. Nemanich Chair of Advisory Committee

DEDICATION

To my family.

"The astronomer may speak to you of his understanding of space, but he cannot give you his understanding.

The musician may sing to you of the rhythm which is in all space, but he cannot give you the ear which arrests the rhythm nor the voice that echoes it.

And he who is versed in the science of numbers can tell of the regions of weight and measure, but he cannot conduct you thither.

For the vision of one man lends not its wings to another man."

- Kahlil Gibran

BIOGRAPHY

Jacqueline Nicole Hanson was born on September 22, 1981 in the small town of North East, Maryland to Steven Jeff and Elaine Hanson. Twenty one months later, her brother, Jeffrey Erik, was born. Today Jacquie has two step-parents, Anthony George and Paula McGovern, and five step-siblings: Elizabeth, Anthony, Jeb, Coleman, and Forrest.

Jacquie graduated from North East High School in 1999. After high school, she attended the University of North Carolina at Wilmington in Wilmington, NC. An interest in astronomy led her to major in physics and she earned a Bachelor of Science in physics and a minor in mathematics in 2003. In 2003 Jacquie was also admitted to the graduate physics program at North Carolina State University. A few semesters later she joined the Surface Science Lab and met her future husband, Matthew Zeman. Jacquie received an en route Master of Science degree in 2006 and completed her Ph.D. in 2007.

ACKNOWLEDGEMENTS

My experience in graduate school has been a roller coaster ride, filled with ups and downs and personal growth and changes. There are many people I would like to thank for helping me along the way:

My family. Thank you for being who you are. Although you don't always agree with my decisions, you have always been there for me. Without your love and support I would not be where I am today. Erik, you have especially inspired me to keep going and to always reach my goals.

My fiancé, Matty. You are my knight in shining armor. I know that I can always count on you. Thank you for your love and your unwavering support and encouragement.

My new family, Kathy and Tracy Zeman. You have been a great source of support over the past year. I could not ask for a better mother and sister-in-law.

My girls, Nancy Santagata and Kristen Levine. I'm so glad you chose NC State, Nancy. You helped make Partners III a more bearable place. You girls were always there when I needed a friend.

Dr. Robert Nemanich, Dr. Alexei Gruverman, and Dr. Thomas Pearl. Thank you for giving me the opportunity to work in your labs and grow as a scientist. I have come a long way since the beginning when I didn't even know what an AFM was. Thank you, Dr. Pearl, for listening and for giving me your honest opinion.

My AFM labmates, Dr. Brian Rodriguez, Tom Blair and Dong Wu. Thank you for making the lab a fun environment and for all that you taught me. I will always remember your AFM/PFM quizzes, Tom. Thank you, Brian, for being a great mentor.

Cecilia Upchurch and CJ Hathorne. Thanks for all that you do for the lab. It was always nice to have another woman to chat with in a lab full of men.

Dr. Lari Jackson. Thank you for making me question my reasoning and for showing me the tools to grow and move on.

Oscar and Jackson. Thank you for giving me much needed breaks during the writing of this dissertation and in life. You always make me smile, even at times when I'm sure there is nothing to smile about.

All the members of the SSL, past and present. Thank you.

TABLE OF CONTENTS

List of Tables ix
List of Figures x

1. Introduction 1
   1.1. Motivation 1
   1.2. Overview 3
   1.3. References 4

2. Ferroelectric Materials 5
   2.1. Introduction 5
   2.2. Ferroelectricity 6
      2.2.1. Definition 6
      2.2.2. Crystal Classes 6
      2.2.3. Mathematical Background 7
   2.3. Ferroelectric Domains 13
   2.4. Surfaces 15
   2.5. Properties of Lithium Niobate and Lithium Tantalate 17
      2.5.1. Overview 17
      2.5.2. Crystal Structure 18
      2.5.3. Dependence of Properties on Crystal Composition 19
         2.5.3.1. Intrinsic Defects 20
         2.5.3.2. Extrinsic Defects (Doping) 21
         2.5.3.3. Thermal Properties 22
         2.5.3.4. Electrical Properties 23
            2.5.3.4.1. Photovoltaic Effect 24
   2.6. Summary 26
   2.7. References 27

3. Scanning Probe Microscopy 40
   3.1. Introduction 40
   3.2. Atomic Force Microscopy 41
      3.2.1. Overview 41
      3.2.2. Primary Imaging Techniques 43
         3.2.2.1. Contact Mode 43
         3.2.2.2. Non-contact Mode 45
         3.2.2.3. Tapping Mode 48
   3.3. Methods for Ferroelectric Domain Imaging 50
      3.3.1. Piezoresponse Force Microscopy 51
         3.3.1.1. Principles of PFM 51
         3.3.1.2. Applications of PFM 52
            3.3.1.2.1. Domain Imaging 53

3.3.1.2.2. Domain Writing 55
3.3.2. Electrostatic Force Microscopy 56
3.3.3. Scanning Kelvin Probe Microscopy 59
3.4. Sources of Error 60
3.5. Summary 63
3.6. References 64

4. Fabrication of Metallic Nanowires on a Ferroelectric Template via Photochemical Reaction 78
4.1. Abstract 78
4.2. Introduction 79
4.3. Experimental Details 80
4.4. Results 81
4.5. Discussion 83
4.5.1. Deposition at the Domain Boundary 83
4.5.2. The Roles of Stoichiometry and Temperature 87
4.6. Conclusion 88
4.7. Acknowledgements 89
4.8. References 90

5. Selective Photoreduction of Metallic Salt Solutions on Domain Patterned LiTaO3 and Mg:LiTaO3 97
5.1. Abstract 97
5.2. Introduction 98
5.3. Experimental Details 99
5.4. Silver Nitrate 100
5.4.1. Results 100
5.4.1.1. PPSLT 100
5.4.1.2. MgO doped PPSLT 101
5.4.2. Discussion 102
5.5. Gold Chloride 106
5.5.1. Results 106
5.5.2. Discussion 108
5.6. Conclusion 109
5.7. Acknowledgements 110
5.8. References 111

6. Investigation of the Surface Potential of Periodically Poled $LiNbO_3$ Via SKPM 120
6.1. Abstract 120
6.2. Introduction 121
6.3. Experimental Details 122
6.4. Results 123
6.5. Discussion 125
6.6. Conclusion 128
6.7. References 129

7. Selective Molecular Adsorption on a Domain Patterned Ferroelectric Template 134
7.1. Abstract.....134
7.2. Introduction.....135
7.3. Stearic Acid 136
7.3.1. Experimental Details.....136
7.3.2. Results and Discussion 138
7.4. Evans Blue Dye Molecule 141
7.4.1. Experimental Details.....141
7.4.2. Results and Discussion 142
7.5. Conclusion 143
7.6. Acknowledgments 144
7.7. References.....145

8. Summary and Future Work.....153
8.1. Summary.....153
8.2. Future Work.....154
8.2.1. $HAuCl_4$ Experiments 154
8.2.2. Deposition in a Controlled Environment 155
8.3. References.....157

LIST OF TABLES

Table 2.1 Voigt notation convention for tensor indices. 31

Table 2.2 Examples of compliances for coupling between mechanical, electric, and thermal variables. 32

Table 2.3 Summary of properties of lithium niobate and lithium tantalate. 33

Table 3.1 Specifications of cantilevers utilized in this research. 68

LIST OF FIGURES

Figure 2.1 Typical hysteresis loop of a ferroelectric material. The magnitude of the spontaneous polarization and coercive field are denoted by P_s and E_c, respectively. 34

Figure 2.2 The diagram displays the 32 crystal classes, 10 of which possess a spontaneous polarization. Whether or not a crystal is ferroelectric can only be determined experimentally. (Courtesy of Christman, 1999) 35

Figure 2.3 Schematic diagrams of ferroelectric domain configurations. The simple periodic domain structure in (a) can be found in materials with 180° domains, such as lithium niobate and barium titanate. Domains in these materials are referred to as *c* (or *z*) domains. The slightly more complicated domain structure in (b) has 90° domain wedges in a region of 180° domains. This configuration can only be found in materials in which 90° domains can form, such as barium titanate. The term "*a* domains" may also be used in reference to 90° domains. 36

Figure 2.4 Schematic diagram of screening at a ferroelectric surface. Due to the instability of polarization bound charges in the unscreened state, the surface of a ferroelectric is always screened internally and/or externally. A positive polarization bound charge is compensated by negative free carriers and adsorbed charges from the environment, while a negative polarization bound charge is compensated by positive charges, thus canceling the electrostatic instability. (After Yang *et al*. 2005.) 37

Figure 2.5 Diagram showing the band bending of a screened ferroelectric material. Internal screening of polarization bound charges creates an internal electric field near the surface, which, in turn, causes bending of the conduction and valence bands. Upward band bending occurs at the negative face (-*c*, negative polarization bound charge), while downward band bending occurs at the positive face (+*c*, positive polarization bound charge).....38

Figure 2.6 Models of the crystallographic structure and relative positions of ions in ferroelectric $LiNbO_3/LiTaO_3$. The stacking sequence of the unit cell consisting of LiO_6, NbO_6/TaO_6 and $VacO_6$ octahedra is shown in (a) (After Abrahams *et al.* 1973). The relative displacements of Li and Nb/Ta cations between oxygen planes along the c-axis are demonstrated in (b). 39

Figure 3.1 Schematic of the AFM setup. A piezoelectric scanner controls the movement of the sample and tip-sample distance. A laser beam is reflected from the back side of the cantilever to a photodetector which records the deflection of the cantilever as it moves across the sample. The data processor and feedback electronics convert the signals and generate an image of the sample surface. 69

Figure 3.2 The various geometries of cantilevers and probes are displayed. (a) and (b) are line drawings of triangular and rectangular cantilevers, respectively. SEM images

reveal the (c) conical and (d) pyramidal shapes of AFM tips. (The image in (c) is courtesy of MikroMasch and (d) of Veeco Probes.).....70

Figure 3.3 Lennard-Jones model of the potential energy of the tip-surface interaction as a function of the distance between them. As the distance between the tip and surface decreases, the tip first experiences attractive, long-range van der Waals forces and then strong, short-range forces due to the Pauli exclusion principle as it comes in "contact" with the surface. 71

Figure 3.4 Example of an amplitude versus frequency curve for an oscillating force sensor (cantilever). The resonant frequency, ω_0, of the cantilever is located at the peak of the curve where the amplitude is a maximum. In NC-AFM, the cantilever is oscillated at frequency ω_2; whereas in TM-AFM, the cantilever is oscillated at frequency ω_1.....72

Figure 3.5 Block diagram of the setup used for PFM measurements. 73

Figure 3.6 In PFM, the orientation of the spontaneous polarization in ferroelectric material can be determined from the phase difference of the piezoresponse signal. (a) The dashed blue line indicates an increase in height of the sample surface under an applied electric field (sample expands). The domain oscillating in phase with the applied voltage ($\theta = 0°$) and the polarization vector is pointing toward the bottom electrode (-*c* domain). (b) The dashed blue line indicates a decrease in height of the sample surface (sample contracts). The domain is oscillating out of phase with the applied voltage ($\theta = 180°$) and the polarization vector is pointing toward the tip (+*c* domain).....74

Figure 3.7 PFM phase images of ferroelectric domain patterns written with an AFM tip. The dark regions are positive domains and the bright regions are negative domains. The horizontal lines in (a) were written in a single domain lithium niobate sample by applying a negative bias to the –*z* surface. The pattern in (b) was written by applying positive and negative biases to a thin film PZT surface. Randomly oriented domains appear as noise in between the written domains. 75

Figure 3.8 Block diagram of the original setup used for EFM measurements (Terris *et al*., 1989). The bimorph (piezoelectric actuator) oscillates the cantilever at frequency ω_2. The first harmonic of the force gradient generates the charge signal which is used to create a map of the surface charge of the sample. The sensor used for experiments in this dissertation was a position sensitive photodiode, not an optical fiber. 76

Figure 3.9 Examples of SPM image artifacts. The double image seen in (a) is due to double tip imaging, in which the tip has two points in contact with the surface. The streaking in (b) is a result of loose debris on the surface being dragged by the tip. (c) shows a contrast in height between the domains and domain boundaries in ferroelectric lithium niobate. The contrast is not an actual topographic feature; it is the presence of strong electric fields dominating the NC-AFM force regime. 77

Figure 4.1 (a) Topographic image of the PPLN sample before deposition; (b, c) Corresponding PFM phase and amplitude images, respectively, of the PPLN sample; (d) topographic image of the same sample after deposition (inset: higher resolution topographic image illustrating the structure of the lines as formed by silver particles). ...92

Figure 4.2 (a, c, e) PFM images of domain patterns generated in the SLN sample by a conductive AFM tip. (b, d, f) Corresponding topographic images of silver nanowires fabricated by aqueous photoreduction at 80ºC. Topographic images are rotated by 30º to 45º clockwise with respect to the PFM images. The scan size in (a-f) is 15x15 μm^2. The inset in (f) shows a zoomed image of the area marked by the black block. The scan size of the inset is 2x2 μm^2. 93

Figure 4.3 Band diagrams for positive (a) and negative (b) domains in PZT demonstrating strong band bending due to a high concentration of defect states (internal screening) near the surface. LN, which has a smaller concentration of defect states, is predominantly screened externally; thus, the band bending that occurs at the surface of positive (c) and negative (d) domains is smaller than that of PZT. 94

Figure 4.4 Calculated distribution of the normal component of the electric field for the periodically poled lithium niobate at a distance of 100 nm below the surface. 95

Figure 4.5 AFM topographic images of silver formation on SLN (a, b) and CLN (c, d) after aqueous photoreduction at 25ºC (a, c) and 80ºC (b, d). 96

Figure 5.1 AFM topographic image (a) and corresponding PFM phase image (b) of the PPSLT surface prior to deposition. After photoreduction of aqueous silver nitrate, silver formation on the positive domains is visible in topographic images (c, d). 114

Figure 5.2 AFM topographic image (a) and corresponding PFM phase image (b) of the Mg doped PPSLT surface prior to deposition. After photoreduction of aqueous silver nitrate, silver formation on the positive domains is visible in topographic images (c). In the higher magnification image (d), silver formation at the domain boundaries is also apparent. 115

Figure 5.3 Band bending diagram for Mg doped PPSLT. MgO is a p-type dopant, thus there an excess of holes exists in the valence band. 116

Figure 5.4 Sequence of topographic images of the MgO doped PPLT surface after 2, 4, 8, and 10 minute (a, b, c, d, respectively) irradiation times. The images indicate that silver forms on the domain boundary first and then on the positive domains. 117

Figure 5.5 Optical microscope (a, b, and d) and AFM topographical images (c, e, and f) of gold formation on lithium tantalate surfaces. Domain specific formation of gold is evident in (b) and (c). The hexagonal (e) and triangular (f) islands that formed on the

surface with the use of 0.01 M concentration $HAuCl_4$ solution are visible with the magnification of an optical microscope (d). 118

Figure 5.6 AFM topographic image of a truncated triangular island that formed on the surface of Mg:PPSLT when a 0.01 M concentration solution of $HAuCl_4$ was used for the deposition process. 119

Figure 6.1 AFM topographic images of PPLN surfaces after the following surface treatments: solvent cleaning (a, b), TMS-Cl passivation (c) and an HF dip (d). After solvent cleaning and TMS-Cl passivation, there are no apparent surface features associated with domains and/or domain boundaries. The *–c* surface of lithium niobate is etched with HF, resulting in a height difference of ~50 nm between antiparallel domains. (Note: these images correspond to the surface potential images in Fig. 6.2.) 131

Figure 6.2 (c, d, g, h) SKPM potential images of lithium niobate surfaces after various surface treatments and (a, b, g, h) corresponding line profiles of the surface potential contrast across a domain boundary. The surface in (a, c) was passivated with TMS-Cl and (b, d) shows the surface after HF etching. The surfaces in (e, g) and (f, h) were cleaned with solvents. 132

Figure 6.3 Schematic of the screening charges on the surface of lithium niobate after solvent cleaning (a) and after passivation with TMS-Cl (b). 133

Figure 7.1 Diagram of the stearic acid vapor deposition setup. The stearic acid is melted in a small glass crucible. The PPLN sample is attached to the glass slide with double-sided tape. (Note: the objects in this diagram are not to scale.).....144

Figure 7.2 Stearic acid molecule. Due to the difference in the electronegativity of its atoms, the carboxyl group (COOH) is polar (oxygen has a net negative charge). As there are no double carbon bonds, the hydrocarbon chain is flexible.....147

Figure 7.3 Images of a PPLN surface after exposure to stearic acid vapor. Domain contrast is apparent in the optical microscope image (a). There is a gap of ~95 μm between regions of periodically poled domains which is also visible in (a). AFM topographic images (b, c) indicate there is an average height difference of ~12 nm between domains of opposite polarity. The highest magnification image (c) shows the large islands that are visible in the optical microscope image (a) are composed of smaller islands. 148

Figure 7.4 Images of a PPLN surface after exposure to stearic acid vapor. After a longer exposure time, domain contrast is no longer visible in the optical microscope image (a). The AFM topographic image in (a) shows the surface is covered with stearic acid. Domain boundaries are visible in the topographic image (c) after the stearic acid covered surface is illuminated with UV light. 149

Figure 7.5 Model of an evans blue dye molecule. This molecule has four anions (SO_3^-), making it a polyionic molecule.....150

Figure 7.6 There is no apparent domain contrast visible in the topographic image before deposition of evans blue dye molecules. After deposition, there is contrast between domains (b). The +*c* domains are ~5 nm taller than –*c* domains.....151

Figure 7.7 XPS data of evans blue dye adsorbed on positive (a) and negative (b) domains of single domain lithium niobate. 152

1. Introduction

1.1 Motivation

Almost a century has passed since J. Valasek discovered ferroelectricity in 1921.[1] Due to the complexity of the crystallographic structure of Rochelle salt, the material in which ferroelectricity was discovered, over a decade passed before any theoretical interpretation of ferroelectricity was given. Ferroelectricity was generally considered an anomaly until its discovery in barium titanate in the 1940s. Since then, the study of ferroelectric materials has been on rise and today they are used in a variety of applications including memory devices,[2] waveguides[3] and microelectromechanical systems (MEMS).[4]

Various techniques have been employed for the characterization and visualization of ferroelectric domains, many of them scanning probe microscopy (SPM) based. One of these techniques, piezoresponse force microscopy (PFM), can also be used to "write" domain patterns locally in ferroelectrics.[5] This is accomplished by applying a high enough voltage to switch the orientation of the spontaneous polarization in the vicinity of the tip. Recent studies have demonstrated the viability of this technique for generating nanoscale ferroelectric domains,[6,7] which may enable new approaches for the fabrication of nanoscale devices.

Many traditional methods for the fabrication of electronic device components utilize "top-down" photolithography-based techniques, which provide high-precision positioning and size control but are limited in downscaling by the wavelength of the

photon source. Thus, "bottom-up" approaches for nanoscale device fabrication have been introduced.[8] Recently, domain patterned ferroelectric materials have attracted attention due to the potential for surface charge associated with their spontaneous polarization to direct the assembly of nanoparticles and molecules on their surfaces.[9],[10] The ability to create nanoscale domain patterns combined with the potential for directed assembly (selective deposition) presents an exciting possibility for new bottom-up approaches toward the fabrication of complex nanostructures and nanoscale devices.

There have been several studies concerning selective deposition of nanoparticles on perovskite ferroelectrics, such as lead zirconate titanate (PZT)[9] and barium titanate,[11] but there are few reports of directed assembly on distorted oxygen octahedra ferroelectrics, such as lithium niobate (LN) and lithium tantalate (LT). Perovskite ferroelectrics and distorted oxygen octahedra ferroelectrics exhibit many differences in their properties. For example, the spontaneous polarization of lithium niobate is almost three times that of barium titanate (71 $\mu C\ cm^{-2}$ for LN vs. 25 $\mu C\ cm^{-2}$ for BTO), yet the dielectric constant of barium titanate is two orders of magnitude larger than that of lithium niobate (ε_{33} = 84 for LN vs. $\varepsilon_{33} \approx 3000$ for BTO).[12] The large magnitude of lithium niobate's spontaneous polarization makes it an attractive candidate for directed assembly, as the charge density at the surface is proportional to the magnitude of the spontaneous polarization.

The research presented in this dissertation is a study of photochemical and electrostatic deposition processes on ferroelectric surfaces, mainly lithium niobate and lithium tantalate. In order to control these processes, the mechanism by which they occur must be understood. We explore the deposition mechanisms on these materials by

varying experimental parameters such as substrate composition (stoichiometry and doping), temperature, incident photon energy, solution concentration and polarity of solvent.

1.2 Overview

The organization of this dissertation is as follows: Chapter 2 is a review of ferroelectric materials. A general overview of ferroelectrics is given in the first half of the chapter, while the second half is devoted to specific properties of lithium niobate and lithium tantalate. Scanning probe microscopy (SPM) techniques are discussed in Chapter 3, as several of these techniques were employed for imaging and characterization of the ferroelectric surfaces. In Chapter 4, metallic nanowire formation by means of a photochemical reaction on lithium niobate surfaces is demonstrated. A model to describe the formation mechanism is presented. Our model for selective photochemical deposition on lithium niobate is extended to lithium tantalate in Chapter 5. We demonstrate the effects of composition of the material (stoichiometry and doping) on the deposition process and subsequent outcome. Solution concentration and pH are also considered. Chapter 6 explores the charge distribution on the lithium niobate surface via scanning Kelvin probe microscopy (SKPM). The results emphasize the external screening mechanism of lithium niobate as well as the instability and screening of surface charge. Selective molecular adsorption is demonstrated in Chapter 7. Photodecomposition of molecules on the surface also confirms our selective photochemical deposition model. Chapter 8 provides a summary of the dissertation and a prospective of future work.

1.3 References

[1] J. Valasek, Phys. Rev. 29, 478 (1921).

[2] M. Dawber, K. M. Rabe, and J. F. Scott, Rev. Mod. Phys. **77**, 1083 (2005).

[3] F. Chen, M. Stepić, C. E. Rüter, D. Runde, D. Kip, V. Shandarov, O. Manela, and M. Segev, Opt. Express **13**, 4314 (2005).

[4] D. L. Polla and P. J. Schiller, Integrated Ferroelectrics **7**, 359 (1995).

[5] A. Gruverman, O. Auciello and H. Tokumoto, Ann. Rev. of Mat. Sci. **28,** 101 (1998).

[6] X. Zhang, D. Xue, X. Liu, and K. Kitamura, Phys. B **387**, 147 (2007).

[7] K. Terabe, M. Nakamura, S. Takekawa, K. Kitamura, S. Higuchi, Y. Gotoh, and Y. Cho, Appl. Phys. Lett. **82**, 433 (2003).

[8] C. M. Lieber, MRS Bulletin **28**, 486 (2003).

[9] S. V. Kalinin, D. A. Bonnell, T. Alvarez, X. Lei, Z. Hu, and J. H. Ferris, Nano Lett. **2**, 589 (2002).

[10] S. Dunn, D. Cullen, E. Abad-Garcia, C. Bertoni, R. Carter, D. Howorth, and R. W. Whatmore, Appl. Phys. Lett. **85**, 3537 (2004).

[11] J. L. Giocondi and G. S. Rohrer, Chem. Mater. **13**, 241 (2001).

[12] M. DiDomenico and S. H. Wemple, J. Appl. Phys. **40**, 720 (1969).

2. Ferroelectric Materials

2.1 Introduction

Ferroelectricity was discovered almost 90 years ago in 1921 when J. Valasek found the polarization of sodium potassium tartrate tetrahydrate ($NaKC_4H_4O_6 \cdot 4H_2O$), also known as Rochelle salt, could be reversed when an electric field was applied to the crystal.[1] Due to its complicated crystallographic structure (unknown at the time, the unit cell contains 112 atoms) over a decade passed before a theoretical interpretation of ferroelectricity was given. In 1945, ferroelectricity was discovered in barium titanate ($BaTiO_3$), which has a much simpler until cell consisting of only five atoms. Since then, the search for and study of ferroelectric materials has increased considerably. Today the applications of ferroelectrics are widespread, ranging from use in memory devices to microelectromechanical systems (MEMS).[2,3]

Various properties of ferroelectric materials are presented in this chapter with emphasis given to those of lithium niobate (LN) and lithium tantalate (LT). First, ferroelectricity is defined, followed by a brief description of crystal classes. Then, a condensed mathematical background of ferroelectricity is given, as descriptions of ferroelectric materials containing greater detail can be found in a number of books devoted to the subject.[4,5,6,7] Ferroelectric domains are described next, followed by a discussion of ferroelectric surfaces. The latter half of the chapter focuses on specific properties of LN and LT that are important for understanding this research. These

properties include crystal composition, which has an impact on fundamental ferroelectric characteristics, such as Curie temperature and coercive field.

2.2 Ferroelectricity

2.2.1 Definition

Ferroelectric material is both pyroelectric and piezoelectric. Like pyroelectric material, which is piezoelectric by definition, it is characterized by a spontaneous electric dipole moment (spontaneous polarization, $\vec{P}_s$) in the absence of an electric field. When stress is applied parallel to the direction of the spontaneous polarization a charge develops on the surface through the direct piezoelectric effect. Ferroelectrics are distinguished by the fact that the spontaneous polarization can be reversed with the application of an electric field with no net change in magnitude. Fatuzzo and Merz define ferroelectric material as a substance in which the relationship between the polarization direction and the applied field is not linear, but given by a hysteresis loop as displayed in Fig. 2.1.[8] Below a critical temperature, the Curie temperature (T_c), ferroelectric material exhibits ferroelectric behavior. Above the Curie temperature, a ferroelectric material enters the paraelectric phase and it no longer possesses a spontaneous polarization.

2.2.2 Crystal Classes

Depending on the geometry of their unit cells, crystals are classified into seven systems: triclinic, monoclinic, orthorhombic, tetragonal, cubic, trigonal, and hexagonal.

According to their symmetry with respect to a point, these systems are divided into 32 crystal classes, or point groups which are shown in Fig. 2.2.[9] Of the 32 classes, 11 of them have a center of symmetry, they are centrosymmetric, and cannot possess polar properties. The remaining 21 classes are noncentrosymmetric; they may have one or more polar axes and only one of them can not exhibit piezoelectricity (class 432).[5] Ten of the 20 piezoelectric classes are polar, or pyroelectric, meaning they possess a spontaneous polarization that is temperature dependent. The spontaneous polarization, which is due to a displacement between centers of positive and negative charge in the unit cell of the crystal, changes upon uniform heating and charge develops on the pyroelectric surface. All ferroelectric materials, such as LN, belong to one or another of the pyroelectric classes of materials. Whether the polarization is reversible, and therefore the material ferroelectric, can only be determined experimentally, it cannot be determined by crystal class.

2.2.3 Mathematical Background

The elastic, dielectric and thermal properties of a dielectric system, such as a ferroelectric, may be described macroscopically by three independent variables chosen from the following conjugate pairs: stress (T) and strain (S), electric field (E) and electric displacement (D), and temperature (θ) and entropy (σ). In this case (macroscopic theory), the material is treated as a continuum and the underlying atomic structure is not taken into consideration.

Strain and stress, both of which are second-rank tensors, are mechanical variables. The components of the strain tensor are given by

$$S_{ij} = \frac{1}{2}\left(\frac{\partial u_i}{\partial x_j} + \frac{\partial u_j}{\partial x_i} \right), \tag{2.1}$$

where u_i and u_j are displacement vectors and x_i and x_j are Cartesian coordinates. The diagonal components ($i = j$) of S_{ij} are referred to as normal while the off-diagonal components ($i \neq j$) are called shear. The elastic relation between stress and strain is given by

$$S_{ij} = s_{ijkl} T_{kl} \text{ or } T_{ij} = c_{ijkl} S_{kl}, \tag{2.2}$$

where T_{ij} is the stress tensor, s_{ijkl} is the elastic compliance coefficient and c_{ijkl} is the elastic stiffness constant. The compliance coefficient and the stiffness constant are fourth-rank tensors. Electric field and electric displacement (or polarization) are electrical variables. The relation between the variables in the electrical system is

$$E_i = \beta_{ij} D_j \text{ or } D_i = \varepsilon_{ij} E_j, \tag{2.3}$$

in which β_{ij} and ε_{ij} are the dielectric impermeability and dielectric constant, respectively, both of which are second-rank tensors. Finally, entropy and temperature are thermal variables. By denoting increments of entropy and temperature as $\delta\sigma$ and $\delta\theta$, the relation between them can be expressed as

$$\delta\sigma = \left(\rho C / \theta\right)\delta\theta, \tag{2.4}$$

where ρ is the density and C is the specific heat per unit mass.

Due to the symmetry property of tensors,[12] index abbreviations can be used to simplify the tensor notation. Table 2.1 lists the Voigt notation convention for index abbreviations in which the subscripts ij and kl are replaced by λ and μ, respectively.[10] The Voigt notation is used throughout this dissertation from this point forward. The

Einstein summation convention is also followed in this chapter, meaning a summation is taken for repeated indices in the same term of an equation.

Assuming the elastic, dielectric and thermal behavior of a dielectric is described by the six fields T, S, E, D, θ and σ, the first law of thermodynamics can be written as

$$dU = T_\lambda dS_\lambda + E_m dD_m + \theta d\sigma \,, \tag{2.5}$$

where U is the internal energy (per unit volume) and the subscript $\lambda = 1,\ldots, 6$ while $m = 1, 2, 3$. Since it is not always convenient to use S, D, and σ as the independent variables (as in equation 2.5), a Legendre transformation allows for a transformation of variables. The scalar functions resulting from the transformation are called thermodynamic potentials, each of which can be used to generate the equations of state.

The Gibbs free energy, another of the eight thermodynamic potentials associated with the above conjugate pairs, is given by

$$G = U - \theta\sigma - T_\lambda S_\lambda - E_m D_m \,. \tag{2.6}$$

The corresponding exact differential is

$$dG = -\sigma d\theta - S_\lambda dT_\lambda - D_m dE_m = \left(\frac{\partial G}{\partial \theta}\right)_{T,E} d\theta + \left(\frac{\partial G}{\partial T_\lambda}\right)_{E,\theta} dT_\lambda + \left(\frac{\partial G}{\partial E_m}\right)_{T,\theta} dE_m \,, \tag{2.7}$$

where the subscripts after the parentheses indicate variables that are held constant. Thus, the following equations of state are generated:

$$S_\lambda = -\left(\frac{\partial G}{\partial T_\lambda}\right)_{E,\theta} \,,\; D_m = -\left(\frac{\partial G}{\partial E_m}\right)_{T,\theta} \,,\; \sigma = -\left(\frac{\partial G}{\partial \theta}\right)_{T,E} \,. \tag{2.8}$$

The linear differential forms of the equations of state in equation 2.8 are

$$dS_\lambda = \left(\frac{\partial S_\lambda}{\partial \theta}\right)_{T,E} d\theta + \left(\frac{\partial S_\lambda}{\partial T_\mu}\right)_{E,\theta} dT_\mu + \left(\frac{\partial S_\lambda}{\partial E_n}\right)_{T,\theta} dE_n, \tag{2.9}$$

$$dD_m = \left(\frac{\partial D_m}{\partial \theta}\right)_{T,E} d\theta + \left(\frac{\partial D_m}{\partial T_\mu}\right)_{E,\theta} dT_\mu + \left(\frac{\partial D_m}{\partial E_n}\right)_{T,\theta} dE_n, \tag{2.10}$$

$$d\sigma = \left(\frac{\partial \sigma}{\partial \theta}\right)_{T,E} d\theta + \left(\frac{\partial \sigma}{\partial T_\mu}\right)_{E,\theta} dT_\mu + \left(\frac{\partial \sigma}{\partial E_n}\right)_{T,\theta} dE_n, \tag{2.11}$$

where $\mu = 1,\ldots, 6$ and $n = 1, 2, 3$. Note the indices i, j, k, l, m and n, ranging from 1 to 3, indicate the crystallographic unit vectors $\hat{x}_1, \hat{x}_2$ and $\hat{x}_3$. The equations of state, or constitutive relations, of the coupled system can now be written as

$$S_\lambda = \eta_\lambda^E \delta\theta + s_{\lambda\mu}^{E,\theta} T_\mu + d_{n\lambda}^\theta E_n, \tag{2.12}$$

$$D_m = p_m^T \delta\theta + d_{m\mu}^\theta T_\mu + \varepsilon_{mn}^{T,\theta} E_n, \tag{2.13}$$

$$\delta\sigma = \left(\rho C^{T,E}/\theta\right)\delta\theta + \eta_\lambda^E T_\lambda + p_n^T E_n, \tag{2.14}$$

where η is the thermal expansion coefficient (also denoted by α), d is the piezoelectric constant, ε is the dielectric constant, p is the pyroelectric coefficient, and s is the elastic compliance coefficient. The coefficients in equations 2.9 to 2.11 are functions of the unperturbed independent variables called compliances or coupling constants, which provide a measure of the coupling between fields. The superscripts on the compliances indicate constant variables. Some examples of couplings between mechanical and electrical variables (electro-mechanical), electric and thermal variables (electro-thermal) and mechanical and thermal variables (thermo-elastic) are given in Table 2.2. When $T_\lambda \equiv 0$ and $E_m \equiv 0$, the strain becomes the thermal expansion in zero field ($S_\lambda = \eta_\lambda(\theta)$)

and the electric displacement is equal to the spontaneous polarization at zero stress ($D_m = P_m^0(\theta)$). Note if $P_m^0(\theta) \neq 0$, the material is pyroelectric.

If the roles of temperature and entropy are ignored, the above constitutive relations yield the fundamental piezoelectric relations

$$S_\lambda = s_{\lambda\mu}^E T_\mu + d_{n\lambda} E_n, \tag{2.15}$$

$$D_m = d_{m\mu} T_\mu + \varepsilon_{mn}^T E_n. \tag{2.16}$$

In the polarization scheme,[10] equation 2.16 takes the following:

$$P_m = d_{m\mu} T_\mu + \kappa_{mn}^T E_n, \tag{2.17}$$

where P_m is the polarization and κ_{mn} is a coefficient of proportionality ($\kappa_{mn} = \varepsilon_{mn} - \varepsilon_0 = \varepsilon_0 \chi_{mn}$).[11] The fundamental piezoelectric relations demonstrate how both electric field and stress (the independent variables in this case) result in strain. Also note, if a material is not piezoelectric (the piezoelectric coefficient is zero), the fundamental piezoelectric relations reduce to the equations of state for uncoupled systems.

By expanding the Gibbs free energy in a Taylor series about equilibrium,

$$G = G_0 + \frac{\partial G}{\partial \theta}\delta\theta + \frac{\partial G}{\partial D_m} D_m + \frac{\partial G}{\partial T_\lambda} T_\lambda + \frac{1}{2}\frac{\partial^2 G}{\partial \theta^2}\delta\theta^2 + \frac{1}{2}\frac{\partial^2 G}{\partial D_m \partial D_n} D_m D_n$$

$$+ \frac{1}{2}\frac{\partial^2 G}{\partial T_\lambda \partial T_\mu} T_\lambda T_\mu + \frac{1}{2}\frac{\partial^2 G}{\partial \theta \partial D_m}\delta\theta D_m + \frac{\partial^2 G}{\partial D_m \partial T_\lambda} D_m T_\lambda + \frac{1}{2}\frac{\partial^2 G}{\partial \theta \partial T_\lambda}\delta\theta T_\lambda + \ldots, \tag{2.18}$$

non-linear (higher order) terms may be considered in addition to the linear equations described above. Just as before, the coefficients in the expansion (the partial derivatives)

are compliances. For example, electrostriction is a property of all materials in which an applied electric field produces a strain that is unchanged upon reversal of the field; hence it is a quadratic term proportional to the square of the electric field.[12] Taking into account the lowest order non-linear coupling between electric and elastic variables (electrostriction), the strain equation of state takes the form

$$S_\lambda = s^D_{\lambda\mu} T_\mu + g_{n\lambda} D_n + Q_{nk\lambda} D_n D_k \,, \tag{2.19}$$

which includes electrostrictive terms. The piezoelectric strain coefficient now has the following form:

$$\left(\frac{\partial S_\lambda}{\partial D_n}\right) = g_{n\lambda} = g^0_{n\lambda} + 2Q_{nl\lambda} D_l \,. \tag{2.20}$$

Due to the relation,

$$d_{n\lambda} = \varepsilon_{nj} g_{j\lambda} = \varepsilon_{nj} g_{n\lambda} \,, \tag{2.21}$$

the piezoelectric coefficient can also be written as follows:

$$d_{n\lambda} = d^0_{n\lambda} + 2\varepsilon_{nk} Q_{kl\lambda} D_l \,, \tag{2.22}$$

where $d^0_{n\lambda}$ is the value of the piezoelectric coefficient for infinitesimal fields.

Above the Curie temperature, the paraelectric phase of many ferroelectric materials is centrosymmetric; as such, the crystals no longer possess polar properties and the coefficients of odd-rank tensors are zero. The first non-zero electromechanical coupling term in the Gibbs free energy expansion is the following electrostrictive term:

$$Q_{\lambda ik} T_\lambda D_i D_k \,, \tag{2.23}$$

which becomes

$$Q_{\lambda ik} T_\lambda P_i P_k \tag{2.24}$$

for $E = 0$ ($D = P$). Equation 2.24 suggests there is a spontaneous strain associated with the spontaneous polarization of the following form:

$$S_s = S_\lambda = g_{i\lambda}^{\theta,T} P_i = \left(\frac{\partial G}{\partial T_\lambda} \right) = Q_{\lambda ik} P_i P_k . \tag{2.25}$$

If both $E = 0$ and $T = 0$, the compliance in equation 2.25 becomes

$$g_{i\lambda} = \left(\frac{\partial^2 G}{\partial P_i \partial T_\lambda} \right) = \frac{\partial}{\partial P_i} \left(\frac{\partial G}{\partial T_\lambda} \right) = 2 Q_{\lambda ik} P_k , \tag{2.26}$$

with piezoelectric coefficient

$$d_{j\lambda} = \varepsilon_{ij}^T g_{i\lambda} . \tag{2.27}$$

The piezoelectric coefficient for ferroelectric materials in the absence of stress and electric field, therefore, is given by

$$d_{j\lambda} = \varepsilon_{ij} Q_{\lambda ik} P_k . \tag{2.28}$$

Above the Curie temperature, where the spontaneous polarization is zero, the piezoelectric coefficient vanishes, as expected.

2.3 Ferroelectric Domains

In an ideal ferroelectric, the spontaneous polarization is uniform. Most ferroelectrics are not ideal, however, and the magnitude and direction of the spontaneous polarization is not uniform throughout ferroelectric material. Instead, the material is composed of regions that contain a large number of dipoles aligned in the same direction called domains which are separated by domain walls (or boundaries). The domain

patterns that form as the material is cooled below the Curie temperature from the paraelectric phase to the ferroelectric phase depend on many factors including the crystal symmetry, the sample geometry, the electrical conductivity, the defect structure and elastic and dielectric compliances.[4]

The total polarization in a ferroelectric has contributions from the polarizability (P_E) of the material in an electric field and the spontaneous polarization (P_s), therefore,

$$\vec{D} = \varepsilon_0 \vec{E} + \vec{P} = \varepsilon_0 \vec{E} + \vec{P}_E + \vec{P}_s \,. \tag{2.29}$$

In order to satisfy Poisson's equation, the divergence of the electric field is

$$\nabla \cdot \vec{E} = \frac{1}{\varepsilon \varepsilon_0} \left(\rho - \nabla \cdot \vec{P}_s \right), \tag{2.30}$$

where ρ is the free charge density. Because the spontaneous polarization is non-uniform (it decreases to zero at the surface of a ferroelectric material and varies near defects), the divergence of the spontaneous polarization in equation 2.30 is non-zero and acts as the source for a depolarizing field. The flow of free charge within the crystal and free charge in the surrounding medium can compensate for the depolarization field. As a ferroelectric crystal is cooled below its Curie temperature, a static domain configuration is achieved by minimizing the total free energy, which includes the depolarization energy, of the crystal. Domains form, in part, to minimize the depolarization energy of the crystal before the surface is compensated by free charges.

Since a surface charge exists when the normal component of the polarization is discontinuous across a boundary, domain walls can also generate a depolarizing field. Domains form in such a way as to minimize the energy associated with the domain walls and thus, minimize the total free energy of the crystal. Depending on the crystal

symmetry, the spontaneous polarization can occur in at least two directions resulting in a corresponding number of domain configurations. Lithium niobate and lithium tantalate, for example, have only two possible polarization orientations; hence, domain walls separate antiparallel domains and are referred to as 180° domain walls (or just 180° domains). In this case, there is no normal component of the polarization across the domain wall since the domains are antiparallel. Perovskites, such as PZT, can have 90° domains in addition to 180° domains and, therefore, six polarization orientations. Because 90° domain walls form at approximately 45° to the polarization of the neighboring domains, the normal component of the polarization is nearly continuous across the boundary. Examples of 90° and 180° domain configurations are illustrated in Figure 2.3.

There are several techniques for visualizing ferroelectric domains and domain walls. These techniques include polarization microscopy,[13] second harmonic generation microscopy,[14] chemical etching,[15] scanning electron microscopy,[16] and various scanning probe microscopy (SPM) techniques.[17,18,19,20] Piezoresponse force microscopy (PFM), electrostatic force microcopy (EFM) and scanning Kelvin probe microscopy (SKPM), all of which are SPM techniques, were used for domain imaging in this dissertation.

2.4 Surfaces

In ferroelectric materials, the discontinuity of the normal component of the polarization at the surface gives rise to a surface charge density,

$$\sigma_{pol} = \vec{P} \cdot \hat{n}, \tag{2.31}$$

in the unscreened state where $\vec{P}$ is the polarization vector and $\hat{n}$ is the unit normal to the surface. The unscreened state, however, is unstable and the surface charges induced by the polarization (polarization bound charges) must be compensated (screened).[21] Screening charges can be external, such as the adsorption of charged molecules from the environment, and they can also be internal, such as free carriers and defects in the bulk. The diagram in Figure 2.4 demonstrates screening at a ferroelectric surface, which, in general, is accomplished by combination of internal and external screening charges.[22] Positive bound polarization charge is compensated by negative internal and/or external charges, while negative bound polarization charge is compensated by positive charges, thus canceling the electrostatic instability.

As a result of the screening of the polarization bound charges, the electronic structure of the surface may be modified.[4,21] One example of this is band bending at the ferroelectric surface, as depicted in Fig. 2.5. An internal electric field is created near the surface due to internal screening of polarization bound charges, which, in turn, leads to bending of the conduction and valence bands. Upward band bending occurs at the negative face (-*c*, negative polarization bound charge) where there are positive screening charges, while downward band bending occurs at the positive face (+*c*, positive polarization bound charge). The photoelectron emission microscopy (PEEM) measurements of Yang *et al*. have confirmed band bending due to internal screening charges in ferroelectrics, as well as a variation of the electron affinity of the surface resulting from external screening charges.[22]

Measurements of surface potential by Kalinin *et al*. and Liu *et al*. have also demonstrated the presence of external screening charges on ferroelectric barium titanate ($BaTiO_3$, BTO) and lithium niobate ($LiNbO_3$, LN) surfaces.[23,24] In both materials, a surface potential contrast was observed between domains of opposite polarity. The measured potential of each domain was opposite in sign to the expected potential of the polarization bound charges; hence, the measured potential was representative of the sign of the screening charges adsorbed on the surface rather than the direction of the spontaneous polarization. With heating, the potential contrast became more apparent due to uncompensated screening charges resulting from the decrease in spontaneous polarization. In addition, the sign of the potential inverted upon cooling revealing the true sign of the spontaneous polarization (polarization bound charges), thus indicating the existence of external screening charges.

2.5 Properties of Lithium Niobate and Lithium Tantalate

2.5.1 Overview

B. Matthias and J. Remeika discovered ferroelectric properties in lithium niobate ($LiNbO_3$ or LN) and lithium tantalate ($LiTaO_3$ or LT) in 1949.[25] Since then, LN and LT have become widely used for applications such as wave guides,[26] nonlinear optical,[27] surface acoustic wave[28] and electro-optic[29] devices due to their unique properties which include transparency through a wide range of wavelengths and large piezoelectric, electro-optic and nonlinear optical coefficients. Another unique characteristic of LN and LT is the large magnitude of the spontaneous polarization they possess, which has a value of 78±3 $\mu C/cm^2$ for LN and 55±5 $\mu C/cm^2$ for LT at room temperature.[30] As stated

previously, the spontaneous polarization in a ferroelectric results in charge that must be compensated at the surface of the material; therefore, a large spontaneous polarization implies stronger electric fields and a greater amount of charge requiring compensation. Although structurally similar, LN and LT have differences that affect their responses to charge compensation and the results of selective deposition experiments.

2.5.2 Crystal Structure

Lithium niobate and lithium tantalate possess very similar crystal structures which have rhombohedral (trigonal) symmetry and belong to the point group 3*m* and space group *R*3*c* in the ferroelectric phase;[31] they are classified as oxygen octahedra ferroelectrics.[32] Although LN and LT do not have the perovskite structure, they do have the general ABO_3 formula as well as a variation of the BO_6 octahedra of perovskite ferroelectrics. The LN (LT) crystallographic frame has three types of constituent octahedra: LiO_6, NbO_6 (TaO_6) and $VacO_6$, where Vac represents a vacant site. As displayed in Fig. 2.6,[33] the stacking sequence of cations is as follows: Li^+, Nb^{5+} (Ta^{5+}), Vac, Li^+, Nb^{5+} (Ta^{5+}), Vac,… along the +*c* axis (0001). Each of the cations and vacant sites sit between planes containing triangles of O^{2-} ions, forming a hexagonal close-packed structure. The parameters of LN and LT unit cells in rhombohedral and hexagonal bases are listed in Table 2.3; note the rhombohedral unit cell contains two formula units while the hexagonal unit cell contains six formula units.[34,50]

In the paraelectric phase, LN and LT are centrosymmetric and belong to the higher symmetry point group $\bar{3}m$ and space group $R\bar{3}c$.[31] A LN (LT) crystal undergoes

a second order phase transition as it is cooled below its Curie temperature (T_C) into the ferroelectric phase and the Li and Nb (Ta) cations are displaced along the *c*-axis during this process. Because crystals cannot be centrosymmetric in the ferroelectric phase, the cations are no longer centered in the oxygen octahedra (between oxygen planes); instead, they are located off-center, with the Li ion further from center than the Nb (Ta) ion due to the difference in bond strengths (the Li-O bond is weaker than the Nb-O (Ta-O) bond).[46] The positions of the displaced ions relative to the centers of their oxygen octahedra are clearly illustrated in Fig. 2.6 (b). This displacement of ions from their symmetric positions results in the formation of a permanent electric dipole moment known as the spontaneous polarization (P_s). Due to the fact the motion of Li and Nb (Ta) cations is restricted parallel to the *c*-axis, only antiparallel (180°) domains can form in LN and LT crystals.

2.5.3 Dependence of Properties on Crystal Composition

Two common methods for growing lithium niobate and lithium tantalate are the Czochralski (CZ) technique and the double crucible Czochralski (DCCZ) technique, in which the crystal is pulled from a melt in the form of a boule.[35,36] The CZ technique is the more established of the two methods and is used commercially to grow LN and LT of congruent composition. The DCCZ method, developed by Kitamura *et al*., is a variation of the CZ method that allows for better control of the crystal stoichiometry during growth and, therefore, the production of high quality near stoichiometric crystals.

In this dissertation, the term "congruent" refers to crystals of the composition C=Li/[Li+(Nb,Ta)]~0.485, which are deficient in lithium.[37] "Stoichiometric" refers to crystals that contain equal quantities of Li and Nb/Ta (C=0.5), while "near-stoichiometric" crystals have the composition C~0.498. The abbreviation CLN/CLT is used for the congruent composition and SLN/SLT is used for crystals of stoichiometric composition; for simplicity, SLN will also be used to refer to near-stoichiometric crystals. CLN, SLN, and SLT crystals were all used in the research for this dissertation.

2.5.3.1 Intrinsic Defects

Crystals of an off-stoichiometric composition, such as CLN and CLT, have a high concentration of intrinsic defects; the total number of which depends on the Li/Nb or Li/Ta ratio. Defects in a crystal lattice can cause modification of local fields and deformation of the surrounding volume; this, in turn, influences optical and dielectric properties of the crystal as well as the switching behavior of ferroelectrics.[4,37] Although several defect models have been proposed for LN, only two will be discussed here, the Nb-site vacancy model and the Li-site vacancy model.

In the Nb-site vacancy model proposed by Peterson and Carnevale, Nb ions occupy vacant Li sites in LN and vacancies exist at the Nb sites.[38] Abrahams and Marsh confirmed this model with single crystal x-ray diffraction experiments and used the chemical formula $[Li_{1-5x}Nb_{5x}][Nb_{1-4x}Vac_{4x}]O_3$ with x=0.0118 to describe congruent LN, thus indicating Li is missing from 5.9% of relevant sites.[39] According to the model, these Li vacancy sites are always compensated by Nb resulting in niobium antisites (Nb_{Li}^{4+})

and, in order to satisfy charge compensation, 4.7% of Nb-ion sites are vacant (Nb vacancy denoted by Vac_{Nb}^{4-}).

On the other hand, the Li-site vacancy model suggests Li vacancies exist in the crystal lattice. This model has been confirmed by the neutron diffraction studies of Iyi *et al*, wherein the chemical formula $[Li_{0.95}Vac_{0.04}Nb_{0.01}]NbO_3$ is used to describe CLN.[40] Here, only 1% of vacant Li sites are filled by Nb ions creating niobium antisites (Nb_{Li}^{4+}) and the remaining 4% exist as lithium vacancies (Vac_{Li}^{-}). Although these models are somewhat contradictory, Ivanova and Yatsenko *et al.* recently concluded a combination of the two models would best explain their nuclear magnetic resonance data, suggesting both models are plausible.[41,42] Due to their structural similarities, these models are also applicable to LT defect structures.

2.5.3.2 Extrinsic Defects (Doping)

Dopants including Ti, Fe, Er, In and Mg are commonly added to LN and LT; the addition of these dopants may enhance crystal properties, such as resistance to optical damage, improving their performance in applications.[43] The manner in which dopants are incorporated into a crystal lattice has some dependence on the composition as well as the defect structure of the crystal. For example, the only sites available for dopants in the LN and LT crystallographic frames are the Li and Nb/Ta cation sites inside oxygen octahedra.[44] In the case of MgO doping, it is proposed that Mg replaces niobium antisites up to a certain concentration and then begins to replace Li cations.[45,46]

MgO (1.0 mol%) doped SLT was used in the research for this dissertation. The addition of MgO to both LN and LT crystals results in an increase of the Curie temperature and a decrease in the coercive field. Nakamura et al. found the Curie temperature of MgO 1 mol% SLT to be 695ºC (a ~5ºC increase).[47] Up to 1 mol% MgO, the coercive field of SLT decreases to a value of 6.0 kV/cm.[30] In contrast to these properties, the spontaneous polarization and refractive indices of SLN and SLT do not show dependence on the concentration of MgO.[30,47]

2.5.3.3 Thermal Properties

One of the most well known influences the composition of LN and LT has on their thermal properties is its affect on the phase transition temperature (the Curie temperature, T_C) of the crystals. Several studies have found a linear dependence between Curie temperature and LiO_2 content, resulting in the use of Curie temperature as a means to estimate the stoichiometry of LN and LT crystals.[40,48,49] For both LN and LT, T_C increases with increasing Li content; this is reflected in reported values of T_C for CLN, SLN, CLT and SLT which are 1140ºC, 1200ºC, 600ºC and 690ºC, respectively (see Table 2.3).[50]

Yao *et al*. have demonstrated the specific heat (C_p), thermal diffusivity (D) and the thermal conductivity (κ) also have higher values in SLN than CLN (see Table 2.3).[51] These properties are related by the equation

$$\kappa = \rho C_p D , \tag{2.32}$$

where ρ is the crystal density. Using ρ =4.659 g/cm^3 for CLN and ρ =4.630 g/cm^3 (at T=25ºC) for SLN and their measured values for C_p and α, they calculated the thermal conductivity to be 3.539 Wm^{-1}K^{-1} and 5.234 Wm^{-1}K^{-1} for CLN and SLN, respectively. A larger heat capacity implies a SLN crystal can absorb or lose a greater amount of heat than CLN at a certain temperature gradient, while a larger thermal diffusivity and conductivity indicate heat can diffuse through the crystal in a shorter amount of time. Since a congruent crystal has more defects than a stoichiometric crystal, the mean free path length between particle collisions is smaller in a congruent crystal; thus, the thermal conductivity has a lower value in CLN than SLN.

2.5.3.4 Electrical Properties

With a change in stoichiometry, there is a significant change in the magnitude of the coercive field (E_c) necessary for domain reversal in LN and LT crystals. Congruent compositions of LN and LT have a similar coercive field value of 210 kV/cm.[30] As the composition reaches stoichiometry, the coercive field drops by an order of magnitude to 40 kV/cm and 17 kV/cm in SLN and SLT, respectively.[30] When a domain is reversed, the Li ion must move through an O^{2-} plane to an adjacent vacant site. In the case of a niobium antisite defect (Nb_{Li}^{4+}), the Nb cation must pass through the oxygen plane upon domain reversal. Because it is more difficult for Nb to pass through the plane, a higher switching field is required.[30] Due to their higher Li content and the resulting decrease in coercive field, SLN can SLT can be poled much more easily; thus, SLN was used to create domain patterned templates via AFM for this research.

Another influence of composition on the electrical properties of LN and LT is the presence of internal fields. Gopalan and Gupta observed a large asymmetry about the electric field axis in their hysteresis loop measurements of CLN, indicating the existence of an internal electric field parallel to the polar axis.[52] The measured internal field had a value of 50 kV/cm, which is greater than the coercive field of SLN. It is possible tantalum antisites and tantalum vacancies due to Li deficiency (in analogy with the Nb-site vacancy model) align in such a way they create a dipolar defect that results in an internal field.[52]

2.5.3.4.1 Photovoltaic Effect

In ferroelectric material, illumination of a surface with light of certain photon energies results in the creation of free carriers and the subsequent development of a photovoltage.[4] Charge carriers contributing to photovoltaic current can be excited from impurity centers within the band gap and directly from the valence band to the conduction band depending on the wavelength of light that is used. The photovoltaic current in ferroelectrics is due to the asymmetry of the charge transfer process resulting from the asymmetry of the crystal lattice (displacement of ions along the polar axis) and Frank-Condon relaxation;[53,54] thus, the current develops along the polar axis.

The photoinduced current flows parallel to the *c*-axis (the polar axis) in lithium niobate and lithium tantalate. The photovoltaic current density (J_{ph}) is proportional to the intensity of the incident light (I) as expressed by the equation for photocurrent density,

$$J_{ph} = K_G \alpha I \,. \tag{2.33}$$

In equation 2.33, α is the absorption coefficient of the material at a specific wavelength and K_G is the photovoltaic constant, also known as the Glass constant, which is dependent upon the nature of the impurity center, the photon energy of the incident light and the free path length of the carrier. The resulting photoconductivity of charge carriers can be written in the following form:

$$\sigma_{ph} = e\mu_p N_p + e\mu_n N_n \,, \tag{2.34}$$

where *e* is the charge of an electron (hole), μ is the mobility and *N* is the concentration of excited electrons and holes (denoted by the subscripts *n* and *p*, respectively).

Composition influences the photovoltaic effect just as it does other key ferroelectric properties of LN and LT crystals. With increasing Li content, the photoconductivity increases in LT.[55] The photoconductivity also increases in lithium niobate (for both CLN and SLN) when crystals are doped with MgO; on the other hand, the photocurrent density decreases in LN with increased concentration of MgO.[56] It is believed defects, such as niobium/tantalum antisites, create electron traps between valence and conduction bands.[55,57] There is a decrease in the number of these internal defects as the Li/Nb or Li/Ta ratio approaches unity, as well as when a dopant is added; thus, the photoexcited free carriers may have a longer lifetime leading to a greater photoconductivity. Since the value of the space charge field depends upon the current density and conductivity ($E_{SC} = J_{ph} / \sigma_{ph}$), it also decreases with increased Li and MgO concentration.[55]

2.6 Summary

Ferroelectric materials have unique properties that can be employed in a variety of applications. The purpose of this chapter was to provide an overview of these properties beginning with a mathematical background in order to understand the results of this dissertation, which are presented in subsequent chapters. The ability to domain pattern ferroelectric material and the charges present at the surfaces of ferroelectrics are principal concepts underlying the ideas of this research; hence, ferroelectric domains and surfaces were discussed. Since lithium niobate and lithium tantalate were the primary ferroelectric materials utilized in this research, part of the chapter focused on properties specific to them. Lithium niobate and lithium tantalate have large magnitudes of spontaneous polarization, leading to a greater amount of charge requiring compensation at their surfaces. Some properties of LN and LT can be varied/enhanced with doping and/or with a change in composition of the crystal, such as the threshold coercive field necessary for domain inversion.

2.7 References

[1] J. Valasek, Phys. Rev. 29, 478 (1921).

[2] B. G. Jeon, M. K. Choi, Y. Song, S. K.Oh, Y. Chung, K. D. Suh, and K. Kim, IEEE J. Solid-State Circuits 35, 1690 (2000).

[3] D. L. Polla and P. J. Schiller, Integrated Ferroelectrics **7**, 359 (1995).

[4] M. E. Lines and A. M. Glass, *Principles and Applications of Ferroelectrics and Related Materials* (Clarendon, Oxford, 1977).

[5] W. A. Wooster, *Crystal Physics* (University Press, Cambridge, 1938).

[6] J. Grindlay, *An Introduction to the Phenomenological Theory of Ferroelectricity* (Pergamon, Oxford, 1970).

[7] J. C. Burfoot, *Ferroelectrics An Introduction to the Physical Principles*, (Van Nostrand Company, Chicago, 1967).

[8] E. Fatuzzo and W. J. Merz, *Ferroelectricity* (Wiley, New York, 1967).

[9] J. A. Christman. 1999. *Piezoelectric Measurements Using An Atomic Force Microscope*. PhD thesis, North Carolina State University, Raleigh, NC.

[10] T. Ikeda, *Fundamentals of Piezoelectricity* (Oxford, New York, 1990).

[11] J. D. Jackson, *Classical Electrodynamics* (Wiley, New York, 1999).

[12] J. F. Nye, *Physical Properties of Crystals*, (Oxford, Great Britain, 1957).

[13] W. J. Merz, Phys. Rev. **95**, 690 (1954).

[14] Y. Uesu, S. Kurimura and Y. Yamamoto, Appl. Phys. Lett. **66**, 2165 (1995).

[15] J. A. Hooton and W. J. Merz, Phys. Rev. **98**, 409 (1955).

[16] S. Zhu and W. Cao, Phys. Rev. Lett. **79**, 2558 (1997).

[17] B. D. Terris, J. E. Stern, D. Rugar, and H. J. Mamin, Phys. Rev. Lett. **63**, 2669 (1989).

[18] A. Gruverman, O. Auciello, and H. Tokumoto, J. Vac. Sci. Technol. B **14**, 602 (1996).

[19]M. Nonnenmacher, M. P. O'Boyle, and H. K. Wickramasinghe, Appl. Phys. Lett. **58**, 2921 (1991).

[20] S. V. Kalinin and D. A. Bonnell, Appl. Phys. Lett. **78**, 1116 (2001).

[21] V. M. Fridkin, *Ferroelectric Semiconductors* (Consultants Bureau, New York, 1980).

[22] W-C Yang, B. J. Rodriguez, A. Gruverman, and R. J. Nemanich, J. Phys.: Condens. Matter **17**, S1415 (2005).

[23] S. V. Kalinin, C. Y. Johnson, and D. A. Bonnell, J. Appl. Phys. **91**, 3816 (2002).

[24] X. Liu, K. Kitamura, and K. Terabe, Appl. Phys. Lett. **89**, 132905 (2006).

[25] B.T. Matthias and J. P. Remeika, Phys. Rev. **76**, 1886 (1949).

[26] E. J. Lim, M. M. Fejer, and R. L. Byer, Electron. Lett. **25**, 174 (1989).

[27] R. L. Byer, J. Nonlin. Opt. Phys. Mater. **6**, 549 (1997).

[28] J. G. Gualtieri, J. A. Kosinski, and A. Ballato, IEEE Trans. Ultrason. Ferroelectr. Freq. Control **41**, 53 (1994).

[29] Y. Q. Shi, C. Zhang, H. Zhang, J. H. Bechtel, L. R. Dalton, B. H. Robinson, and W. H. Steier, Science **288**, 119 (2000).

[30] S. Ganesamoorthy, M. Nakamura, S. Takekawa, S. Kumaragurubaran, K. Terabe, and K. Kitamura, Mater. Sci. Eng. B **120**, 125 (2005).

[31] D. A. Scrymgeour, V. Gopalan, A. Itagi, A. Saxena, and P. J. Swart, Phys. Rev. B **71**, 184110 (2005).

[32] M. DiDomenico and S. H. Wemple, J. Appl. Phys. **40**, 720 (1969).

[33] S. C. Abrahams, E. Buehler, W. C. Hamilton, and S. J. Laplaca, J. Phys. Chem. Solids **34**, 521 (1973).

[34] A. M. Prokhorov and Y. S. Kuz'minov, *Physics and Chemistry of Crystalline Lithium Niobate* (Adam Hilger, New York, 1990).

[35] H. Matthes, J. Cryst. Growth **15**, 157 (1972).

[36] K. Kitamura, J. K. Yamamoto, N. Iyi, S. Kimura, and T. Hayashi, J. Cryst. Growth **116**, 327 (1992).

[37] S. Kim, V. Gopalan, K. Kitamura, and Y. Furukawa, J. Appl. Phys. **90**, 2949 (2001).

[38] G. E. Peterson and A. Carnevale, J. Chem. Phys. **56**, 4848 (1972).

[39] S. C. Abrahams and P. Marsh, Acta Crystallogr. Sect. B **42**, 61 (1986).

[40] N. Iyi, K. Kitamura, F. Izumi, J. K. Yamamoto, T. Hayashi, H. Asano, and S. Kimura, J. Solid State Chem. **101**, 340 (1992).

[41] E. M. Ivanova, N. A. Sergeev, and A. V. Yatsenko, Kristallografiya **43**, 337 (1998).

[42] A. V. Yatsenko, E. N. Ivanova, and N. A. Sergeev, Physica B **240**, 254 (1997).

[43] D. A. Bryan, R. Gerson, and H. E. Tomaschke, Appl. Phys. Lett. **44**, 847 (1984).

[44] D. Xue, K. Kitamura, and J. Wang, J. Opt. Mater. **23**, 399 (2003).

[45] N. Iyi, K. Kitamura, Y. Yajima, S. Kimura, Y. Furukawa, and M. Sato, J. Solid State Chem. **118**, 148 (1995).

[46] O. F. Schirmer, O. Thiemann, and M. Wohlecke, J. Phys. Chem. Solids **52**, 185 (1991).

[47] M. Nakamura, S. Higuchi, S. Takekawa, K. Terabe, Y. Furukawa, and K. Kitamura, Jpn. J. Appl. Phys. **41**, L465 (2002).

[48] M. Liu and D. Xue, J. Alloys Compd. **427**, 256 (2007).

[49] M. Wohlecke, G. Corradi, and K. Betzler, Appl. Phys. B **63**, 323 (1996).

[50] V. Gopalan, N. A. Sanford, J. A. Aust, K. Kitamura, and Y. Furukawa, in *Handbook of Advanced Electronic and Photonic Materials and Devices, Vol. 4 Ferroelectrics and Dielectrics*, edited by H. S. Nalwa (Academic Press, New York, 2000).

[51] S. Yao, J. Wang, H. Liu, X. Hu, H. Zhang, X. Cheng, and Z. Ling, J. Alloys Compd. (2007).

[52] V. Gopalan and M. Gupta, Appl. Phys. Lett. **68**, 888 (1996).

[53] A. M. Glass, D. von der Linde, T. J. Negran, Appl. Phys. Lett. **25**, 233 (1974).

[54] V. M. Fridkin, *Photoferroelectrics* (Springer-Verlag, New York 1979).

[55] F. Holtmann, J. Imbrock, Ch. Baumer, H. Hesse, E. Kratzig, and D. Kip, J. Appl. Phys. **96**, 7455 (2004).

[56] Y. Furukawa, K. Kitamura, S. Takekawa, A. Miyamoto, M. Terao, and N. Suda, Appl. Phys. Lett. **77**, 2494 (2000).

[57] M. Lee, S. Takekawa, Y. Furukawa, K. Kitamura, and H. Hatano, J. Appl. Phys. **87**, 1291 (2000).

Table 2.1 Voigt notation convention for tensor indices.[10]

λ, μ	***ij, kl***
1	11
2	22
3	33
4	23, 32
5	31, 13
6	12, 21

Table 2.2 Examples of compliances for coupling between mechanical, electric, and thermal variables.[6]

Coupling	Name	Compliance
Electro-mechanical	direct piezoelectric effect	$d_{m\lambda} = \left(\frac{\partial D_m}{\partial T_\lambda} \right)_{E,\theta}$
	converse piezoelectric effect	$d_{m\lambda} = \left(\frac{\partial S_\lambda}{\partial E_m} \right)_{T,\theta}$
Electro-thermal	pyroelectric effect	$p_m = \left(\frac{\partial D_m}{\partial \theta} \right)_{T,E}$
	electro-caloric effect	$p_m = \left(\frac{\partial \sigma}{\partial E_m} \right)_{T,\theta}$
Thermo-elastic	thermal expansion	$\alpha_\lambda = \left(\frac{\partial S_\lambda}{\partial \theta} \right)_{T,E}$
	piezo-caloric effect	$\alpha_\lambda = \left(\frac{\partial \sigma}{\partial T_\lambda} \right)_{E,\theta}$

Table 2.3 Summary of properties of lithium niobate and lithium tantalate. (References for values noted in text.)

Property		**CLN**	**SLN**	**CLT**	**SLT**	**MgSLT**
Curie temperature (ºC)		1140	1200	600	690	695
spontaneous polarization ($\mu C/cm^2$)			78 ± 3	55 ± 5		
coercive field (kV/cm)		210	40	210	17	6
lattice parameters (rhombohedral)	a_R		5.494 Å		5.474 Å	
	α		55º52′		56º11′	
lattice parameters (hexagonal, Å)	a_H	5.1505	5.1474	5.1543	5.1512	
	c_H	13.8650	13.8561	13.7808	13.7736	
pyroelectric coefficient ($x10^{-5}$ C/m^2K)		4		23		
dark conductivity ($x10^{-18}$ $(\Omega cm)^{-1}$)		1			1500	
dielectric constant	ε_{11}		84		51	
	ε_{33}		30		45	
photoconductivity at 10 mW/cm^2 ($x10^{-10}$ $(\Omega cm)^{-1}$)					3	1
thermal conductivity (W/m K)		3.92	5.97			8.42
thermal diffusivity at 25□C ($x10^{-6}m^2/s$)		1.34	1.98			
specific heat at 25ºC (kJ/kg K)		0.628	0.651			
carrier mobility ($x10^{-4}$ m^2/V s)		0.74	7.4			
piezoelectric constant (pC/N)	d_{33}		6.2		8	

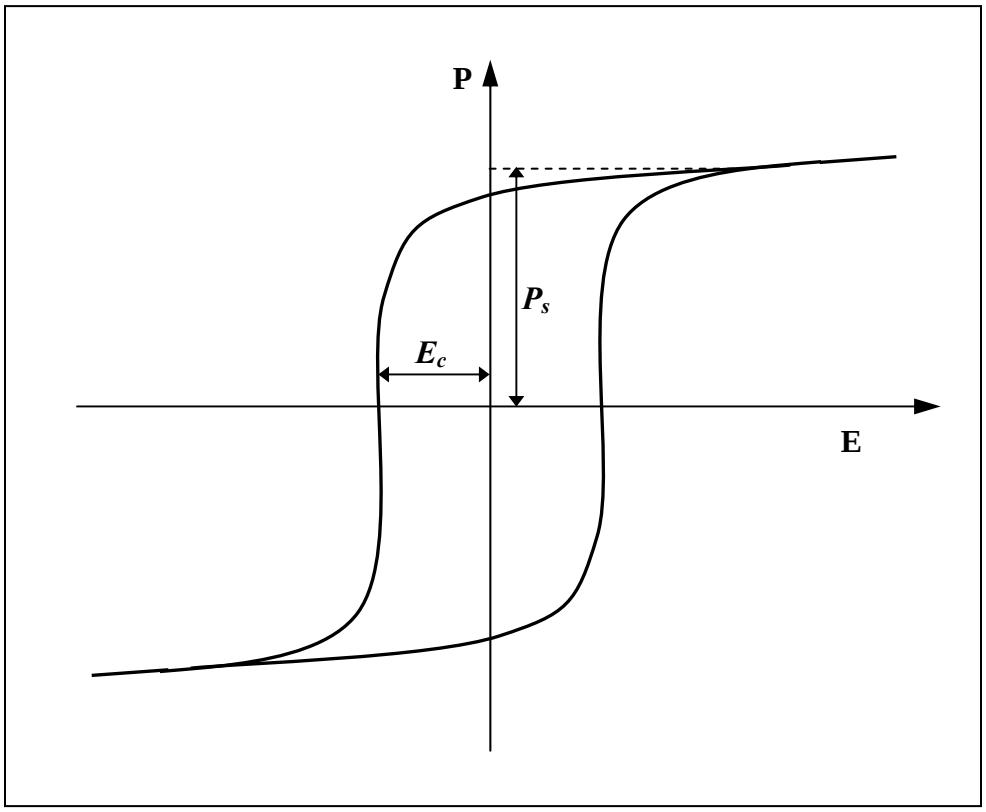


Figure 2.1 Typical hysteresis loop of a ferroelectric material. The magnitude of the spontaneous polarization and coercive field are denoted by P_s and E_c, respectively.

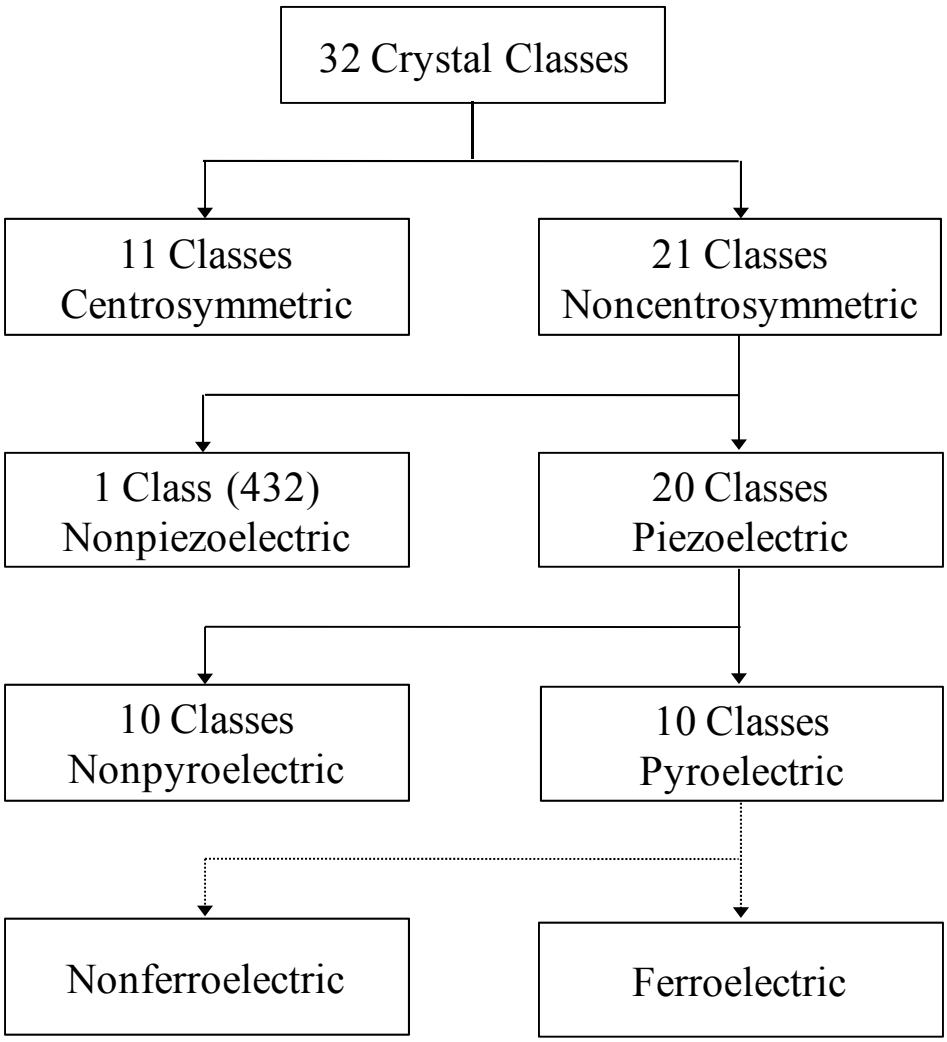


Figure 2.2 The diagram displays the 32 crystal classes, 10 of which possess a spontaneous polarization. Whether or not a crystal is ferroelectric can only be determined experimentally. (Courtesy of Christman, 1999)

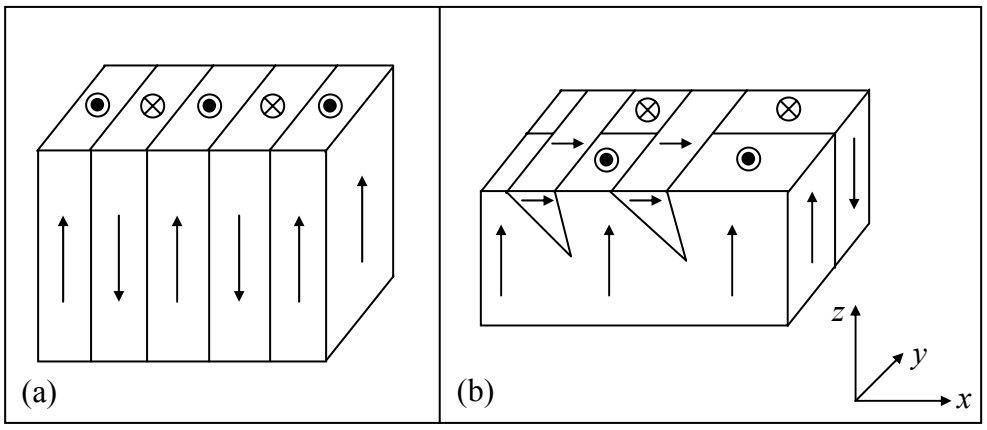


Figure 2.3 Schematic diagrams of ferroelectric domain configurations. The simple periodic domain structure in (a) can be found in materials with 180° domains, such as lithium niobate and barium titanate. Domains in these materials are referred to as *c* (or *z*) domains. The slightly more complicated domain structure in (b) has 90° domain wedges in a region of 180° domains. This configuration can only be found in materials in which 90° domains can form, such as barium titanate. The term "*a* domains" may also be used in reference to 90° domains.

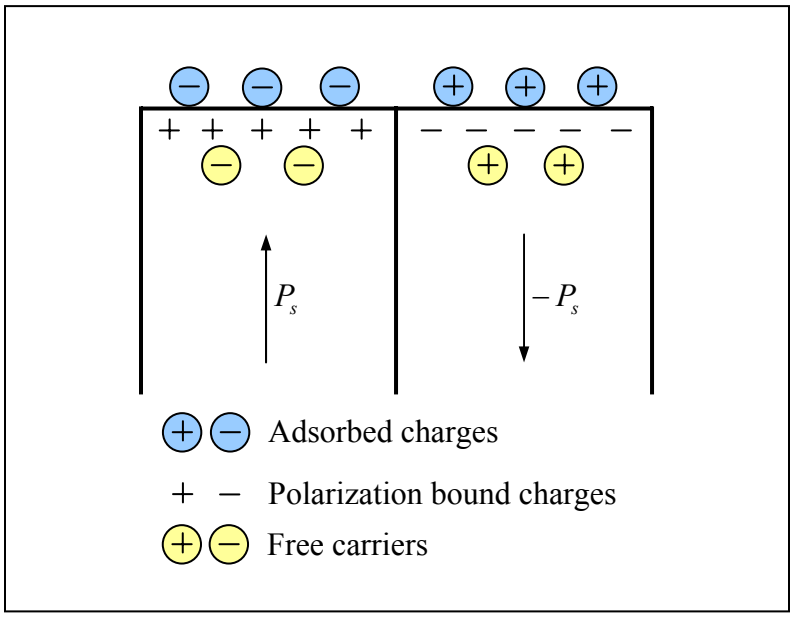


Figure 2.4 Schematic diagram of screening at a ferroelectric surface. Due to the instability of polarization bound charges in the unscreened state, the surface of a ferroelectric is always screened internally and/or externally. A positive polarization bound charge is compensated by negative free carriers and adsorbed charges from the environment, while a negative polarization bound charge is compensated by positive charges, thus canceling the electrostatic instability. (After Yang *et al*. 2005.)

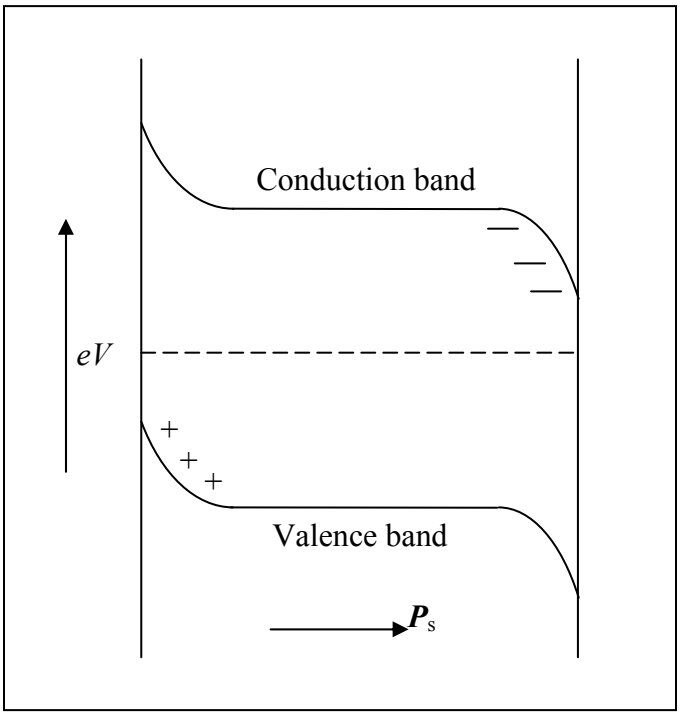


Figure 2.5 Diagram showing the band bending of a screened ferroelectric material. Internal screening of polarization bound charges creates an internal electric field near the surface, which, in turn, causes bending of the conduction and valence bands. Upward band bending occurs at the negative face (-*c*, negative polarization bound charge), while downward band bending occurs at the positive face (+*c*, positive polarization bound charge).

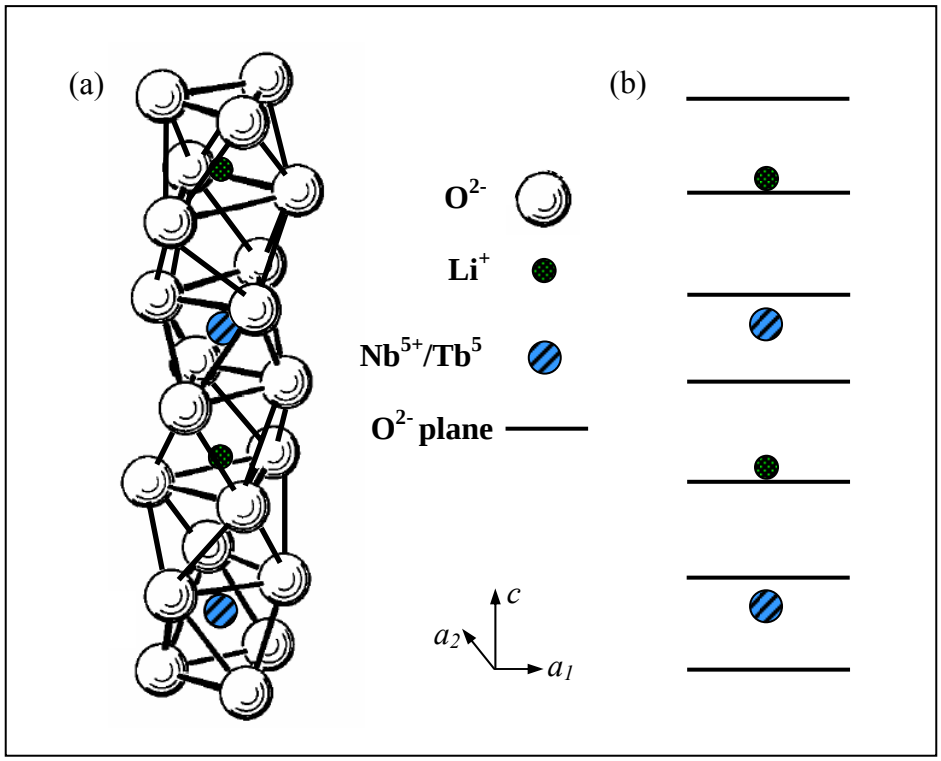


Figure 2.6 Models of the crystallographic structure and relative positions of ions in ferroelectric $LiNbO_3/LiTaO_3$. The stacking sequence of the unit cell consisting of LiO_6, NbO_6/TaO_6 and $VacO_6$ octahedra is shown in (a) (After Abrahams *et al.* 1973). The relative displacements of Li and Nb/Ta cations between oxygen planes along the c-axis are demonstrated in (b).

3. Scanning Probe Microscopy

3.1 Introduction

Since G. Binnig and H. Rohrer developed the scanning tunneling microscope (STM) in 1982,[1] scanning probe microscopy (SPM) has become a significant tool for observation and characterization in surface science technology. The STM is a surface probe capable of atomic spatial resolution which measures tunneling current as a function of position on the surface of electrically conductive material. The atomic force microscope (AFM) was created by G. Binnig, C. Quate and C. Gerber in 1986 as a method to image insulators, in addition to conductors, on an atomic scale.[2,3] Although the original function of AFM was to measure surface topography, it has extended to a variety of other surface force probing techniques including electrostatic force microscopy (EFM),[4,5,6,7,8] piezoresponse force microscopy (PFM)[9,10,11] and scanning Kelvin probe microscopy (SKPM),[12,13,14] which have all been utilized in this research.

In this chapter, SPM techniques employed for this dissertation are introduced and described. SPM is the focus of numerous books;[15,16,17,18,19,20] therefore, an extensive review is not given here and only the basics of each technique are discussed. First, an overview of AFM is given followed by an explanation of each of its primary imaging modes: contact, non-contact and tapping. These three modes of imaging are the basis for all other scanning surface force probing techniques. Next, the methods used for the visualization and control of ferroelectric domains are described. Emphasis is placed on

PFM, as it was utilized most often. Finally, sources of experimental error in these SPM techniques are discussed.

3.2 Atomic Force Microscopy

3.2.1 Overview

An AFM has three basic components: a force sensor, a scanner and a device to detect the motion of the cantilever, which are all connected to an electronic controller and a computer. Variations of these components are the foundation for all SPMs. The controller generates the electronic signals necessary to move the components of the AFM and also converts data so that it can be displayed by the computer. Specially designed computer software acquires and displays data in the form of an AFM image, which is a map of surface topography. Fig. 3.1 shows a typical AFM setup. Two AFMs were used in this research, a Park Scientific M5 (M5) and a ThermoMicroscopes CP-Research (CP-R).

The AFM force sensor consists of a microfabricated rectangular or triangular cantilever with a small tip, or probe, at one end. The probe can be conical or pyramidal in shape. The geometries of tip and cantilever shapes are displayed in Fig. 3.2. Microfabricated cantilevers are most commonly made of Si_3N_4 or Si. The backside of the cantilever (the side without the tip) is sometimes coated with a metal such as Al to increase reflectivity. The tip can also be coated with metal for use in electrical measurements, such as PFM, in which it needs to be conductive. Table 3.1 lists the properties of the SPM probes used in this research.

Movement of the tip over the surface and the tip-sample distance are controlled by the scanner which is made of a piezoelectric ceramic, such as PZT. As discussed in Chapter 2 of this dissertation, piezoelectric materials expand or contract when a voltage is applied. Since the applied voltage is proportional to the mechanical motion of the material, the scanner has precise control over lateral and vertical movements. The scanner can have two different configurations; either the tip moves and the sample is stationary or the sample is rastered and the tip is fixed. The CP-R is a sample-scanning instrument and the M5 is a tip-scanning instrument. Although a tip-scanning microscope can accommodate large samples (up to several inches in diameter), a microscope with a stationary tip is smaller and has better resolution.

There are various methods to detect the motion of the cantilever as it scans across the surface of a sample such as tunneling detection, capacitance detection, and optical interferometry. Both the CP-R and M5 use laser beam deflection ("beam bounce" deflection). The displacement of the cantilever is measured by detecting the deflection of the laser beam from the back side of the cantilever as it rasters across the sample surface. The detector in this case is a position-sensitive photodetector (PSPD) composed of four photodiodes. When the laser beam hits a photodiode, a current is generated, and a difference in intensity can be measured between the quadrants. The difference in intensity is referred to as the "error signal."

3.2.2 Primary Imaging Techniques

3.2.2.1 Contact Mode

In contact mode AFM (c-AFM), the probe is in contact with the sample surface. A map of the sample topography is created by keeping either the force between the probe and sample constant or the probe height constant. All contact mode images in this dissertation were taken in constant force mode, wherein the force is maintained by means of a feedback loop (via the controller) that applies a voltage to the piezoelectric scanner which subsequently adjusts the height of the tip/sample. Therefore, a topographic image is obtained by recording the applied voltage (in the *z* direction), not by measuring the cantilever deflection as in constant height mode.

Since the tip is within a few angstroms of the sample surface, it is acting in the repulsive force regime, as shown in Fig. 3.3, primarily under strong, short-range forces due to the Pauli exclusion principle. The interaction potential between the tip and surface can be modeled by the Lennard-Jones potential,

$$V_I(r) = 4V_0\left[\left(\frac{\sigma}{r}\right)^{12} - \left(\frac{\sigma}{r}\right)^{6}\right] = \frac{B}{r^{12}} - \frac{A}{r^{6}}, \tag{3.1}$$

with $A = 4V_0\sigma^6$ and $B = 4V_0\sigma^{12}$, which describes the interaction between two atoms. The atom separation is denoted by r and σ is a parameter that can be determined experimentally. [21] The interaction force between the tip and surface is given by $F_I(r) = -\left(\frac{\partial V}{\partial r}\right)$.

In addition to the tip-sample interaction force, there are two other forces between the probe and surface in c-AFM: forces exerted by the tip and capillary forces. The force exerted on the surface by the tip can be found using Hooke's Law,

$$F = -kd \quad , \tag{3.2}$$

where k is the force (spring) constant of the cantilever and d is the amount of tip deflection. The spring constant of the cantilever should be as low as possible so that its deflection is maximized and small forces can be detected. There is a thin layer of liquid (usually composed of water) present on surfaces in an ambient environment, sometimes referred to as a "double layer," that gives rise to a capillary force.[22,23] The capillary force, which is a strong, attractive force that tends to hold the tip in contact, is dependent on the distance of the tip from the surface.

Due to the strong repulsive forces present in contact mode, there is a possibility for larger force gradients and greater cantilever deflection than in other imaging modes. This results in images with higher resolution. The disadvantage of contact mode is that the tip and sample *are* in contact, thus both the tip and sample are at a higher risk of being easily damaged. Because the tip is essentially being dragged across the surface, it is vulnerable to lateral (shear) forces. If the tip is in contact with a very hard surface, it can become dull quickly which leads to poor image quality and the need to change tips frequently. If the sample is soft, the tip can scratch the surface, as well as pick up contaminants that will create artifacts in the image data.

3.2.2.2 Non-contact Mode

In non-contact mode AFM (NC-AFM), as the name suggests, the probe is not in contact with the sample. Instead, the probe is vibrated at a frequency between 10 and 500 kHz above the surface of the sample at a distance of tens to hundreds of Ångstroms.[24] At this distance, the tip is acting in the attractive force regime under force gradients from long-range van der Waals (VDW) and electrostatic forces between the tip and sample (see Fig. 3.3). In order to keep the frequency of vibration constant, the tip-sample separation is maintained by means of a feedback loop as the oscillating cantilever is rastered across the surface; hence, a voltage is applied to the piezoelectric scanner in response to changes in the cantilever vibration and the tip/sample height is adjusted accordingly. In this manner, a topographic image is generated from the feedback data of the scanner.

Although the Lennard-Jones potential only applies to the interaction between two atoms, a macroscopic form of the potential can be approximated by integrating the interaction across microscopic bodies. In the case of NC-AFM, a sphere is chosen to represent the tip and a plane to represent the sample surface. Now the equation for the attractive component of the potential is

$$V_A(z) = -4\pi^2 V_0 \rho_s \rho_p \sigma^5 R \frac{\sigma}{6z}, \tag{3.3}$$

and equation for the repulsive component is

$$V_B(z) = 4\pi^2 V_0 \rho_s \rho_p \sigma^5 R \frac{1}{1260}\left(\frac{\sigma}{z}\right)^7, \tag{3.4}$$

where ρ_s and ρ_p are the number densities of atoms for the sphere and plane, respectively, R is the radius of the sphere and z is the distance between the plane and sphere. Adding the two components gives the total interaction potential,

$$V_I(z) = \int_s \int_p V_I(r)\rho_s d\vec{r}_s \rho_p d\vec{r}_p = -\frac{2}{3}\pi^2 V_0 \rho_s \rho_p \sigma^5 R\left[\frac{\sigma}{z} - \frac{1}{210}\left(\frac{\sigma}{z}\right)^7\right], \tag{3.5}$$

and the interaction force can be found by taking the derivative of the potential with respect to z,

$$F_I(z) = -\frac{2}{3}\pi^2 V_0 \rho_s \rho_p \sigma^4 R\left[\left(\frac{\sigma}{z}\right)^2 - \frac{1}{30}\left(\frac{\sigma}{z}\right)^8\right]. \tag{3.6}$$

Taking the derivative again yields the force gradient,

$$F_I'(z) = \frac{4}{3}\pi^2 V_0 \rho_s \rho_p \sigma^3 R\left[\left(\frac{\sigma}{z}\right)^3 - \frac{2}{15}\left(\frac{\sigma}{z}\right)^9\right]. \tag{3.7}$$

The presence of a force gradient causes the effective force constant of the cantilever to change as follows,

$$k_{eff} = k - F_I'. \tag{3.8}$$

Here, k is the force constant of the cantilever in the absence of an interaction force. If the force constant changes, then the resonant frequency of the cantilever must also change as displayed in Fig. 3.4. From Hooke's law for simple harmonic motion, the resonant frequency, ω_0, is known to be

$$\omega_0 = \left(\frac{k}{m}\right)^{1/2}, \tag{3.9}$$

where m is the effective mass of the cantilever and tip. Thus, the resonant frequency becomes

$$\omega_1 = \omega_0\left(1-\frac{F_I'}{k}\right)^{1/2}, \tag{3.10}$$

when the tip is subject to a force gradient F_I', which is the result of substituting equation 3.8 into equation 3.9. Equation 3.10 can be approximated by

$$\omega_1 \approx \omega_0\left(1-\frac{F_I'}{2k}\right), \tag{3.11}$$

if k is large compared to F_I'.

For large values of z where the effect of the sample on the tip is negligible, the vibration amplitude of the tip, A, as a function of the frequency is a Lorentzian of the following form:

$$A = \frac{A_0(\omega_0/\omega)}{\sqrt{1+Q^2(\omega/\omega_0-\omega_0/\omega)^2}}, \tag{3.12}$$

where A_0 is the amplitude at resonance and Q is the quality factor ($Q >> 1$).[25] Fig. 3.4, an example of an A vs. ω curve, shows there is a large peak in the vibration amplitude at the resonant frequency. As can be seen from equation 3.8, an attractive force ($F_I' > 0$) will cause a decrease in the spring constant which, in turn, causes a decrease in the resonant frequency. In order to maximize the cantilever deflection and detect small force gradients, the vibration frequency of the cantilever should be chosen at the steepest part (greatest slope) of the A vs. ω curve.

In NC-AFM, the vibration of the cantilever is driven at a frequency just to the right of the resonant peak maximum (at the off-resonant frequency ω_2 in Fig. 3.4) by a piezoelectric actuator, called a "dithering piezo." A stiff cantilever (a cantilever with a high force constant) is usually chosen to reduce the tendency of the cantilever to be pulled down to the surface. Since the spring constant is high, the amplitude of the oscillation is typically small (on the order of tens to hundreds of Ångstroms) so as to keep the motion of the tip in the attractive force regime.[15]

NC-AFM is a very favorable technique for imaging "soft" samples that can be easily damaged, such as biological materials or molecules that are poorly adhered, because the tip does not come in contact with the surface. Unfortunately, attractive VDW forces are significantly weaker than contact mode forces and there is only a small range above the surface where they exist. Under ambient conditions, all or a portion of their range may be occupied by the thin layer of adsorbates (mostly water) that is present. Consequently, it is difficult to maintain the tip-sample separation necessary for NC-AFM since the cantilever can easily slip into contact with the surface due to stronger repulsive forces and capillary forces.

3.2.2.3 Tapping Mode

In intermittent contact AFM, or tapping mode (TM-AFM) as it is commonly called, the tip is oscillated in and out of contact with the surface of the sample. Hence, it is acting through both the attractive and repulsive force regimes. Similar to NC-AFM, the amplitude of the operating frequency of vibration, the "set point" amplitude, is held

constant and the scanner adjusts the tip/sample separation via a feedback loop to maintain the frequency which is typically between 10 and 500 kHz. As with c-AFM and NC-AFM, a topographic image is generated from the feedback data of the scanner.

To account for damping that occurs as the tip approaches the surface, the vibration of the cantilever is driven at a frequency just to the left of the resonant peak maximum (at the off-resonant frequency ω_1 in Fig. 3.4) by a dithering piezo. In general, a stiff cantilever with a high Q factor (~100 to 1000) is used for TM-AFM and it is oscillated with a large amplitude (on the order of tens to hundreds of nanometers).[26] This guarantees the tip has enough energy to overcome attractive forces, such as capillary forces, and is able to tap in and out of the contaminant layer on the sample surface. Vibrating a stiff, high Q factor cantilever with a large amplitude also ensures that the energy of the probe oscillation is much higher than the energy that is lost when the tip strikes the surface.

As stated earlier, the force exerted by the tip on the sample when it strikes the surface is given by Hooke's law,

$$F = k\Delta A, \tag{3.13}$$

where k is the force constant of the cantilever and ΔA is the amplitude change in one cycle of oscillation. The change in amplitude during one cycle of oscillation can be approximated with the formula

$$\Delta A = \frac{\left(A_0 - A_s\right)}{Q}, \tag{3.14}$$

where A_0 and A_s are the free amplitude the set point amplitude, respectively. If, for example, k = 5 N/m, Q = 100 and $A_0 - A_s = 10$ nm, the force per strike is approximately 0.5 nN. This is much smaller than the force exerted by the tip in contact mode AFM, which can be ~100 nN.[16]

Tapping mode has many advantages over contact and non-contact mode AFM. Frictional shear forces are avoided and the force exerted by the tip on the sample can be up to three orders of magnitude lower than in contact mode; thus, the risk of damage to the tip and sample surface that is prevalent in c-AFM is greatly reduced in TM-AFM. This makes tapping mode ideal for imaging soft samples. The cantilever in tapping mode operates in a larger range (with a larger amplitude of oscillation) above the sample surface and with greater energy than in NC-AFM. High resolution images can be obtained since the cantilever is able to tap in and out of the water layer on the surface.

3.3 Methods for Ferroelectric Domain Imaging

Ferroelectric material, which is inherently piezoelectric, possesses a reversible spontaneous polarization. The existence of a spontaneous polarization gives rise to polarization bound surface charge and screening charge at the surface that can vary in magnitude and sign. These surface charges exert electrostatic forces on the tip that can be measured via electrostatic force microscopy (EFM)[27] and scanning Kelvin probe microscopy (SKPM)[12] to generate an image with information about the ferroelectric domains. Piezoelectric properties that provide information about domain structure can be measured via piezoresponse force microscopy (PFM).[9] PFM can also be used to reverse

the spontaneous polarization and create domain patterns. These techniques provide a way to non-destructively visualize ferroelectric domains in which the domain measurement is independent of the surface topography. All three domain imaging methods were utilized for this dissertation, but emphasis will be placed on PFM, as it was used most often. Both microscopes, the CP-R and M5, are configured for EFM, PFM and SKPM.

3.3.1 Piezoresponse Force Microscopy

3.3.1.1 Principles of PFM

In recent years, piezoresponse force microscopy (PFM) has become the most commonly used SPM technique for imaging ferroelectric domains due to its high resolution and relative ease of implementation.[28] PFM is based on the detection of sample deformation induced by an applied modulation voltage (a result of the converse piezoelectric effect) via a conductive AFM tip. The electrically driven probe is operated in contact mode; hence, the probe in PFM is acting predominantly in the repulsive force regime under short-range forces between the tip and sample. The piezoresponse signal that is generated is used to characterize the piezoelectric (and ferroelectric) properties of the sample material. Topographic information and piezoresponse amplitude (also called magnitude) and phase data are obtained simultaneously in PFM.

There are two main approaches to exciting piezoelectric vibrations (sample deformation) in the sample in PFM. In one approach, the modulation voltage is applied through a conductive tip or external probe to a top electrode that has been deposited on the surface of the sample. The sample is referred to as a capacitor in this method. When

the bias is applied, a homogenous electric field is generated in the material below the top electrode which is much larger in size than the contact area between the tip and sample. Since the piezoelectrically excited region is large, mechanical constraint due to nearby unexcited regions is minimized. The homogeneous field and large piezoelectrically excited area allow quantitative information about piezoelectric and ferroelectric properties of the sample to be measured. One drawback to this method is that it measures the bulk piezoelectric effect and as a result, the measurements represent an average. A top electrode was not used for PFM data acquired in this research.

In the second approach, which is the method used for this research, the modulation voltage is applied through a conductive tip directly to the bare surface of the sample. In this manner, piezoelectric vibrations are generated locally and a correlation can be established between the microstructure and the piezoresponse and domain configurations of the material. This approach can also be used for the investigation and reversal of individual domains as well as nanoscale domain patterning. On the other hand, due to the inhomogeneous field generated by the tip and mechanical constraint from nearby unexcited regions, it is difficult to obtain accurate quantitative information about field dependent parameters, such as the piezoelectric coefficient. Figure 3.5 shows an experimental PFM setup.

3.3.1.2 Applications of PFM

PFM was originally developed to locally measure the amplitude and phase of piezoelectric surface vibrations.[29,30] It was quickly realized that ferroelectric domains could be reversed utilizing the PFM technique and PFM was extended to ferroelectric

domain patterning (writing) with applications such as high-density data storage[31,32] and ferroelectric lithography.[33,34] PFM has also been applied for local hysteresis loop spectroscopy[35,36] and the study of domain switching dynamics.[37,38] Only out-of-plane polarization could be imaged initially, until an approach to image in-plane polarization, known as lateral PFM (LPFM), was developed by Eng, *et al*.[39] LPFM subsequently led to three-dimensional PFM and the reconstruction of polarization and the investigation of switching in ferroelectrics in three dimensions.[40,41] The applications of PFM employed for this dissertation were imaging and domain patterning of ferroelectric material, which are described below. PFM domain imaging was used to visualize ferroelectric domains in as received samples as well as patterns written via the PFM technique in ferroelectric samples.

3.3.1.2.1 Domain Imaging

In PFM, an electrical bias is applied between a conductive probe and the bottom electrode of a sample. The bias can be applied to either the tip or to the bottom electrode (or the backside of the sample if there is no bottom electrode). In all of the data recorded for this dissertation, the bias was applied to the tip while the bottom electrode was grounded. The total voltage applied to the tip is

$$V_{tip} = V_{dc} + V_{ac} = V_{dc} + V_0 \cos(\omega t), \tag{3.15}$$

where V_{dc} is the dc component of the tip bias and V_{ac} is the modulation (imaging) voltage. In general, a dc bias does is not necessary for ferroelectric domain imaging. Through the converse piezoelectric effect, when a bias is applied to a piezoelectric

material, it will expand or contract due to the production of a field-induced strain; thus, the applied bias creates an alternating electric field which results in a corresponding displacement of the sample surface at the modulation frequency. In order to avoid cross-talk between topography and piezoresponse data, the ac bias is operated at a greater frequency than the AFM feedback loop response frequency but less than the resonant frequency of the cantilever.

The displacement of the sample (change in the sample thickness) results in a deflection of the cantilever that is converted into an electrical signal called the piezoresponse signal. The piezoresponse signal is detected as the first harmonic component of the cantilever deflection, which is given by

$$d = d_0 + A\cos(\omega t + \theta), \tag{3.16}$$

where A is the piezoresponse amplitude and θ is the phase difference between the modulation voltage and the piezoresponse. If the cantilever deflection is entirely due to sample displacement as a result of the converse piezoelectric effect (there is no contribution from electrostatic and/or capacitive forces),[28,42] the longitudinal piezoelectric coefficient can be calculated using the piezoresponse amplitude,

$$d_{33} = \frac{A}{V_0}. \tag{3.17}$$

The piezoresponse amplitude should be equal for domains of opposite polarity, while it is zero at the domain boundary.

The orientation of the spontaneous polarization can be determined from the phase difference as follows (assuming a positive tip bias): if the sample expands, it is oscillating

in phase with the applied voltage ($\theta = 0°$) and the polarization vector is pointing toward the bottom electrode. If the sample contracts, it is oscillating out of phase with the applied voltage ($\theta = 180°$) and the polarization vector is pointing toward the tip. Therefore, positive domains appear dark and negative domains appear bright in PFM phase images. Figure 3.6 demonstrates the response of out-of-plane ferroelectric domains to the electric field from the modulation bias. If a domain is oriented parallel to the surface, it will appear as noise in phase images. LPFM, however, can detect in-plane polarization by measuring the torsional vibration of the cantilever due to piezoelectric shear deformation of the sample.[39]

3.3.1.2.2 Domain Writing

What makes ferroelectric material distinct is the fact that its spontaneous polarization is reversible under an applied electric field. It is possible to reverse (switch) the polarization if the following conditions are met: (1) the magnitude of the applied field is greater than the coercive field of the material and (2) the direction of the applied field is parallel to and opposite that of the region to be switched. This unique property allows domain patterns to be written in ferroelectric material via the PFM technique, as described in the previous section. The total voltage applied to the tip in PFM is a sum of ac and dc components (equation 3.15); however, an ac modulation voltage is not necessary for domain writing since the electric field should not be oscillated.

Patterns of any desired shape or form can be created if the appropriate software and/or electronics are available. Conversely, the size of a pattern is limited by factors such as domain wall width, grain size and the x-y range of the scanner. The largest scan

size for both AFMs used in this research, the M5 and the CP-R, is 100 μm x 100 μm; consequently, the maximum area that can be switched during a scan is 100 x 100 μm^2. Figure 3.7 shows PFM phase images of regions of ferroelectric samples (single crystalline SLN and thin film PZT) in which domains have been written. For samples that possess randomly oriented domains, such as PZT, a large area must be poled in one direction first; then a domain pattern of opposite polarization can be written in the pre-poled area. The same conductive tip is used to create domain patterns and subsequently image them.

3.3.2 Electrostatic Force Microscopy

Electrostatic force microscopy (EFM) is a non-contact technique that is used to map the electrostatic force between a tip and sample. The conductive probe is acting in the attractive force regime under force gradients from long-range Coulomb forces. There are two methods of measuring the surface charge. In one method, called "interleave" or "lift" mode, topography and electrostatic force are measured independently in two steps.[43] First, the tip scans one line in tapping mode to acquire topographic information. Next, the tip is raised a predetermined height above the surface and scans a line parallel to (and directly above) the first line to acquire information from the electrostatic interaction between the tip and sample. In the second method, which was developed by Terris *et al*. and is the method used for this dissertation, non-contact topographic and electrostatic images are obtained simultaneously.[7,8] A diagram of the setup for the second method is displayed in Fig. 3.6

Coulomb's law for the force between two point charges, in this case the tip and sample, has the form

$$F_{coul} = \frac{q_s q_t}{4\pi\varepsilon_0 z^2}, \tag{3.18}$$

where ε_0 is the permittivity of free space, z is the distance between the charges and q_t and q_s are the charge on the tip and sample, respectively. In addition to the Coulomb force, there are also capacitive forces from external ac and dc voltages that are applied between the tip and sample during EFM, V_{dc} and $V_{ac} = V\ \sin(\omega t)$. Here, the frequency ω is greater than the frequency of the feedback loop that controls the movement of the scanner, but much lower than ω_2, the frequency of the tip oscillation. The sum of the capacitive forces, with capacitance C and surface potential V_s, is

$$F_{cap} = \frac{1}{2}\frac{\partial C}{\partial z}\left(V_{dc} + V_{ac} - V_s\right)^2. \tag{3.19}$$

The total force on the tip is then

$$F_z = F_{coul} + F_{cap} = \frac{q_s q_t}{4\pi\varepsilon_0 z^2} + \frac{1}{2}\frac{\partial C}{\partial z}\left(V_{dc} + V_{ac} - V_s\right)^2, \tag{3.20}$$

with total charge

$$q_t = -q_s + q_{dc} + q_{ac} = -q_s + CV_{dc} + CV_{ac}. \tag{3.21}$$

After substituting the expression for the total charge into equation 3.17 and taking the derivative of the result, we find the force gradient can be separated into three components: a static, or dc, component

$$F'_{dc} = \frac{q_s}{2\pi\varepsilon_0 z^3}\left[q_s - CV_{dc} + \frac{z}{2}\frac{\partial C}{\partial z}V_{dc}\right] + \frac{1}{2}\frac{\partial^2 C}{\partial z^2}\left[\left(V_{dc} - V_s\right)^2 + \frac{V^2}{2}\right], \tag{3.22}$$

a first harmonic ac component

$$F'_{1\omega} = \left[\frac{q_s}{2\pi\varepsilon_0 z^3}\left(\frac{z}{2}\frac{\partial C}{\partial z} - C\right) + \frac{\partial^2 C}{\partial z^2}\left(V_{dc} - V_s\right)\right] V \sin(\omega t), \tag{3.23}$$

and a second harmonic ac component

$$F'_{2\omega} = -\frac{1}{4}\frac{\partial^2 C}{\partial z^2} V^2 \cos(2\omega t). \tag{3.24}$$

If no charge is present on the surface, the force gradient will oscillate at the 2ω frequency of the second harmonic. The second harmonic can be used to calculate the tip-sample capacitance. If charge is present, the force gradient will be modulated at the frequency ω; therefore, the first harmonic of the force gradient is used to find the charge on the surface. The ω signal is called the "charge signal" and is detected by a second lock-in amplifier at the output of the feedback loop lock-in.[8] The sign of the surface charge is determined by the phase of the ω signal.

EFM can provide a map of ferroelectric domains since the force gradient on the tip depends on the magnitude and sign of the spontaneous polarization. In NC-AFM, the second harmonic of the force gradient and the dielectric constant of the sample are needed to calculate the polarization from the first harmonic signal; unfortunately, the small gap of air between the tip and sample can significantly alter the result of the calculation.[44] Also, the force gradient on the tip can be due to attractive VDW forces in addition to electrostatic Coulomb forces. As a result, it is difficult to obtain precise quantitative data from EFM measurements.

3.3.3 Scanning Kelvin Probe Microscopy

Scanning Kelvin probe microscopy (SKPM), which is also known as Kelvin probe force microscopy (KPFM) and scanning surface potential microscopy (SSPM), was developed to measure the contact potential difference (CPD) between the tip and sample.[12] As with EFM (SKPM is an extension of EFM), the conductive probe is acting in the attractive force regime under long-range Coulomb forces. The lift mode technique, as described above, is used to measure topography and surface potential sequentially. By operating the microscope in lift mode, the amount of cross-talk between topography and surface potential signals is minimized.[45] In SKPM, an additional feedback loop controls the dc offset voltage that is applied to the sample in order to minimize the Coulomb force interaction between the tip and sample. A map of the surface potential is then generated from the dc offset feedback data. SKPM measurements for this dissertation were performed at Oak Ridge National Laboratory (Oak Ridge, TN) using a Digital Instruments NanoMan V AFM.

The total force on the tip is the same as the total force on the tip in EFM, which is given by equation 3.17. As before, the total force on the tip can be divided into three components: a dc component

$$F_{dc} = \frac{q_s}{4\pi\varepsilon_0 z^2}\left(CV_{dc} - q_s\right) + \frac{1}{2}\frac{\partial C}{\partial z}\left[\left(V_{dc} - V_s\right)^2 + \frac{V^2}{2}\right], \tag{3.25}$$

a first harmonic component (ω)

$$F_{1\omega} = \left[\frac{q_s C}{4\pi\varepsilon_0 z^2} + \frac{\partial C}{\partial z}\left(V_{dc} - V_s\right)\right] V\sin(\omega t), \tag{3.26}$$

and a second harmonic component (2ω)

$$F_{2\omega} = -\frac{1}{4}\frac{\partial C}{\partial z}V^2 \cos(2\omega t). \tag{3.27}$$

The second term in the ω component vanishes when the dc bias is equal to the surface potential; hence, the Coulomb interaction is minimized. The value of the measured dc bias then, is equal to

$$V_{dc} = V_s = \phi_t - \phi_s ,$$

where ϕ_t and ϕ_s are the work functions of the tip and sample, respectively. The work function difference is also referred to as the contact potential difference or the Volta potential.[46] If the work function of the metal tip coating is known, the work function of the sample as well as information about the local band structure of the sample can be deduced.

Although SKPM provides a direct surface potential measurement, in the case of ferroelectric surfaces (as well as others) the measurement should be interpreted as an effective surface potential since it includes contributions from polarization bound charge, internal and external screening charges and capacitive interactions.[47,48] The sign of the potential measured by SKPM is often that of the external screening charges (adsorbates) under ambient conditions, which is the opposite of the domain polarization.

3.4 Sources of Error

As with all experimental measurements, there are several sources of possible error in scanning probe microscopy. The most common errors, or image artifacts, are due problems with the tip. Images measured with a SPM are the result of the interaction between tip geometry (radius of curvature and sidewall angles) and surface topography.

This implies the shape of a tip directly influences what a topographic image will look like; hence, it is important to choose an appropriate tip for the application. If the radius of curvature of the tip is much larger than the features on the surface being measured, the lateral resolution is reduced. A protrusion on the surface, such as a nanoparticle, will appear larger and a depression will appear smaller than its true size. Likewise, if a feature has a steeper slope than the sidewall angle of the tip, the image will reflect the sidewall angle of the tip rather than the actual profile of the feature.

As a tip scans across a surface, there is a possibility for loose debris to accumulate on the tip or for the tip to become worn or even chip, especially in contact mode. Any modification of the tip can result in image distortion. One example of such distortion is tip imaging, wherein it is actually the shape of the tip that is being imaged. The most obvious sign of tip imaging is if many of the features in an image appear exhibit structures that resemble each other. Another example is double or multiple tip imaging in which the tip has more than one point in contact with the surface. In this case, as shown in Fig. 3.9 (a), each feature appears two or more times. If tip imaging occurs, the tip should be replaced. Loose debris on the surface can also produce skips and streaking in images (Fig. 3.9 (b)); although, there is a chance the debris can be swept out of the scan area after a few scans and the tip does not have to be replaced.

In addition to the tip, the scanner is also a source of error. Scanner artifacts, which include bow, drift and edge overshoot, are due to piezoelectric properties of the scanner material (PZT). The end of the scanner that contains the tip or sample is free to move while the other end is attached. As a result, the motion of the scanner is nonlinear (in the *z* direction) and the image appears bowed. Bow, which increases with scan size,

can be removed from an image with image processing software. Large changes in *x* and *y* offsets and external temperature changes cause creep in the piezoelectric scanner. Creep produces drift in images that causes features to appear curved or elongated. Hysteresis in the scanner (in the *z* direction) can lead to edge overshoot. Edge overshoot is most often observed in line profiles at the leading and trailing edges of a feature such as a step. Creep and hysteresis can be sufficiently controlled with proper calibration of the scanner.

Forces between the tip and sample are another source of image artifacts, especially when imaging in non-contact mode. For example, if a sample possesses a large electric field, such as lithium niobate, it is possible for the electrostatic interaction between the tip and sample to dominate in a NC-AFM image (rather than attractive VDW forces). This is demonstrated in Fig. 3.9 (c) in which the domain boundaries appear to be raised from the surface. There is no difference in height between domains and domain boundaries when the same area is imaged in contact mode. NC-AFM images may also reflect the surface of the adsorbate layer instead of the actual surface of the material.

Electrical SPM measurements are also prone to error. With use over time, the metal coating wears off of metal coated tips and they are no longer useful for electrical measurements, as they have lost their necessary conductivity. They may, however, still be adequate for obtaining topographic data. Application of an ac bias to a sample also creates errors. If the modulation voltage applied during PFM imaging is too high (greater than the coercive voltage of the material), it is possible to alter the domain structure. When a bias is applied in the absence of a top electrode, electrostatic and capacitive forces are induced between the tip and sample. The electric field is inhomogeneous and

accurate quantitative information about the material cannot be obtained in PFM measurements.

3.5 Summary

Scanning probe microscopy techniques employed for this dissertation were presented in this chapter. The primary modes of AFM imaging used for all scanning force probe measurements were explained, followed by a description of methods employed to detect ferroelectric domains. Tapping mode AFM was used most often to obtain topographic information in this research because it is a high resolution, non-destructive method. PFM was utilized not only to map ferroelectric domains on a sample, but also to create domain patterns of various shapes and sizes. The next few chapters describe how domain patterned ferroelectric material was used for selective deposition and subsequently imaged with AFM in order to observe any structures that may have formed on the surface.

3.5 References

[1] G. Binnig and H. Rohrer, Helv. Phys. Acta **55**, 726 (1982).

[2] G. Binnig, C. F. Quate, and C. Gerber, Phys. Rev. Lett. **56**, 930 (1986).

[3] T. R. Albrecht and C. F. Quate, J. Appl. Phys. **62**, 2599 (1987).

[4] J. W. Hong, D. D. Kahng, J. C. Shin, H. J. Kim, and Z. G. Khim, J. Vac. Sci. Technol. B **16**, 2942 (1998).

[5] Y. Leng and C. C. Williams, Coll. Suf. A **93**, 335 (1994).

[6] J. W. Hong, S. Park, and Z. G. Khim, Rev. Sci. Instrum. **70**, 1735 (1999).

[7] F. Saurenbach and B. D. Terris, Appl. Phys. Lett. **56**, 1703 (1990).

[8] B. D. Terris, J. E. Stern, D. Rugar, and H. J. Mamin, Phys. Rev. Lett. **63**, 2669 (1989).

[9] A. Gruverman, O. Auciello, and H. Tokumoto, J. Vac. Sci. Technol. B **14**, 602 (1996).

[10] A. Gruverman, O. Auciello, and H. Tokumoto, Integr. Ferroelectrics **19**, 49 (1998).

[11] O. Kolosov, A. Gruverman, J. Hatano, K. Takahashi, and H. Tokumoto, Phys. Rev. Lett., **74**, 4309 (1995).

[12] M. Nonnenmacher, M. P. O'Boyle, and H. K. Wickramasinghe, Appl. Phys. Lett. **58**, 2921 (1991).

[13] M. Fujihira and H. Kawate, J. Vac. Sci. Technol. B **12**, 1604 (1994).

[14] M. M. Shvebelman, A. G. Agronin, R. P. Urenski, Y. Rosenwalks, and G. I. Rosenman, Nano Lett. **2**, 455 (2002).

[15] R. Howland and L. Benatar, *A Practical Guide to Scanning Force Microscopy* (Park Scientific Instruments, 1993).

[16] R. Wiesendanger, *Scanning Probe Microscopy and Spectroscopy: Methods and Applications* (Cambridge University Press, Cambridge, 1994).

[17] T. Sakurai and Y. Wantanabe, *Advances in Scanning Probe Microscopy*, (Springer, New York, 2000).

[18] D. Sarid, *Scanning Force Microscopy with Applications to Electric, Magnetic and Atomic Forces*, (Oxford University Press, New York, 1994).

[19] S. Morita, *Roadmap of Scanning Probe Microscopy*, (Springer, New York, 2007).

[20] P. West, *Introduction to Atomic Force Microscopy*, (Pacific Nanotechnology, 2006).

[21] C. Kittel, *Introduction to Solid State Physics*, (Wiley, New York, 1996).

[22] A. Torii, M. Sasaki, K. Hane, and S. Okuma, Sens. Actuators A. **40**, 71 (1994).

[23] T. Stifter, O. Marti, and B. Bhushan, Phys. Rev. B **62**, 13667 (2000).

[24] M. Di Ventra, S. Evoy, and J. R. Heflin, *Introduction to Nanoscale Science and Technology*, (Springer, New York, 2004).

[25] Y. Martin, C. C. Williams, and H. K. Wickramasinghe, J. Appl. Phys. **61**, 4723 (1987).

[26] Q. Zhong, D. Inniss, K. Kjoller, and V. B. Elings, Surf. Sci. Lett. **290**, L688 (1993).

[27] Y. Martin, D. W. Abraham, and H. K. Wickramasinghe, Appl. Phys. Lett. **52**, 1103 (1987).

[28] M. Alexe and A. Gruverman, *Nanoscale Characterisation of Ferroelectric Materials Scanning Probe Microscopy Approach,* (Springer, Berlin, 2004).

[29] P. Guthner and K. Dransfeld, Appl. Phys. Lett. **61**, 1137 (1992).

[30] K. Franke, J. Besold, W. Haessler, and C. Seegebarth, Surf. Sci. Lett. **302**, L283 (1994).

[31] H. Shin, S. Hong, J. Moon, and J. U. Jeon, Ultramicroscopy **91**, 103 (2002).

[32] T. Tybell, P. Paruch, T. Giamarchi, and J. M. Triscone, Phys. Rev. Lett. **89**, 097601 (2002).

[33] K. Terabe, M. Nakamura, S. Takekawa, K. Kitamura, S. Higuchi, Y. Gotoh, and Y. Cho, Appl. Phys. Lett. **82**, 433 (2003).

[34] S. V. Kalinin, D. A. Bonnell, T. Alvarez, X. Lei, Z. Hu, J. H. Ferris, Q. Zhang, and S. Dunn, Nano Lett. **2**, 589 (2002).

[35] M. Alexe, A. Gruverman, C. Harnagea, N. D. Zakharov, A. Pignolet, D. Hesse, and J. F. Scott, Appl. Phys. Lett. **75**, 1158 (1999).

[36] A. Roelofs, U. Boettger, R. Waser, F. Schlaphof, S. Trogisch, and L. M. Eng, App. Phys. Lett. **77**, 3444 (2000).

[37] C. Dehoff, B. J. Rodriguez, A. I. Kingon, R. J. Nemanich, A. Gruverman, and J. S. Cross, Rev. Sci. Instrum. **76**, 023708 (2005).

[38] A. Gruverman, B. J. Rodriguez, C. Dehoff, J. D. Waldrep, A. I. Kingon, R. J. Nemanich, and J. S. Cross, App. Phys. Lett. **87**, 082902 (2005).

[39] L. M. Eng, H. J. Guntherodt, G. A. Schneider, U. Kopke, and J. M. Saldana, Appl. Phys. Lett. **74**, 233 (1999).

[40] B. J. Rodriguez, A. Gruverman, A. I. Kingon, R. J. Nemanich, and J. S. Cross, J. Appl. Phys. **95**, 1958 (2003).

[41] B. J. Rodriguez, A. Gruverman, A. I. Kingon, R. J. Nemanich, and J. S. Cross, App. Phys. A **80**, 99 (2004).

[42] S. Jesse, A. P. Baddorf, and S. V. Kalinin, Nanotechnology **17**, 1615 (2006).

[43] V. Elings and J. Gurley, US Patent Nos. 5,266,801 and 5,308,974, Digital Instruments, Santa Barbara, CA

[44] K. Franke, H. Huelz, and M. Weihnacht, Surf. Sci. **415**, 178 (1998).

[45] H. O. Jacobs, H. F. Knapp, S. Muller and A. Stemmer, Ultramicroscopy **69**, 39 (1997).

[46] P. P. Craig and V. Radeka, Rev. Sci. Instrum. **41**, 258 (1970).

[47] S. V. Kalinin and D. A. Bonnell, Phys. Rev. B **63**, 125411 (2001).

[48] D. A. Bonnell and R. Shao, Current Opin. Solid State Matter Sci. **7**, 161 (2003).

Table 3.1 Specifications of cantilevers utilized in this research.

Material	Shape	Coating	Force Constant (N/m)	Resonant Frequency (kHz)	Tip Radius of Curvature (nm)	Manufacturer
Si	Rectangular	Ti-Pt	5.0	160	<40.0	MikroMasch
Si_3N_4	Triangular	Cr-Au	0.01 0.03 0.1 0.5	7 15 38 120	<60.0	Veeco
Si_3N_4	Triangular	Cr-Au	0.61 0.16	68 22	<40.0	Olympus

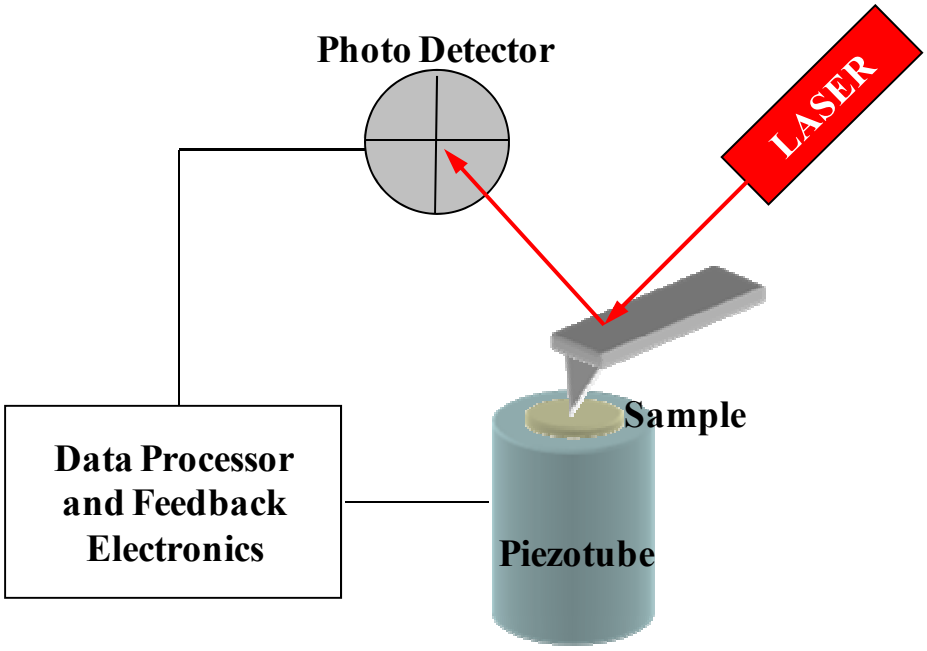


Figure 3.1 Schematic of the AFM setup. A piezoelectric scanner controls the movement of the sample and tip-sample distance. A laser beam is reflected from the back side of the cantilever to a photodetector which records the deflection of the cantilever as it moves across the sample. The data processor and feedback electronics convert the signals and generate an image of the sample surface.

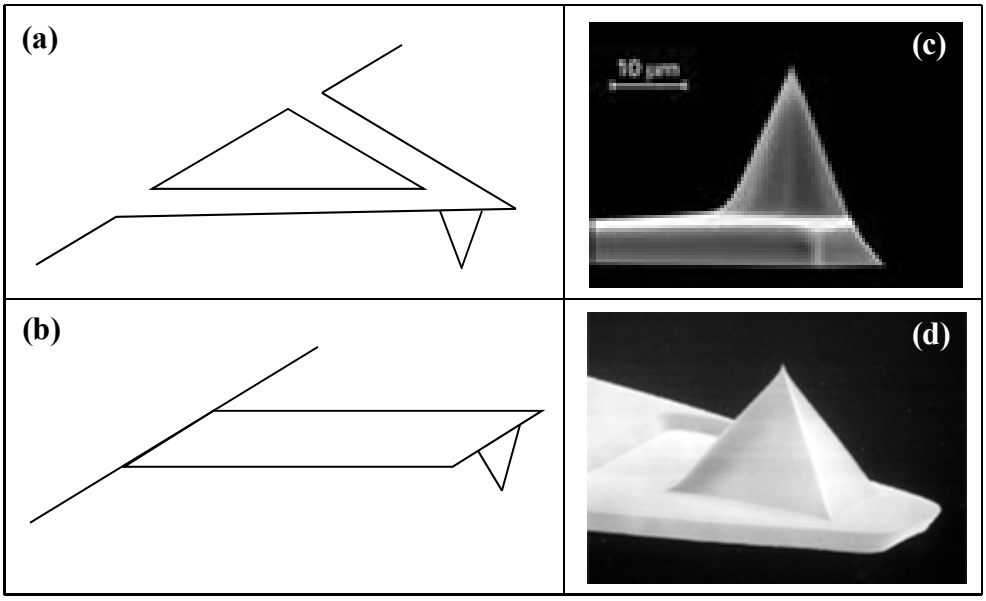


Figure 3.2 The various geometries of cantilevers and probes are displayed. (a) and (b) are line drawings of triangular and rectangular cantilevers, respectively. SEM images reveal the (c) conical and (d) pyramidal shapes of AFM tips. (The image in (c) is courtesy of MikroMasch and (d) of Veeco Probes.)

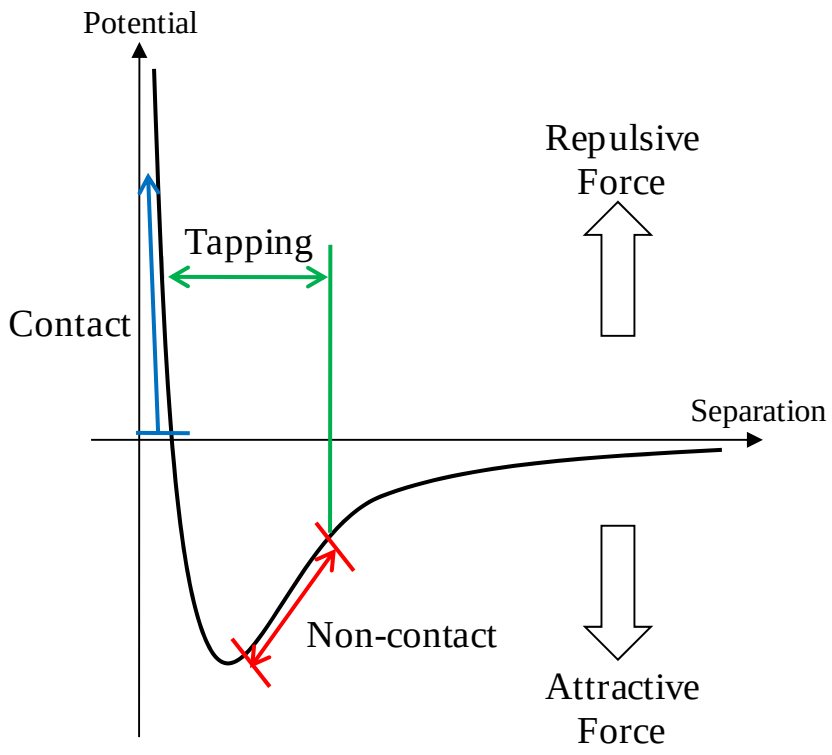


Figure 3.3 Lennard-Jones model of the potential energy of the tip-surface interaction as a function of the distance between them. As the distance between the tip and surface decreases, the tip first experiences attractive, long-range van der Waals forces and then strong, short-range forces due to the Pauli exclusion principle as it comes in "contact" with the surface.

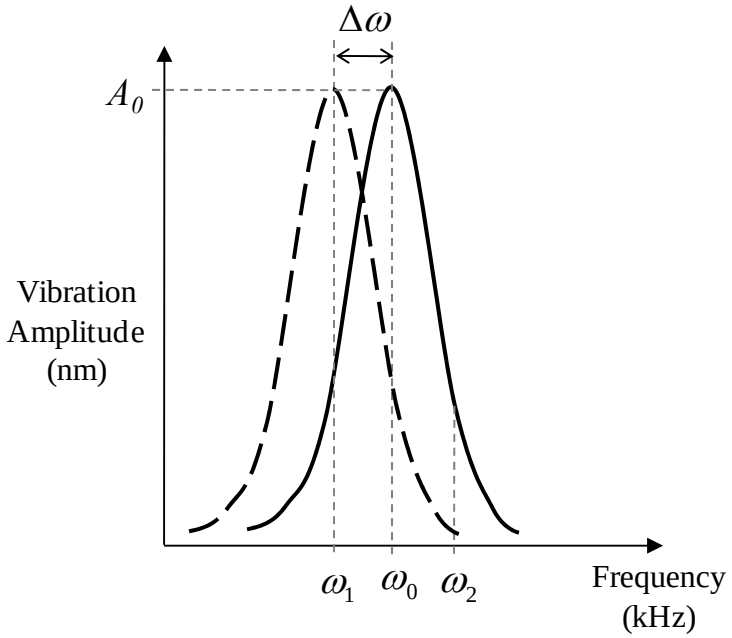


Figure 3.4 Example of an amplitude versus frequency curve for an oscillating force sensor (cantilever). The resonant frequency, ω_0, of the cantilever is located at the peak of the curve where the amplitude is a maximum. In NC-AFM, the cantilever is oscillated at frequency ω_2; whereas in TM-AFM, the cantilever is oscillated at frequency ω_1.

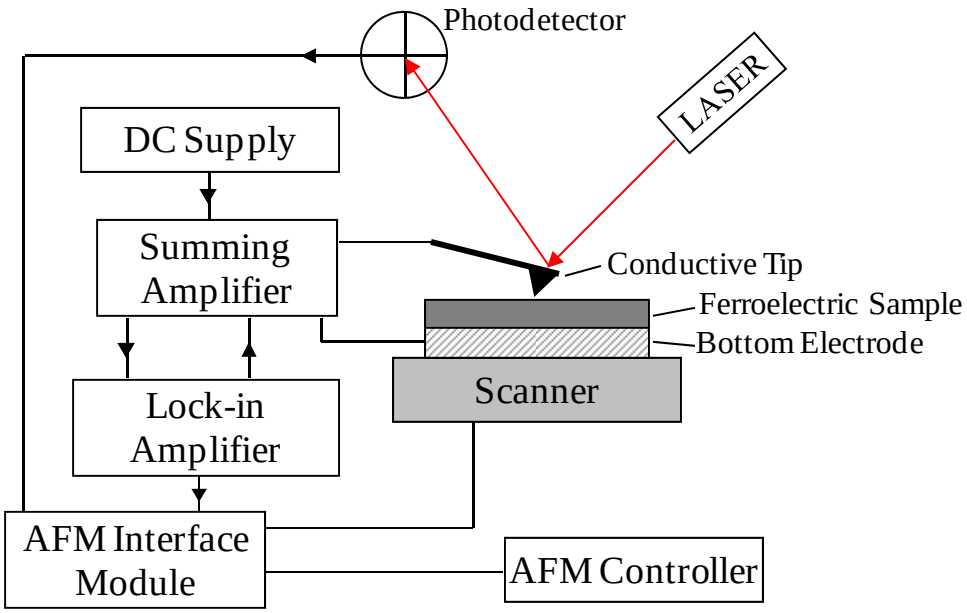


Figure 3.5 Block diagram of the setup used for PFM measurements.

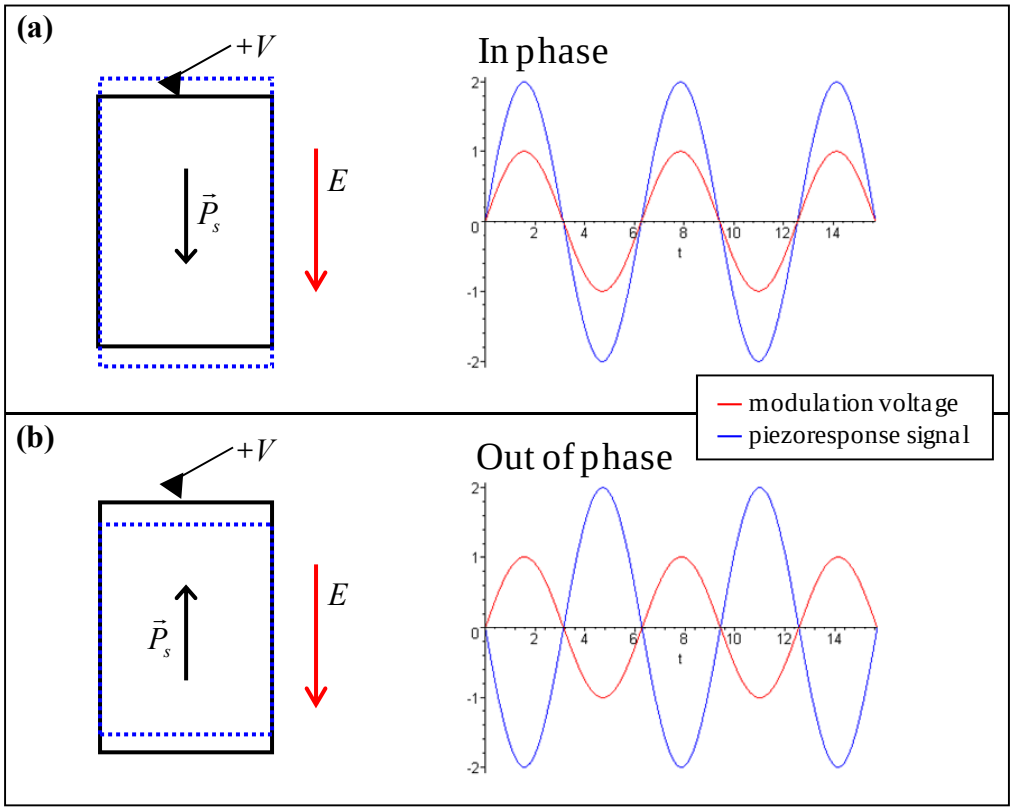


Figure 3.6 In PFM, the orientation of the spontaneous polarization in ferroelectric material can be determined from the phase difference of the piezoresponse signal. (a) The dashed blue line indicates an increase in height of the sample surface under an applied electric field (sample expands). The domain oscillating in phase with the applied voltage ($\theta = 0°$) and the polarization vector is pointing toward the bottom electrode (-*c* domain). (b) The dashed blue line indicates a decrease in height of the sample surface (sample contracts). The domain is oscillating out of phase with the applied voltage ($\theta = 180°$) and the polarization vector is pointing toward the tip (+*c* domain).

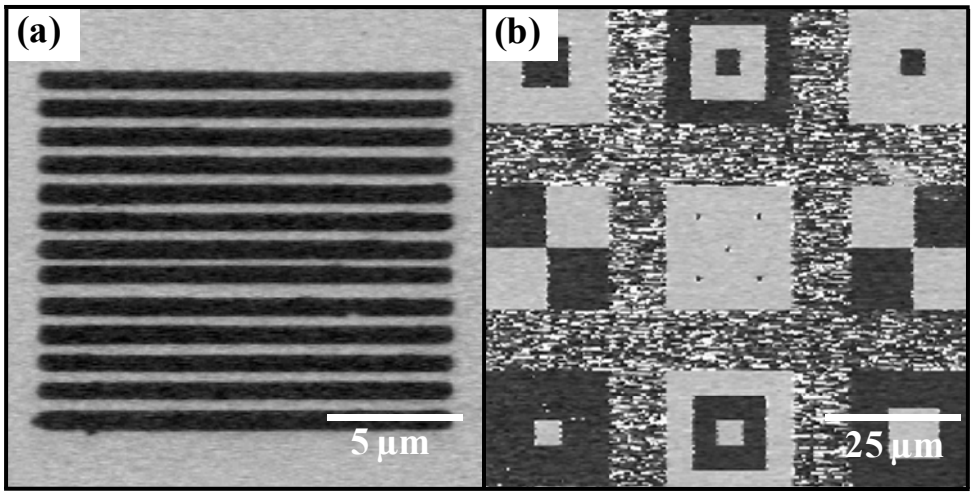


Figure 3.7 PFM phase images of ferroelectric domain patterns written with an AFM tip. The dark regions are positive domains and the bright regions are negative domains. The horizontal lines in (a) were written in a single domain lithium niobate sample by applying a negative bias to the $-z$ surface. The pattern in (b) was written by applying positive and negative biases to a thin film PZT surface. Randomly oriented domains appear as noise in between the written domains.

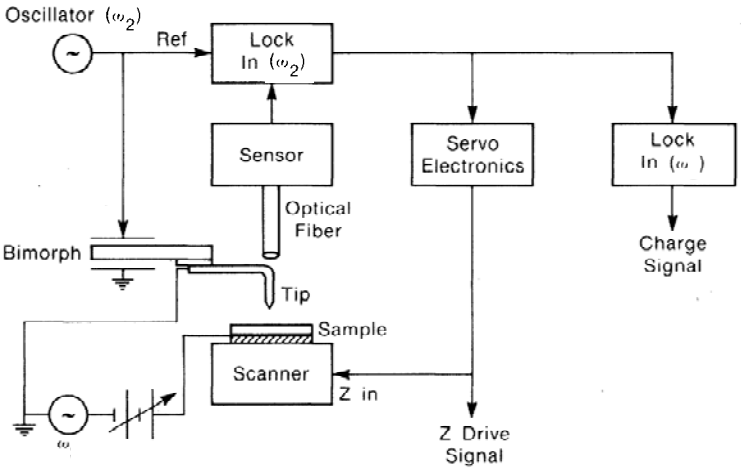


Figure 3.8 Block diagram of the original setup used for EFM measurements (Terris *et al*., 1989). The bimorph (piezoelectric actuator) oscillates the cantilever at frequency ω_2. The first harmonic of the force gradient generates the charge signal which is used to create a map of the surface charge of the sample. The sensor used for experiments in this dissertation was a position sensitive photodiode, not an optical fiber.

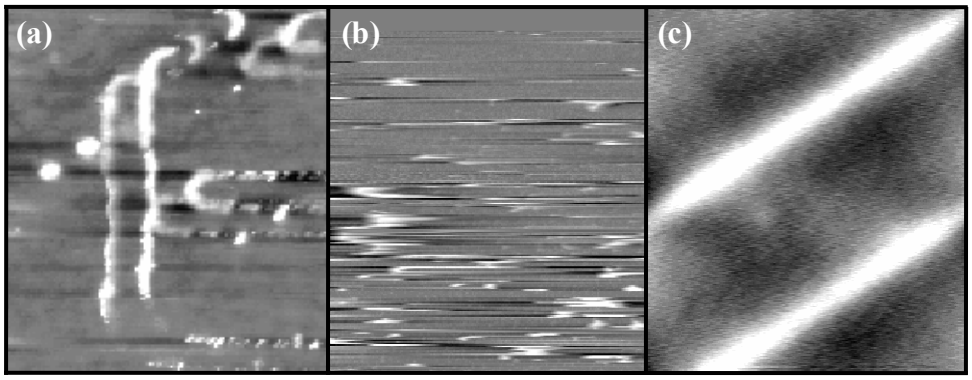


Figure 3.9 Examples of SPM image artifacts. The double image seen in (a) is due to double tip imaging, in which the tip has two points in contact with the surface. The streaking in (b) is a result of loose debris on the surface being dragged by the tip. (c) shows a contrast in height between the domains and domain boundaries in ferroelectric lithium niobate. The contrast is not an actual topographic feature; it is the presence of strong electric fields dominating the NC-AFM force regime.

4. Fabrication of Metallic Nanowires on a Ferroelectric Template via Photochemical Reaction

This chapter is based on the following publication:

Jacqueline N. Hanson, B. J. Rodriguez, R. J. Nemanich, and A. Gruverman,
Nanotechnology **17**, 4946 (2006).

Department of Physics and Department of Materials Science and Engineering,
North Carolina State University,
Raleigh, NC 27695-8202

4.1 Abstract

Fabrication of silver nanowires on a domain-patterned lithium niobate template by inducing a photoreduction from aqueous solution is reported. Silver deposition occurs preferentially along the domain boundaries which separate antiparallel domains. The nanowires can reach the length of hundreds of micrometers and their location can be controlled by generating domain patterns of a desired configuration while their width depends on deposition conditions, such as temperature, solution concentration and UV light exposure time. The selective deposition process is explained by a combination of the inhomogeneous distribution of the electric field in the vicinity of the domain wall and the low conductivity of the template material. Controllable and selective deposition of metal species onto nanoscale domain-patterned ferroelectric templates may provide an alternative bottom-up route to lithographic fabrication methods.

4.2 Introduction

Miniaturization of electronic devices requires development of structural elements of reduced dimensions. Metallic nanowires are attracting great interest due to their application as interconnecting components of nanoscale devices as well as chemical sensors and biological labels.[1,2] Numerous techniques have been adopted for the growth of metal nanowires. Many of the top-down lithography-based methods provide high-precision positioning and size control but are limited in downscaling the nanowire diameter below 50 nm.[3,4] The bottom-up approaches allow fabrication of the nanowires with much smaller diameters but are time consuming, suffer from poor registration and require special templates that in turn involve top-down processing.[5]

A unique feature of ferroelectric materials is a spontaneous polarization, the direction of which can be changed by the application of an external electric field.[6] Polar surfaces of ferroelectrics are characterized by the presence of surface charges that can be utilized in a new set of applications, including local molecular self-assembly, local physical adsorption/desorption, local chemical reactions, local charge transfer reactions, and the manipulation of individual molecules. There are a number of reports on domain-specific deposition of materials on ferroelectric surfaces governed either by Coulomb interaction or electrochemical reactions.[7,8,9] Prior experiments utilizing the effect of ferroelectric polarization on chemical reactivity have demonstrated the viability of this approach for fabrication of complex nanostructures.[10,11]

In this chapter, we present a liquid phase processing method for the fabrication of

silver nanowires on a domain-patterned ferroelectric template via a photochemical reaction. We demonstrate that the local reactivity on the ferroelectric surfaces depends not only on polarization but also on the intricate balance between polarization charges, adsorbed charges and defect states near the surface. It is shown that variations in the local surface electronic properties induced by the domain walls leads to preferential deposition of silver along the domain boundaries. As the domain walls in ferroelectrics can be as thin as several unit cells, this approach opens a possibility of fabricating metallic wires of nanoscale dimensions.

4.3 Experimental Details

In this work, periodically poled lithium niobate (PPLN) substrates of congruent composition (Crystal Technologies) were used as ferroelectric templates. At room temperature lithium niobate exhibits a hexagonal symmetry with polarization along the *c*-axis, which allows only two possible domain orientations. The samples used in this study were 3 x 3 x 0.5 mm^3 plane-parallel plates cut normal to the polar axis. The periodic domain structure (period of ~28 μm) was fabricated using a lithographic mask and liquid electrodes; the electrodes were removed after poling. In addition, *c*-cut 0.9 μm thick crystals of stoichiometric lithium niobate (SLN) were used in this study. The lower switching threshold field of the SLN samples[12] allows local domain switching using a conductive tip of an atomic force microscope (AFM). Domain patterns of arbitrary configuration were written in the SLN samples using a computer-controlled Keithley 236 Source Measure Unit by applying a negative bias of 30 V to the sample via a Pt-coated tip (MikroMasch, k = 5 N/m). The same tip was used for visualization of the domain

patterns in both samples by means of piezoresponse force microscopy (PFM).[13]

Sample preparation for silver deposition was as follows: the sample was sonicated for 20 minutes first in acetone and then for 20 minutes in methanol. After cleaning, the sample was placed in a petri dish, and the surface was covered with an aqueous $AgNO_3$ solution of 0.01 M concentration. The sample was then illuminated with a 20 W Hg pen lamp placed above the sample. Two different Hg pen lamps were used in the experiments, one with the predominant emission at 254 nm, which corresponds to strong optical absorption, and another with the predominant emission at 365 nm which has a photon energy less than the ~3.9 eV band gap of lithium niobate. According to the manufacturer's specifications, the power density at a distance of 2 cm from the lamp is ~1 to 4 mW/cm^2. The irradiation time was varied in the range from 1 minute to 30 minutes. Immediately following illumination, the sample was immersed in deionized water for 1 minute and then blown dry with nitrogen. After the deposition, samples were imaged in non-contact mode AFM (NC-AFM) in order to preserve any structures that had formed on the surface.

4.4 Results

Figure 4.1 (a) displays an AFM topographic image of the surface of the PPLN sample, which shows no apparent surface features associated with the domain structure. The PFM images of the same area (Figs. 4.1 (b) and (c)) reveal a pattern of periodically poled 180º domains of ~14 μm wide. Analysis of the contrast variation in the PFM phase image allows identification of domain polarity: dark contrast indicates $+c$ domains (with positive surface polarization charges), while bright contrast corresponds to $-c$ domains.

In the PFM amplitude image, the boundaries between antiparallel domains appear as dark lines of about 150 nm wide. (We note parenthetically that this result, which confirms the previously reported data on domain wall width in lithium niobate, presents an unsolved problem: while the first-principle calculations suggest that the width of the 180º domain wall should be just 1-2 unit cells,[14] the experimental observations by means of X-ray synchrotron imaging[15] and PFM[16,17,18] show significant broadening of the walls. It is speculated that this phenomenon might be a result of a strong residual stress in the vicinity of the wall associated with Li vacancies.)

In previously reported studies, deposition occurred on the negative or positive surfaces of the domains depending on the sign of the charge carried by the particles or the type of the chemical reaction (reduction or oxidation). In our case, however, the deposition pattern turns out to be quite different. Illustrated in Fig. 4.1 (d) is a typical structure consisting of Ag lines observed after the aqueous photoreduction procedure using the 254 nm UV light on the PPLN sample. Comparison of the topographic image of the silver lines with the corresponding PFM images shows that silver deposition occurred preferentially along the domain boundaries with silver lines following the perimeter of the negative domains. The line width can be controlled in the range from 70 nm to 300 nm by changing the UV exposure time from 1 to 30 minutes. Furthermore, it has been found that the deposition process is sensitive to the light wavelength: silver deposition was not observed on the sample surface illuminated with the below band gap 365 nm light.

Topographic imaging at a higher magnification reveals that the lines are formed by clusters of 30-150 nm silver particles (inset in Fig. 4.1 (d)). Formation of continuous

Ag lines with high aspect ratio (nanowires) can be achieved by performing the photoreduction process at elevated temperature (T ~ 80ºC). Figure 4.2 shows several examples of nanowire formation using various domain patterns generated in the SLN sample by the conductive AFM tip. It is evident that the aqueous photoreduction process using domain-patterned templates allows fabrication of nanowire arrays with control over their position, shape and aspect ratio.

4.5 Discussion

4.5.1 Deposition at the Domain Boundary

In prior deposition experiments employing particles in solution,[9] it has been assumed that the interaction between the deposited ions or charged particles and the ferroelectric surface is electrostatic in nature and results from the fact that the ferroelectric holds a surface charge density arising from its spontaneous polarization. However, in an aqueous solution, the formation of an electric double layer due to the adsorption of water dipoles or different ionic species should lead to essentially complete screening of the polarization charges. Because of this fact, surface decoration techniques described several decades ago usually work only when insulating organic liquids are used.[7] In this case, charged colloidal particles are attracted to the surfaces of the polar domains.

The fact that in our experiments silver is deposited along the domain boundaries can be, in principle, attributed to the dipolar interaction of charged particles with the field gradient existing in the vicinity of the domain wall. Decoration of domain walls has been observed in colloidal solutions containing particles with high dielectric constants.[7] In this

case, the non-uniform electric field interacting with the field-induced polarization in the particles would provide a force tending to move them towards the domain boundaries (a process related to the dielectrophoretic effect). However, the fact that without UV irradiation silver deposition was not observed indicates that the dielectrophoretic effect cannot explain the domain wall decoration with silver. In addition, the size of the ions in the solution is far smaller than the minimum particle size (of the order of several hundred nanometers) required for an appreciable dielectrophoresis effect.

In the present experiment, the expectation was that the reduction of silver ions by the excess electron charge generated by UV light would lead to selective silver deposition on $+c$ domains similar to the previously reported results of photochemical reactions on surfaces of barium titanate $BaTiO_3$ (BTO) crystals and $Pb(Zr,Ti)O_3$ (PZT) films.[10,11] To explain this significantly different pattern of selective deposition in lithium niobate, we consider the difference in electronic properties of lithium niobate and the perovskite ferroelectrics used in the previous studies and additionally take into account the distribution of the electric field in the vicinity of the domain wall.

In PZT films, oxygen loss during high-temperature annealing of the film typically produces a high concentration of oxygen vacancies. This high concentration of defect states near the surface in PZT, estimated as 10^{14} cm^{-2} (see Ref. 19), leads to a significant contribution of internal screening that compensates the polarization charges and leads to strong band bending at the surface as shown in Fig. 4.3 (a, b). The absorption of the above band gap light results in the generation of electron-hole pairs across the PZT film. In PZT with a relatively high mobility of the electrons (0.2 cm^2 V^{-1} s^{-1}), the electron-hole pairs generated by the UV light subsequently become separated by the electric field of the

space-charge layer with electrons moving to the surface towards the end of the positive domain and holes drifting away from it. The electron charges can then participate in the photochemical reduction of ionic Ag^+ to metal Ag^0 via the reaction,

$$Ag^+ + e^- \rightarrow Ag^0 . \tag{4.1}$$

Given that the defect density near the film surface is two orders of magnitude higher than in the bulk of the PZT film (10^{-20} versus 10^{-18} cm^{-3}, respectively),[19] it can be assumed that the regions close to the surface provide most of the electrons for the photochemical reaction on the surface.

In the lithium niobate crystal, a low concentration of defect states near the surface (10^{12} cm^{-2})[20] implies that the predominant external mechanism of polarization screening is via surface absorption of charged molecules (Fig. 4.3 (c, d)). The band bending will thus occur over a length scale that is large compared to the UV absorption length.[21] Because of the weak electric field near the surface, the separation of electron-hole pairs is less efficient and there will be dynamic equilibrium of the generation and recombination processes. However, calculation of the electric field near the surface of the lithium niobate following the approach used in Ref. 22 and assuming complete external polarization screening shows that the field distribution is nonuniform (Fig. 4.4). The equation for the electric field at the surface E_z (z delineates the direction along the polar axis, or the normal component of the field) has the following form:

$$E_z = \frac{-8h\varepsilon_0\sigma}{L\varepsilon_2\left(\varepsilon_0 + \sqrt{\varepsilon_x\varepsilon_z}\right)}\sqrt{\frac{\varepsilon_x}{\varepsilon_z}}\sum_{n=0}\sin\left(\frac{2\pi(2n+1)x}{L}\right)\exp\left(\frac{2\pi(2n+1)z}{L}\sqrt{\frac{\varepsilon_x}{\varepsilon_z}}\right), \tag{4.2}$$

where h is the thickness of the adsorbate layer, σ is the surface charge density, L is the

domain width, and ε_x, ε_z and ε_2 are the components of the LN dielectric constant and the dielectric constant of the adsorbate layer, respectively. The following values were used in this calculation: h =0.25 nm, $\sigma = \vec{P}_s \cdot \hat{n} = 70$ μC cm^{-2}, L=14 μm, ε_x=84, ε_z=30 and ε_2=80 (it is assumed the adsorbate layer consists mainly of water).[20]

Indeed, a strong electric field, E_z, resulting from the superposition of the fields of polarization and screening charges exists in the vicinity of the 180º domain wall while away from it the field is almost zero (Fig. 4.4). Thus, it may be expected that, as a result of the inhomogeneous field distribution, separation of the photoinduced electron-hole pairs will occur only in the vicinity of 180º domain walls with excess electron charge accumulating on the surface along the domain wall. Since lithium niobate has a band gap energy of ~ 3.9 eV,[21] only light with a wavelength less than 318 nm can be used for optical generation of electron charge, which explains the absence of any selective silver deposition on the sample illuminated with the 365 nm UV light. It should be noted that irradiation for a longer period of time or with high power UV light leads to silver deposition on the positive surfaces of the domains which can be explained by gradual accumulation of the photoinduced charges on polar surfaces.

In principle, there is an additional mechanism that can result in strong local electric fields, which is related to the defect structure of lithium niobate. It has been shown that domain walls are stabilized by slow reorientation of defect dipoles comprised of niobium antisites (Nb_{Li}) and lithium vacancies (Vac_{Li}). This process can lead to the formation of local electric fields of the order of several kV/cm[23] and stronger band bending. In addition, an in-plane component of the electric field E_y due to defects[24] can

allow the migration of the carriers across the domain wall which will serve as a sink for the accumulating positive charge. The effect of defect concentration on heating and the selective deposition process is discussed in the following section.

4.5.2 The Roles of Stoichiometry and Temperature

Silver formed in clusters along domain boundaries on the stoichiometric lithium niobate sample when photoreduction was performed at room temperature (Fig. 4.5 (a)), similar to Ag formation on the congruent PPLN sample (Fig. 4.5 (c)). When the deposition was performed at an elevated temperature of ~80°C, continuous lines of Ag (nanowires) formed on the domain boundaries as shown in Figs. 4.2 and 4.5 (b). There was no significant difference in the formation of Ag on the congruent PPLN sample during photoreduction at an elevated temperature (Fig. 4.5 (d)), however. The difference in Ag formation at elevated temperature between the congruent and stoichiometric samples is attributable to the variation of properties due to the defect structures of the crystals.

Lithium niobate of congruent composition (CLN) is deficient in lithium (C=Li/[Li+Nb]~0.485),[25] resulting in a much greater concentration of intrinsic defects in CLN crystals than in stoichiometric crystals (C~0.5). As mentioned above, these defects consist of niobium antisites (Nb_{Li}) and lithium vacancies (Vac_{Li}) according to the lithium-site vacancy model.[26] Defects due to lithium nonstoichiometry can strongly affect electrical, optical and thermal properties of lithium niobate crystals thus influencing the results of photochemical reactions and selective deposition at the surface.

In a pyroelectric crystal such as lithium niobate, a change in temperature causes a

change in the spontaneous polarization,[27] which in turn, results in an excess of free charges at the surface of the material. For example, the magnitude of the spontaneous polarization will decrease with an increase in temperature creating an excess of negative charge at the $+c$ surface. In the case of lithium niobate, in which the polarization screening mechanism is predominantly external, the excess adsorbed negative charge can leave the surface. There is less external screening at the surface of congruent lithium niobate compared to stoichiometric lithium niobate due to the higher number of intrinsic defects present in congruent crystals. This is reflected in the results of deposition at elevated temperature; nanowire formation is enhanced on the SLN crystal, while there is little change in the formation on the CLN crystal.

Additionally, the kinetic energy of ions in solution increases with an increase in temperature.[28] This implies there is a greater number of collisions between the ions and the solution, thus there is increased opportunity for photoreduction of the silver ions in silver nitrate.

4.6 Conclusion

In summary, we have developed a liquid phase processing method for the fabrication of silver nanowires on a domain-patterned ferroelectric template via a photochemical reaction. Variations in the local surface electronic properties induced by the domain walls lead to preferential deposition of silver along the domain boundaries. The observed behavior is explained by the local reactivity on the ferroelectric surfaces, which depends not only on polarization but also on the intricate balance between polarization charges, adsorbed charges and surface states. As the domain walls in

ferroelectrics can be as thin as several unit cells, this approach opens a possibility of fabricating metal nanowires of nanoscale diameter.

Furthermore, this approach allows fabrication of nanowires of any aspect ratio by developing domain patterns of desired configuration and by adjusting the temperature, solution concentration and irradiation time. This is important for many applications, which are dependent on the nanowire aspect ratio. Using this approach, nanowires could be assembled into complex two-dimensional structures, and nanowire segments of different metals could potentially be fabricated by using solutions containing different metal ions.

4.7 Acknowledgements

This work was supported by the National Science Foundation NIRT Grant No. 0403871, NSF Grant DMR-0235632, US–Israel Bilateral Science Foundation (BSF) and a GAANN fellowship. The authors acknowledge useful discussions with V. Gopalan. Invaluable discussions with S. V. Kalinin and his help in calculations of the electric field distribution are greatly appreciated. The authors thank Dr. K. Kitamura for supplying the stoichiometric lithium niobate sample used in this study.

4.8 References

[1] J. I. Pascual, J. Mendez, J. Gomezherrero, A. M. Baro, N. Garcia, U. Landman, W. D. Luedtke, E. N. Bogachek, and H. P. Cheng, Science **267**, 1793 (1995).

[2] T.M Whitney, J. S. Jiang, P. C. Searson, and C. L. Chien, Science **261**, 1316 (1993).

[3] L. L. Sohn and R. L. Willett, Appl. Phys. Lett. **67**, 1552 (1995).

[4] M. Geissler, H. Wolf, R. Stutz, E. Delamarche, U. W. Grummt, B. Michel, and A. Beitsch, Langmuir **19**, 6301 (2003).

[5] W. D. Williams and N. Giordano, Rev. Sci. Instrum. **55**, 410 (1984).

[6] M. E. Lines and A. M. Glass, *Principles and Applications of Ferroelectrics and Related Materials* (Clarendon, Oxford, 1977).

[7] G. L. Person, W. L. Feldmann, J. Phys. Chem. Solids **9**, 28 (1958).

[8] G. I. Distler, V. P. Konstantinova, V. M. Gerasimov, G. A. Tolmacheva, Nature **218**, 762 (1968).

[9] G. I. Distler, J. Cryst. Growth **3**, 175 (1968).

[10] J. L. Giocondi and G. S. Rohrer, Chem. Mater. **13**, 241 (2001).

[11] S. V. Kalinin, D. A. Bonnell, T. Alvarez, X. Lei, Z. Hu, and J. H. Ferris, Nano Lett. **2**, 589 (2002).

[12] V. Gopalan, T. E. Mitchell, Y. Furukawa, and K. Kitamura, Appl. Phys. Lett. **72**, 1981 (1998).

[13] A. Gruverman, O. Auciello and H. Tokumoto, Ann. Rev. of Mat. Sci. **28,** 101 (1998).

[14] J. Padilla, W. Zhong, and D. Vanderbilt, Phys. Rev. B **53**, R5969 (1996).

[15] S. Kim, V. Gopalan, and B. Steiner, Appl. Phys. Lett. **77**, 2051 (2000).

[16] B. J. Rodriguez, R. J. Nemanich, A. I. Kingon, A. Gruverman, S. V. Kalinin, K. Terabe, X. Y. Liu, and K. Kitamura, Appl. Phys Lett. **86**, 012906 (2005).

[17] C. E. Valdivia, C. L. Sones, J. G. Scott, S. Mailis, and R. W. Eason, D. A. Scrymgeour V. Gopalan, T. Jungk, E. Soergel, I. Clark, Appl. Phys. Lett. **86**, 022906 (2005).

[18] S. Kim, V. Gopalan, and A. Gruverman, Appl. Phys. Lett. **80**, 2740 (2002).

[19] J. F. Scott, *Ferroelectric Memories* (Springer, 2000).

[20] A. M. Prokhorov and Yu. S. Kuz'minov, *Physics and Chemistry of Crystalline Lithium Niobate* (Taylor and Francis, 1990).

[21] W. C. Yang, B. J. Rodriguez, A. Gruverman, and R. J. Nemanich, Appl. Phys. Lett. **85**, 2316 (2004).

[22] S. V. Kalinin and D. A. Bonnell, Phys. Rev. B **63**, 125411 (2001).

[23] S. Kim, V Gopalan, K. Kitamura, Y. Furukawa, J. Appl. Phys. **90**, 2949 (2001).

[24] T. J. Yang, V. Gopalan, P. J. Swart, and U. Mohideen, Phys. Rev. Lett. **82**, 4106 (1999).

[25] S. Kim, V. Gopalan, K. Kitamura, and Y. Furukawa, J. Appl. Phys. **90**, 2949 (2001).

[26] N. Iyi, K. Kitamura, F. Izumi, J. K. Yamamoto, T. Hayashi, H. Asano, and S. Kimura, J. Solid State Chem. **101**, 340 (1992).

[27] J. F. Nye, *Physical Properties of Crystals Their Representation by Tensors and Matrices* (Oxford, London, 1957).

[28] T. L. Brown, H. E. LeMay, and B. E. Bursten, *Chemistry The Central Science* (Prentice Hall, New Jersey, 2000).

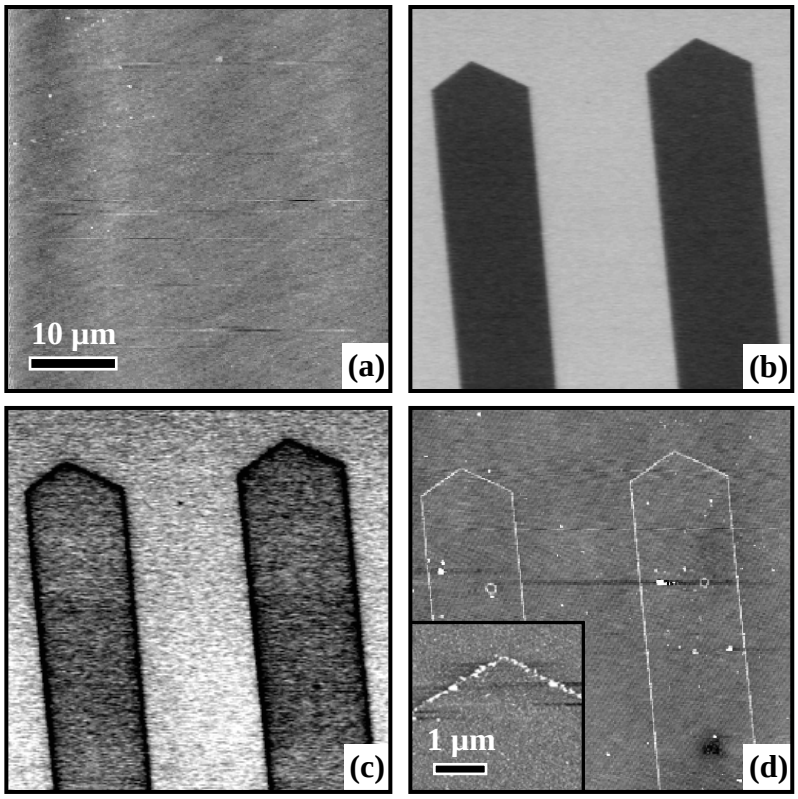


Figure 4.1 (a) Topographic image of the PPLN sample before deposition; (b, c) Corresponding PFM phase and amplitude images, respectively, of the PPLN sample; (d) topographic image of the same sample after deposition (inset: higher resolution topographic image illustrating the structure of the lines as formed by silver particles).

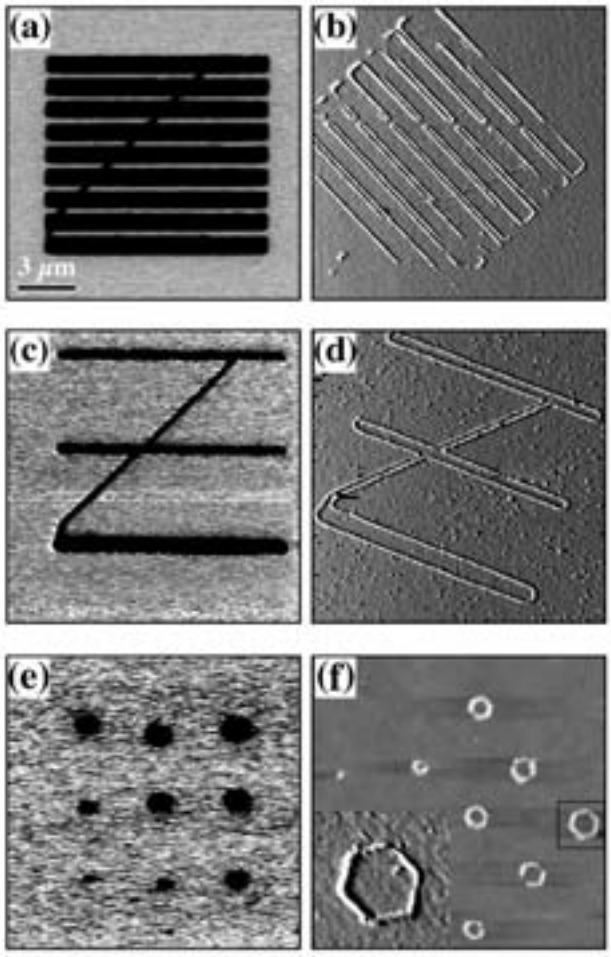


Figure 4.2 (a, c, e) PFM images of domain patterns generated in the SLN sample by a conductive AFM tip. (b, d, f) Corresponding topographic images of silver nanowires fabricated by aqueous photoreduction at 80ºC. Topographic images are rotated by 30º to 45º clockwise with respect to the PFM images. The scan size in (a-f) is 15x15 μm^2. The inset in (f) shows a zoomed image of the area marked by the black block. The scan size of the inset is 2x2 μm^2.

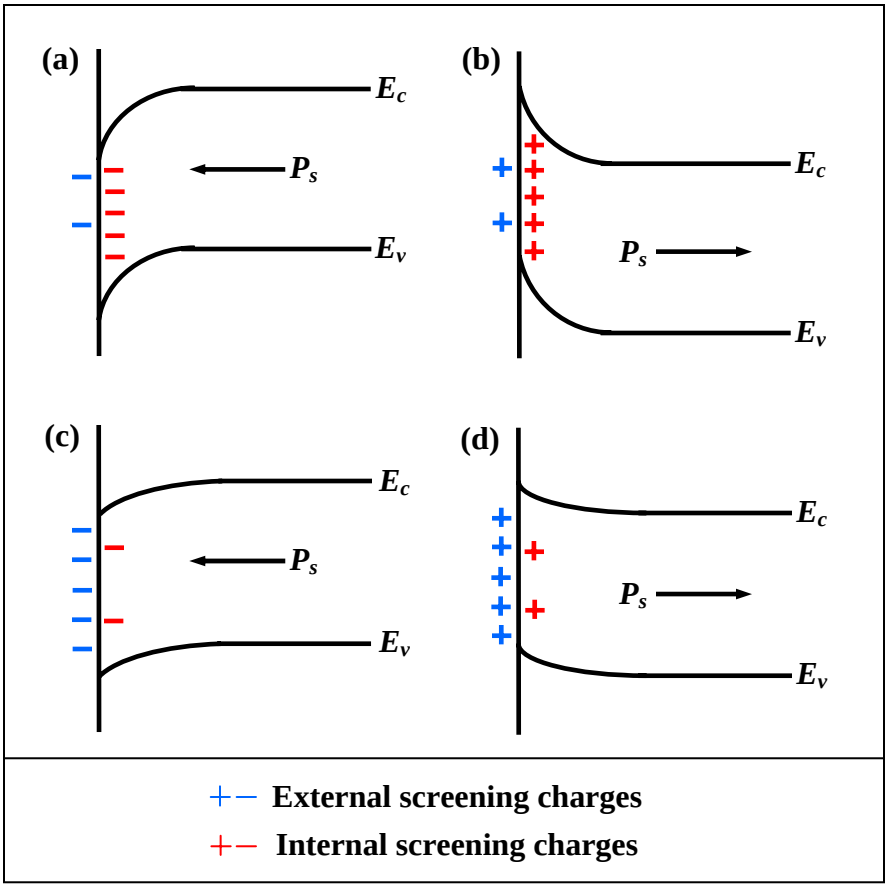


Figure 4.3 Band diagrams for positive (a) and negative (b) domains in PZT demonstrating strong band bending due to a high concentration of defect states (internal screening) near the surface. LN, which has a smaller concentration of defect states, is predominantly screened externally; thus, the band bending that occurs at the surface of positive (c) and negative (d) domains is smaller than that of PZT.

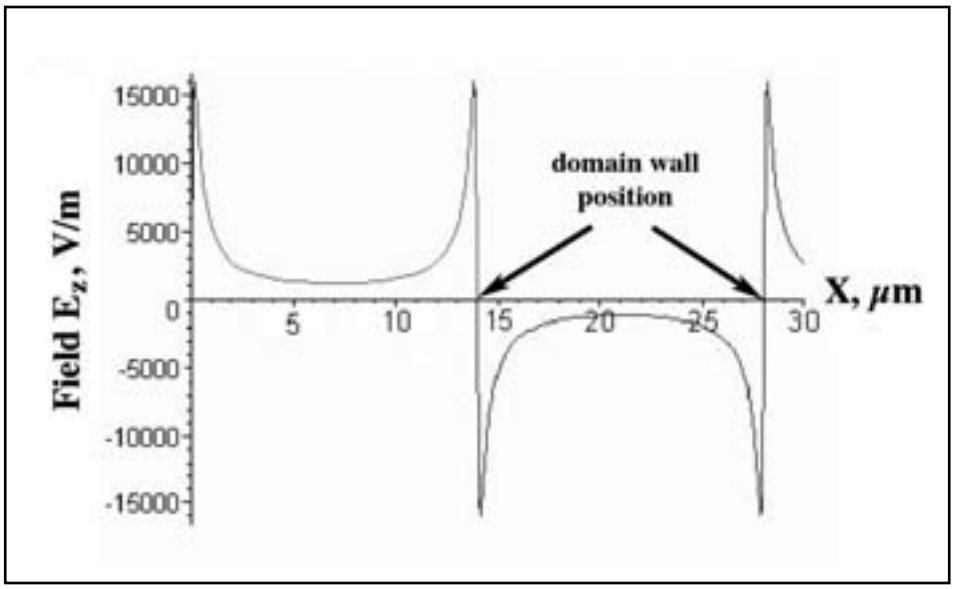


Figure 4.4 Calculated distribution of the normal component of the electric field for the periodically poled lithium niobate at a distance of 100 nm below the surface.

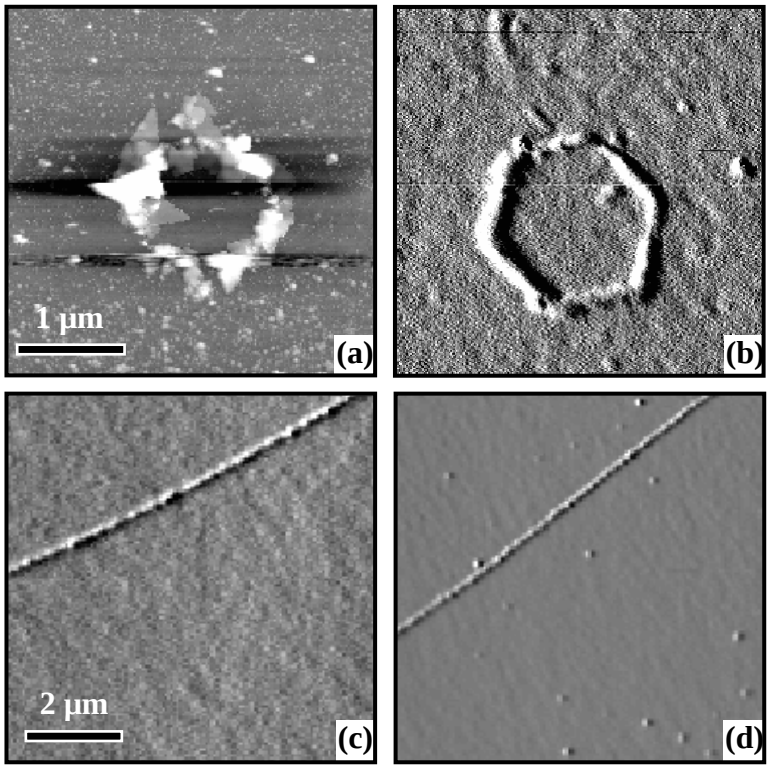


Figure 4.5 AFM topographic images of silver formation on SLN (a, b) and CLN (c, d) after aqueous photoreduction at 25ºC (a, c) and 80ºC (b, d). At elevated temperature,

5. Selective Photoreduction of Metallic Salt Solutions on Domain Patterned $LiTaO_3$ and Mg:$LiTaO_3$

Jacqueline N. Hanson,[1] A. Gruverman,[1] and R. J. Nemanich[2]

[1]Department of Physics and Department of Materials Science and Engineering
North Carolina State University
Raleigh, NC 27695-8202

[2]Department of Physics
Arizona State University
Tempe, AZ 85287-1504

5.1 Abstract

Domain specific deposition of metals on domain patterned ferroelectric templates of undoped near stoichiometric lithium tantalate (SLT) and MgO (1.0 mol%) doped SLT (Mg:SLT) is presented. The formation of metal on the ferroelectric surfaces is attributed to the reduction of aqueous metal salt solutions by photogenerated electrons from the material. We demonstrate the mechanism of silver and gold formation on the surfaces is dependent upon the composition of the template material and the corresponding electronic properties of the surface as well as the concentration of the solution. In addition, we show the deposition procedure may also be utilized for the formation of metallic nanoplates.

5.2 Introduction

Lithium niobate and lithium tantalate have attracted a great deal of attention due to their excellent electro-optic, non-linear optic, and piezoelectric properties that make them ideal for use in applications such as quasi-phase matching and piezoelectric devices.[1,2] The composition of these crystals greatly affects many of their properties, and some properties can be enhanced by increasing the stoichiometry of the composition and/or doping. The magnitude of the coercive field required to reverse the polarization, for example, is 210 kV cm^{-1} in congruent lithium tantalate and 17 kV cm^{-1} in stoichiometric lithium tantalate (a difference of over an order of magnitude).[3] The lower switching field allows for nanoscale domain patterning via scanning probe microscopy (SPM),[4] which is useful for our experiments. In Chapter 4 we demonstrated selective deposition of silver via photoreduction on congruent and stoichiometric domain patterned lithium niobate.

Recently, selective deposition on ferroelectric materials has shown ferroelectric materials may be used as a template for the assembly of functional complex nanostructures via a bottom up approach. In this chapter, we explore photochemical reactions on the surface of stoichiometric and MgO doped stoichiometric lithium tantalate. As lithium niobate and lithium tantalate are structurally very similar, we expected photochemical reactions to proceed in a similar manner on their surfaces. Furthermore, it is expected that doping should alter the pattern of deposition on the surface depending on the type of dopant. In this study, we demonstrate that the mechanism of photogenerated electron transfer to the surface of these oxygen octahedra ferroelectrics is highly dependent upon the electronic properties of the material, which

vary with stoichiometry and doping, as well as the photon energy of the incident light. We also show the pH and concentration of the metallic salt solution used for the photodeposition process impacts the location and shape of metal formation on the surface. Depending on the experimental conditions, nanowires and nanoplates may be formed via photochemical reactions at the surface of lithium tantalate.

5.3 Experimental Details

Periodically poled ferroelectric substrates of stoichiometric lithium tantalate (PPSLT) and 1 mol% MgO doped near-stoichiometric lithium tantalate (Mg:PPSLT) were used for this study. At room temperature, lithium tantalate exhibits hexagonal symmetry with its polar axis aligned parallel to the *c*-axis; hence, only two domain orientations are possible (antiparallel 180º domains). Both doped and undoped crystals were grown using the double crucible Czochralski technique.[5,6] Plane-parallel plates of 0.5 mm thickness were cut from boules normal to the z-axis (growth axis). The periodic domain structure, which has a period of ~8 to 10 μm, was fabricated by depositing a metal electrode on a patterned photoresist film on the +*c* surface of the crystals and applying an electric field of less than 2 kV/mm.[6] Piezoresponse force microscopy (PFM) with a Pt-coated tip (MikroMasch, $k = 5$ N/m) was used to visualize the domain pattern in both samples.[7]

Prior to all deposition experiments, the crystals were sonicated in acetone and then methanol in order to remove any debris from the surface. Immediately following cleaning, the sample was covered with one of two aqueous metal salt solutions; both silver nitrate ($AgNO_3$) of 0.01 M concentration and gold (lll) chloride ($HAuCl_4$) of

varying concentration were used for the experiments. A 20 W Hg pen lamp was placed 2 cm above the sample at room temperature and the sample was illuminated for times ranging from 1 to 30 minutes. Two Hg pen lamps were used; one with predominant emission at 254 nm, corresponding to strong optical absorption, and another with predominant emission at 365 nm, which has a photon energy less than the ~ 4.77 eV band gap[8] of stoichiometric lithium tantalate. According to the manufacturer's specifications, the power density at a distance of 2 cm from the lamp is ~1-4 mW/cm^2. For deposition at elevated temperature, the sample and solution were heated to 80°C before and for the duration of irradiation with UV light. After illumination, the sample was removed from solution, rinsed in deionized water, and then blown dry with nitrogen. Samples were imaged in tapping mode AFM (TM-AFM) following the deposition procedure in order to preserve any structures that had formed on the surface.

5.4 Silver Nitrate

5.4.1 Results

5.4.1.1 PPSLT

An AFM topographic image of the surface of the undoped PPSLT sample, which shows no apparent surface features associated with the domain structure, is displayed in Fig. 5.1 (a). The PFM phase image of the same area (Fig. 5.1 (b)) reveals a pattern of periodically poled antiparallel domains that have a periodicity of ~10 μm. Analysis of the contrast variation in the PFM phase image allows identification of domain polarity: dark contrast indicates $+c$ domains (with positive surface polarization charges), while bright contrast corresponds to $-c$ domains.

Topographic images of the PPSLT surface after aqueous photoreduction using the 254 nm pen lamp are displayed in Fig. 5.1 (c) and (b). Similar to previously reported studies in which deposition occurred on the positive or negative surfaces of the domains depending on the sign of the charge carried by the particles and the type of the chemical reaction (reduction or oxidation),[9,10] silver formed on the positive domains of the PPSLT surface. Deposition at elevated temperature resulted in an increase in the amount of silver that formed on the domains. In addition, the formation of silver was not observed on the surface when the sample was illuminated with the 365 nm (below band gap) lamp.

5.4.1.2 MgO doped PPSLT

The surface of a MgO doped PPSLT sample is displayed in the topographic image in Fig. 5.2 (a). As with the undoped sample, no surface features associated with the domain structure are evident. The periodic domain pattern of periodicity of ~8 μm is illustrated in the PFM phase image of Fig. 5.2 (b), in which dark contrast corresponds to +*c* domains and bright contrast to –*c* domains.

Figure 5.2 (c) shows a typical AFM topographic image of the Mg:PPSLT surface after photoreduction of aqueous silver nitrate was performed with the 254 nm pen lamp. In contrast to the deposition result of the undoped PPSLT sample, a greater amount of silver formed at the domain boundaries than the on the positive domains. The nanowire-like formation of silver at the domain boundaries is more clearly demonstrated in the higher magnification image of Fig. 5.2 (d). This result is comparable to results previously reported by our group (Chapter 4), in which silver nanowires form at the domain boundary on lithium niobate surfaces via aqueous photoreduction.[11] The

sequence of images in Fig. 5.4 (a-d) shows the Mg:PPSLT surface after 2, 4, 8, and 10 minute illumination times. This figure indicates formation of silver occurs on domain boundaries first, followed by positive domains.

Photoreduction of aqueous silver nitrate at elevated temperature on the Mg:PPSLT sample causes the photochemical reaction to occur at an accelerated rate, as compared with the undoped PPSLT sample. Also analogous to the undoped sample, photodeposition of silver is not observed on the surface of the Mg:PPSLT sample after irradiation with the 365 nm lamp.

5.4.2 Discussion

Previous reports of photochemical reactions on the surfaces of perovskite ferroelectrics have demonstrated domain specific deposition. For example, metallic silver formed on the positive (+*c*) domains of PZT films via the reaction[10]

$$Ag^{+} + e^{-} \rightarrow Ag^{0}, \tag{5.1}$$

in which a silver ion (Ag^{+}) combines with a photogenerated electron (e^{-}). In PZT, the bound polarization charge is screened predominantly internally due a high concentration (~10^{14} cm^{-2})[12] of defect states near the surface. Internal screening leads to strong band bending at the surface, thus photoexcited charge carriers are easily separated by the electric field in the space charge layer and electrons can move to the surface of +*c* domains where they can participate in photochemical reactions.

Lithium tantalate, on the other hand, has a smaller concentration of intrinsic defects and polarization screening is predominantly external through the adsorption of

charged molecules. Furthermore, stoichiometric crystals of lithium tantalate have an even lower concentration of intrinsic defects than congruent crystals.[13] Due to this small amount of internal screening, the length scale over which band bending will occur is large compared to that of UV absorption (as with lithium niobate)[14] resulting in a weak electric field at the surface and, subsequently, less efficient separation of photoexcited electron-hole pairs. This implies electrons must reach the surface of lithium tantalate via a different mechanism than in PZT.

In our previously reported study of the aqueous photoreduction of silver nitrate on the surface of domain patterned lithium niobate (Chapter 4), we attributed the formation of silver at the 180º domain boundaries to a combination of the surface electronic properties of the crystal and an inhomogeneous distribution of the electric field at the boundaries. Lithium niobate and lithium tantalate are structurally very similar and consequently exhibit similar characteristics;[15] thus, it was expected that photochemical reactions at the surfaces of these materials would proceed in a corresponding manner. The difference in results, however, indicates the pattern of selective deposition in these oxygen octahedra ferroelectrics is highly dependent upon variations in electronic properties of the crystals.

The band gap of lithium tantalate is ~4.77 eV, therefore only light with a wavelength less than ~260 nm can excite charge carriers within the crystal, as less energetic photons are not absorbed. This explains the absence of metal formation on the surface when the 365 nm pen lamp was used. Additionally, photons possessing a much larger energy than the band gap of the crystal are primarily absorbed at the surface, contributing little to the conductivity of the bulk. The energy difference between the

band gap of lithium niobate (~3.9 eV)[14] and the photon energy of the 254 nm pen lamp is much greater than that of lithium tantalate (1.0 eV for LN vs. 0.13 eV for LT); hence, there may be greater photon absorption at the surface of lithium niobate than in the bulk compared to lithium tantalate at this wavelength. In this case, it is possible the bulk photovoltaic effect may be the dominant charge driving force in lithium tantalate.[16,17]

Photovoltaic current in ferroelectrics, such as lithium tantalate, is due to the asymmetry of the charge transfer process resulting from the asymmetry of the crystal lattice (displacement of Li^{+} and Ta^{5+} along the polar axis) and Frank-Condon relaxation;[18,19] thus, the current develops along the *c*-axis of lithium tantalate under illumination of light of certain photon energies. Because electrons tend to move in the +*c* direction (toward the surface of positive domains), reduction of silver occurs primarily at the surface of positive domains. Additionally, the dark conductivity of lithium tantalate at room temperature is $\sigma_{dark} = 1.5 \times 10^{-15}$ Ω^{-1} cm^{-1},[8] while under illumination with 257 nm light of 10 mW cm^{-2} intensity (similar to the specifications of our pen lamp), the photoconductivity of lithium tantalate is $\sigma_{ph} = 3 \times 10^{-10}$ Ω^{-1} cm^{-1}.[20] With an increase in the conductivity of five orders of magnitude and transport via the bulk photovoltaic effect, it is possible electrons are effectively moved to the surface where they can participate in photochemical reactions.

The photoreduction of silver on the surface of MgO doped stoichiometric lithium tantalate surface yielded a different result (Fig. 5.2 (c and d)). As with photoreduction of silver on lithium niobate, nanowire-like structures are formed on domain boundaries by clusters of 30-90 nm silver particles. Formation of silver was also observed on the

positive domains. $Mg^{2+}O^{2-}$ is a p-type dopant in lithium tantalate, thus there should be an excess of holes (*e*+) (Fig. 5.3). It is expected that some of the photogenerated electrons will combine with these excess holes before they reach the surface, thus reducing the amount of silver formed on the positive domains. This is reflected in the decreased photoconductivity of Mg:SLT ($\sigma_{ph} = 10^{-10}$ Ω^{-1} cm^{-1}),[20] which is three times less than that of SLT. Additionally, the field distribution of PPSLT (and Mg:PPSLT) is similar to the distribution calculated for lithium niobate in Chapter 4 following the approach of Kalinin and Bonnell.[21] Thus, it is possible that photogenerated electron-hole pairs are also separated in the vicinity of 180º domain boundaries resulting from the inhomogeneous field distribution with excess electron charge accumulating on the surface along the domain boundaries. The results imply this process is slightly stronger in Mg:PPSLT than the photovoltaic effect.

The sequence of images in Fig. 5.4 (a-d) demonstrates the accumulation of silver on the surface over a time period of 10 minutes. It is clear from Fig. 5.4 (a) that the formation of silver begins at the domain boundaries. This is consistent with our model for the formation of silver on lithium niobate surfaces.[11] Over time, silver also accumulates on the positive domains. The accumulation of silver on positive domains occurs much faster on lithium tantalate than on lithium niobate (~10 minute difference). Again, this indicates that the bulk photovoltaic effect may be the dominant charge driving force in lithium tantalate allowing electrons to move to the surface of positive domains; whereas, it is not the dominant charge driving force in lithium niobate due to the

difference between the photon energy of the incident light and the band gap of the material.

When the deposition was performed at an elevated temperature of ~80ºC, silver covered the entire surface (a difference in height remained between domains of opposite polarity and the domain boundaries, indicating some surfaces were covered with a greater amount of silver), which implies the reaction occurred at an accelerated rate. It is well known that the rate of most chemical reactions increases with increasing temperature.[22] As the temperature of the aqueous silver nitrate solution increases, the average kinetic energy of the molecules in the solution also increases; therefore, the number of collisions between the silver ions in the solution and the surface of the lithium tantalate crystal increases. Furthermore, in a pyroelectric crystal such as lithium tantalate, a change in temperature causes a change in the spontaneous polarization, which in turn, results in an excess of free charges at the surface of the material. The magnitude of the spontaneous polarization decreases with increasing temperature until it reaches zero at the Curie temperature; upon cooling, the spontaneous polarization increases.[15] Thus, the accelerated rate of deposition can be attributed to a combination of the increase in number of collisions of silver ions with the surface and the excess free charges at the surface of lithium tantalate resulting from the decrease of the spontaneous polarization.

5.5 Gold Chloride

5.5.1 Results

The optical microscope image (in unpolarized transmitted light) in Fig. 5.4 (a) shows the surface of a clean PPSLT sample. There are no apparent features related to the

domain structure in the image. When the surface was exposed to UV illumination (using the 254 nm pen lamp) in a 0.1 mM aqueous gold chloride solution, gold formed everywhere. Both positive and negative domains were covered with gold, however, there was an average height difference of ~20 nm between domains. This indicates a greater amount of gold formed on the positive domains, as no height difference between domains of opposite polarity is observed in topographic images of the clean PPSLT surface. Domain contrast after deposition is obvious in the optical microscope image (Fig. 5.4 (b)) and the AFM topographic image (Fig. 5.4 (c)).

An unanticipated result was obtained with use of $HAuCl_4$ of 0.01 M concentration (the same concentration as the $AgNO_3$ solution) in the experiments. Domain selective deposition was not observed; rather, islands of ~10 nm height formed randomly on the surface. The islands, which are hexagonal and triangular in shape, are visible in the optical microscope image in Fig. 5.4 (d) due to their large size. The shapes of the islands are consistent with the underlying *3m* (trigonal) crystal symmetry of the lithium tantalate.[23,24] Topographic images of higher magnification of the islands are displayed in Fig. 5.4 (e) and (f). The edges of the hexagonal island have an average length of ~1.66 μm, while the edges of the triangular island have equal lengths of ~1.52 μm. In addition, a truncated triangular island formed on the MgO doped PPSLT surface (Fig. 5.6). The height of the island displayed in Fig. 5.6 varies from ~3-8 nm and the long edges of the triangle are ~2 μm in length, while edge length of the truncated corners is ~800 nm.

As with the aqueous silver nitrate solution, gold formation did not occur on the PPSLT surface when the 365 nm pen lamp was used with the aqueous gold chloride

solution suggesting photodeposition on lithium tantalate surfaces is sensitive to light wavelength.

5.5.2 Discussion

There are a number of studies that report the formation of hexagonal, triangular and truncated triangular metallic gold nanoplates of (111) lattice planes via the reduction of gold chloride.[25,26,27,28] The thickness of the nanoplates are in the range of tens of nanometers, while the widths of the nanoplates vary over a large range from hundreds of nanometers to tens of microns. The islands that formed on lithium tantalate in the present study are consistent with these dimensions. In all of these previous studies, a reducing agent or polyelectrolyte was added to the aqueous $HAuCl_4$ solution in order to induce the reaction and gold nanoplates formed as precipitates of the reaction. In our experiments, however, the solution only contained a mixture of $HAuCl_4$ and deionized water. Chen *et al*. utilized UV irradiation in addition to polyacrylic acid to induce the reactions to form these gold nanoplates, citing that the reaction was dependent upon photoexcited electrons from the Teflon dish in which the reaction was performed.[29] It is possible, therefore, the islands that formed on our lithium niobate samples are gold nanoplates.

Furthermore, previous studies have demonstrated $HAuCl_4$ concentration[25] and solution pH[30] play key roles in the formation of gold precipitates. Spherical nanoparticles form instead of nanoplates if the solution concentration is too low, which our results are in agreement with. We have demonstrated the formation of gold nanoparticles on lithium tantalate surfaces with the use of 0.1 mM concentration gold chloride (Fig. 5.5 (c)). The pH of our gold salt solutions was measured to be 1.5 and 3 for 0.01 M and 0.1 mM

concentrations, respectively. Kumaran *et al*. found the rate of gold formation significantly decreased when the pH of the solution was above 3.0, while below a pH of 2.5 the formation of gold increased.[30] Although this is in contrast to our results, the reducing agent (Na_2SO_3) they used in the solution contributes to the increase of the gold formation. In our case, the increase of H^+ (lower pH) at a higher concentration of $HAuCl_4$ may result in screening of the photogenerated electrons at the surface thus decreasing the amount of gold formation.

Kalinin *et al*. also observed the formation of gold triangles and hexagons on perovskite ferroelectrics, which they attributed to dependence on surface energies.[10] It is not clear, however, if the gold formation they observed was domain specific. The formation of gold islands on lithium tantalate is not predetermined by domain configuration. Investigation of the mechanism of gold formation on ferroelectric surfaces is continuing in our group.

5.6 Conclusion

In summary, we have demonstrated domain patterned lithium tantalate can be utilized as a template for the formation of nanostructures. It is clear that there are many competing factors that determine the specific outcome of the photodeposition process on ferroelectric surfaces. In particular, the pattern of silver deposition on the surface is highly dependent upon the charge distribution at the surface as well as the composition and ensuing electronic properties of the template material. We have shown selective deposition of silver can occur on the surface of domain boundaries in lithium tantalate, as with lithium niobate, and/or on the surface of positive domains.

We have also demonstrated the concentration and pH of the solution used in the photodeposition process can affect the location and shape of the metal formation on the surface. With acidic gold chloride solution, nanoplate-like structures form on the surface of lithium tantalate. Although the exact mechanism of formation of these gold nanoplates is still unknown, under proper conditions it may be possible to utilize the electronic properties of ferroelectrics to control their formation.

5.7 Acknowledgements

This work was supported by the National Science Foundation NIRT Grant No. 0403871 and a GAANN fellowship. The authors thank Dr. K. Terabe for supplying the lithium tantalate samples used in this study.

5.7 References

[1] L. E. Myers, G. D. Miller, R. C. Eckardt, M. M. Feyer, and R. L. Byer, Opt. Lett. **20**, 52 (1995).

[2] K. Mizuuchi and K. Yamamoto, Appl. Phys. Lett. **66**, 2943 (1995).

[3] S. Ganesamoorthy, M. Nakamura, S. Takekawa, S. Kumaragurubaran, K. Terabe, and K. Kitamura, Mater. Sci. Eng. B **120**, 125 (2005).

[4] K. Terabe, M. Nakamura, S. Takekawa, K. Kitamura, S. Higuchi, Y. Gotoh, and Y. Cho, Appl. Phys. Lett. **82**, 433 (2003).

[5] S. Kumaragurubaran, S. Takekawa, M. Nakamura, and K. Kitamura, J. Crystal Growth 285 (2005) 88.

[6] S. Kumaragurubaran, S. Takekawa, M. Nakamura, and K. Kitamura, J. Crystal Growth 292 (2006) 332.

[7] A. Gruverman, O. Auciello, and H. Tokumoto, Annu. Rev. Mater. Sci. 28 (1998) 101.

[8] P. Dittrich, B. Koziarska-Glinka, G. Montemezzani, P. Günter, S. Takekawa, K. Kitamura, and Y. Furukawa, J. Opt. Soc. Am. B **21**, 632 (2004).

[9] J. L. Giocondi and G. S. Rohrer, Chem. Mater. **13**, 241 (2001).

[10] S. V. Kalinin, D. A. Bonnell, T. Alvarez, X. Lei, Z. Hu, and J. H. Ferris, Nano Lett. **2**, 589 (2002).

[11] J. N. Hanson, B. J. Rodriguez, R. J. Nemanich, and A. Gruverman, Nanotechnology **17**, 4946 (2006).

[12] J. F. Scott, *Ferroelectric Memories* (Springer, Berlin, 2000).

[13] Y. Furukawa, K. Kitamura, K. Niwa, H. Hatano, P. Bernasconi, G. Montemezzani, and P. Günter, Jpn. J. Appl. Phys. **38**, 1816 (1999).

[14] W.-C. Yang, B. J. Rodriguez, A. Gruverman, and R. J. Nemanich, Appl. Phys. Lett. **85**, 2316 (2004).

[15] M. E. Lines and A. M. Glass, *Principles and Applications of Ferroelectrics and Related Materials* (Oxford, New York, 1977).

[16] X. Liu, K. Kitamura, K. Terabe, H. Hatano, and N. Ohashi, Appl. Phys. Lett. **91**, 044101 (2007).

[17] F. Holtman, J. Imbrock, Ch. Bäumer, H. Hesse, E. Krätzig, and D. Kip, J. Appl. Phys. **96**, 7455 (2004).

[18] V. M. Fridkin, *Photoferroelectrics* (Springer-Verlag, New York 1979).

[19] A. M. Glass, D. von der Linde, and T. J. Negran, Appl. Phys. Lett. **25**, 233 (1974).

[20] F. Juvalta, B. Koziarska-Glinka, M. Jazbinšek, G. Montemezzani, K. Kitamura, and P. Günter, Opt. Expr. **14**, 8278 (2006).

[21] S. V. Kalinin and D. A. Bonnell, Phys. Rev. B **63**, 125411 (2001).

[22] T. L. Brown, H. E. LeMay, and B. E. Bursten, *Chemistry: The Central Science* (Prentice Hall, New Jersey, 2000).

[23] X. Zhang, D. Xue, and K. Kitamura, Mater. Sci. Eng. B **120**, 21 (2005).

[24] X. Zhang, D. Zue, X. Liu, K. Terabe, and K. Kitamura, J. Phys. D: Appl. Phys. **39**, 3103 (2006).

[25] D. Ibano, Y. Yokota, and T. Tominaga, Chem. Lett. **32**, 574 (2003).

[26] H.-C. Chu, C.-H. Kuo, and M. H. Huang, Inorg. Chem. **45**, 808 (2006).

[27] X. Sun, S. Dong, and E. Wang, Langmuir **21**, 4710 (2005).

[28] Y. Shao, Y. Jin, and S. Dong, Chem. Commun., 1104 (2004).

[29] H. Chen, J. Jia, and S. Dong, Nanotechnology **18**, 245601 (2007).

[30] A. U. S. Kumaran, T. Miyawaki, and M. Ichimura, Jpn. J. Appl. Phys. **45**, L1283 (2006).

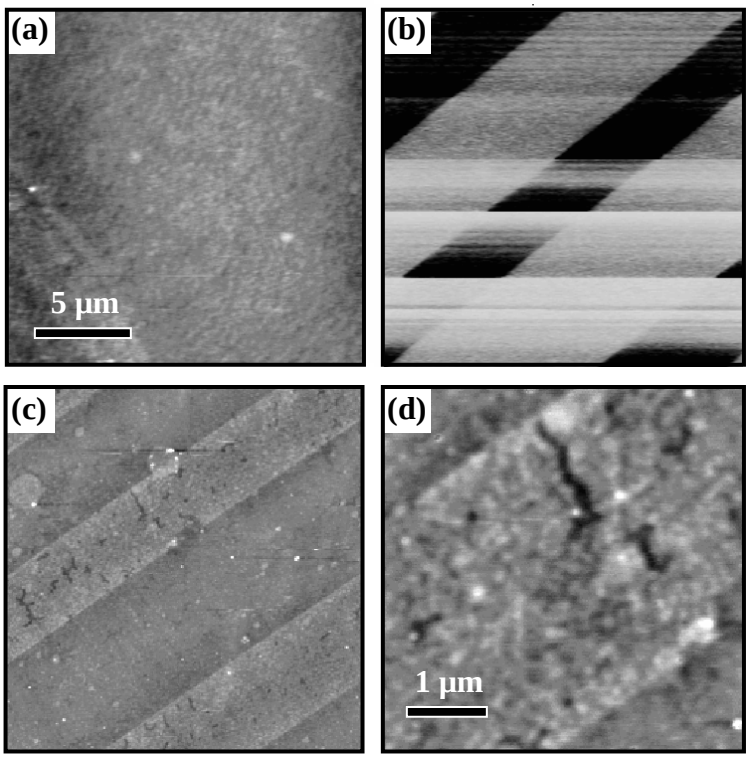


Figure 5.1 AFM topographic image (a) and corresponding PFM phase image (b) of the PPSLT surface prior to deposition. After photoreduction of aqueous silver nitrate, silver formation on the positive domains is visible in topographic images (c, d).

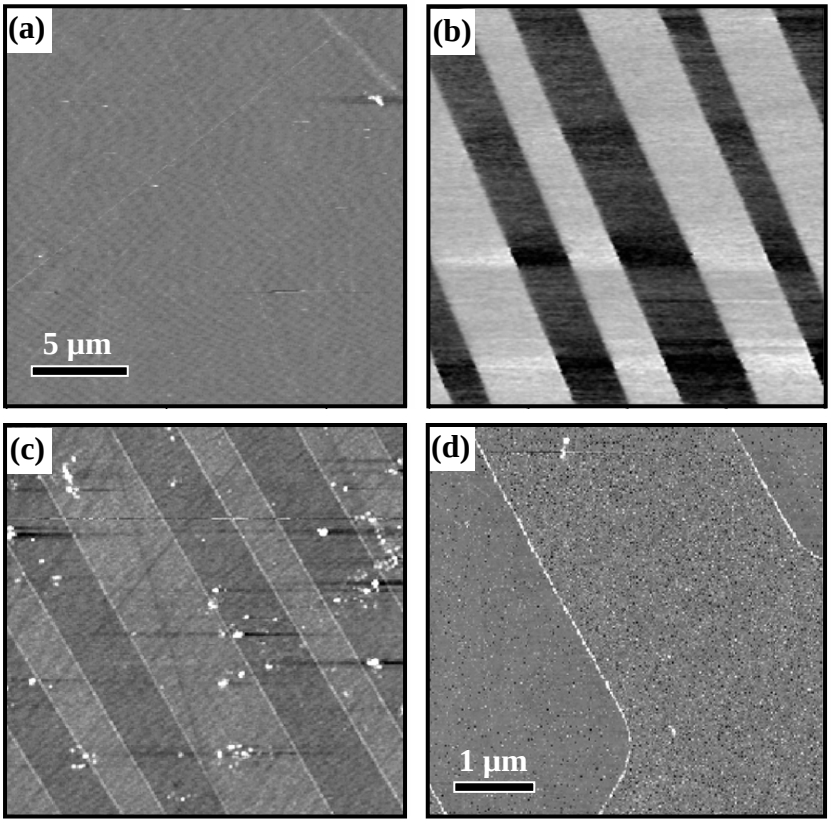


Figure 5.2 AFM topographic image (a) and corresponding PFM phase image (b) of the Mg doped PPSLT surface prior to deposition. After photoreduction of aqueous silver nitrate, silver formation on the positive domains is visible in topographic images (c). In the higher magnification image (d), silver formation at the domain boundaries is also apparent.

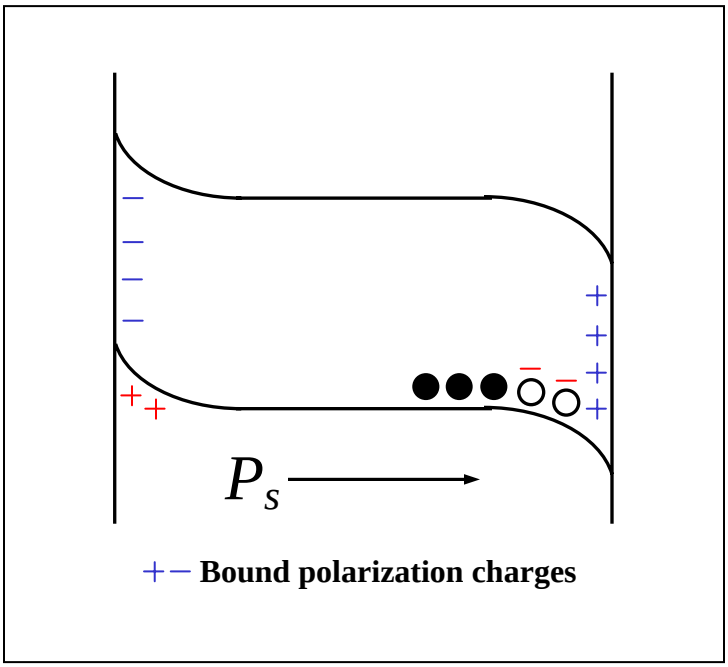


Figure 5.3 Band bending diagram for Mg doped PPSLT. MgO is a p-type dopant, thus there an excess of holes exists in the valence band.

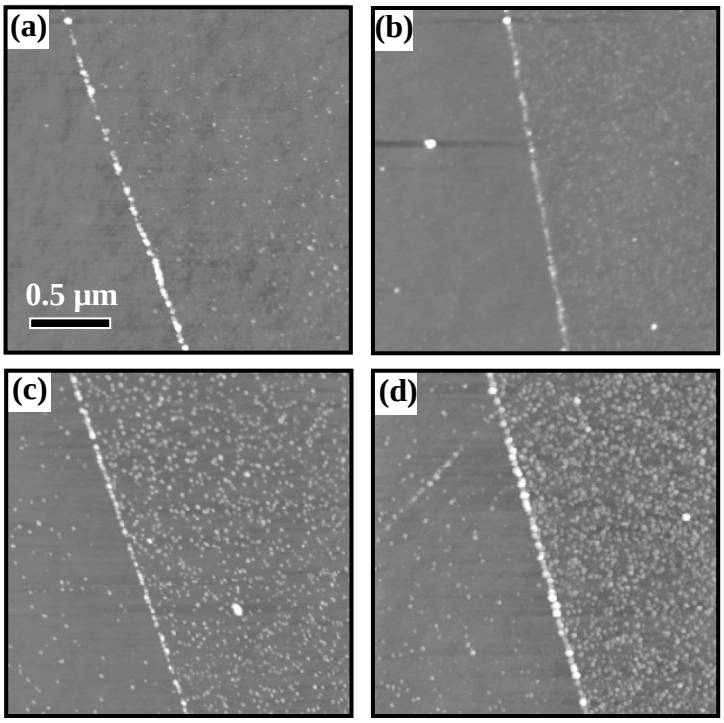


Figure 5.4 Sequence of topographic images of the MgO doped PPLT surface after 2, 4, 8, and 10 minute (a, b, c, d, respectively) irradiation times. The images indicate that silver forms on the domain boundary first and then on the positive domains.

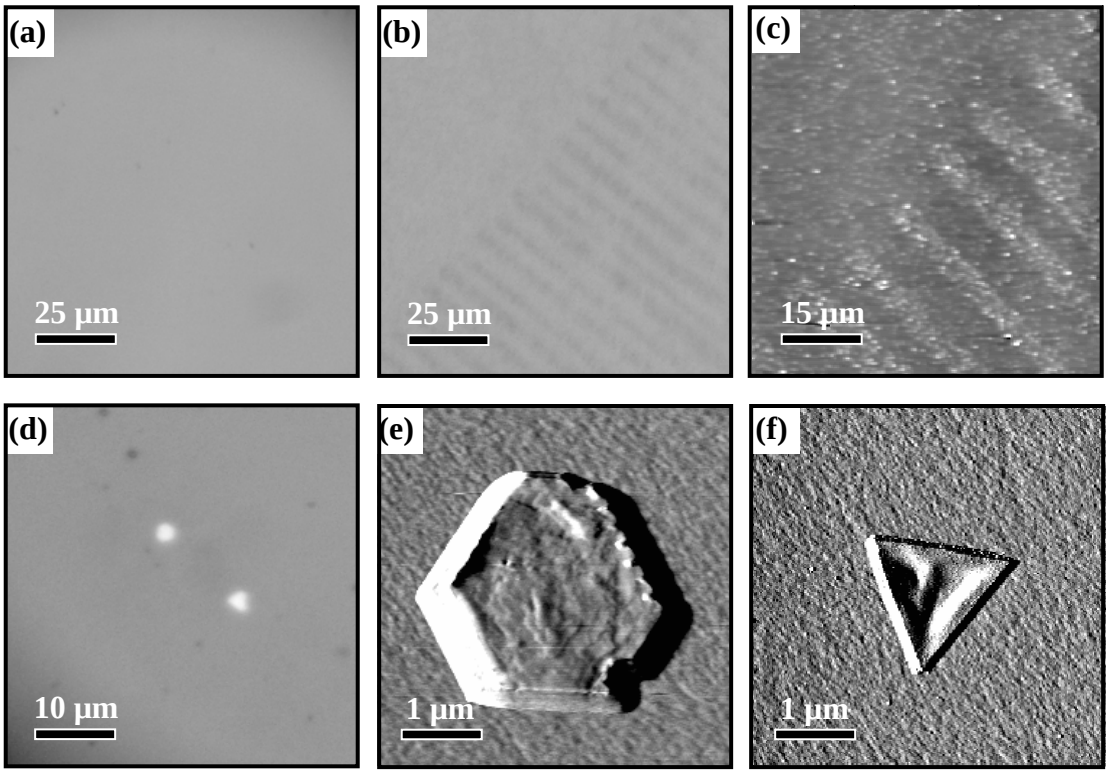


Figure 5.5 Optical microscope (a, b, and d) and AFM topographical images (c, e, and f) of gold formation on lithium tantalate surfaces. Domain specific formation of gold is evident in (b) and (c). The hexagonal (e) and triangular (f) islands that formed on the surface with the use of 0.01 M concentration $HAuCl_4$ solution are visible with the magnification of an optical microscope (d).

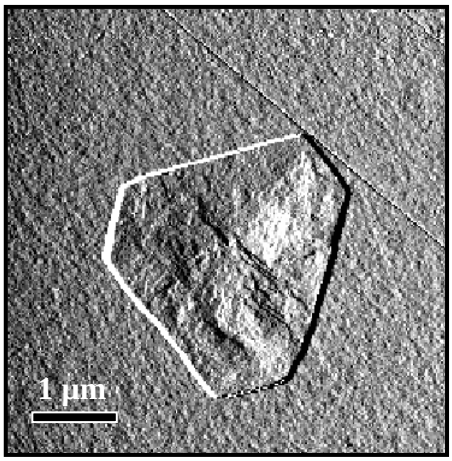


Figure 5.6 AFM topographic image of a truncated triangular island that formed on the surface of Mg:PPSLT when a 0.01 M concentration solution of $HAuCl_4$ was used for the deposition process.

6. Investigation of the Surface Potential of Periodically Poled $LiNbO_3$ Via SKPM

Jacqueline N. Hanson, [1] B. J. Rodriguez,[2] R. J. Nemanich,[3] A. Gruverman,[1] S. V. Kalinin,[2] and A. P. Baddorf[2]

[1]Department of Physics and Department of Materials Science and Engineering
North Carolina State University
Raleigh, NC 27695-8202

[2]Materials Science and Technology Division
Oak Ridge National Laboratory
Oak Ridge, TN 37831

[3]Department of Physics
Arizona State University
Tempe, AZ 85287-1504

6.1 Abstract

The surface potential of periodically poled lithium niobate (PPLN) after various surface treatments was investigated using scanning Kelvin probe microscopy (SKPM) under ambient conditions. We demonstrate the charge distribution on the surface of PPLN is responsive to surface treatments, which include solvent cleaning, etching and passivation. The results emphasize that the screening mechanism of lithium niobate is predominantly external. Additionally, the instability and screening of surface charge is demonstrated through the variance and irreproducibility of the results.

6.2 Introduction

Ferroelectric materials have unique surface properties due to the spontaneous polarization they possess. In recent years, the spontaneous polarization of ferroelectrics has been utilized as a means of achieving selective deposition on the nanoscale.[1,2] Selective deposition may be considered a promising first step in the assembly of functional complex nanostructures via a bottom up approach. In the preceding two chapters, we demonstrated the selective deposition of metals via photochemical reactions induced on the surfaces of oxygen octahedra ferroelectrics, namely, lithium niobate and lithium tantalate. The formation of silver nanowires on the domain boundaries was attributed to the inhomogeneous field distribution at the domain boundaries, which results from screening at the ferroelectric surface. It is well known that the charge associated with the spontaneous polarization must be compensated, resulting in internal and/or external screening at the surface.[3] The orientation of the spontaneous polarization determines the sign and density of the screening charges, which subsequently modify the electronic properties of the surface. In order to understand the selective deposition process on ferroelectric surfaces, it is clear that we must understand the local surface electronic properties.

Since the creation of atomic force microscopy (AFM) nearly two decades ago,[4] several scanning force microscopy (SPM)-based techniques have been developed and employed for the characterization of ferroelectric domains. These techniques include piezoresponse force microscopy (PFM),[5] electrostatic force microscopy (EFM)[6] and scanning Kelvin probe microscopy (SKPM).[7] In this work, we used SKPM as a means to study the surface potential on lithium niobate surfaces. Prior to deposition experiments,

our samples are exposed to a variety of surface treatments that are performed in an effort to reproduce initial surface conditions for each experiment. By measuring the surface potential via SKPM following surface treatments, we can gain a better understanding of the charge distribution on the surface after treatment as well as test the reproducibility of surface conditions.

6.3 Experimental Details

In this work, periodically poled lithium niobate (PPLN) substrates of congruent composition (Crystal Technologies) were used. At room temperature lithium niobate exhibits a hexagonal symmetry with polarization along the *c*-axis, which arises from the displacement of cations (Li^{+} and Nb^{5+}) with respect to oxygen planes along the *c*-axis.[8] Thus, only two domain orientations are possible in lithium niobate (antiparallel 180º domains). The periodic domain structure with a period of ~28 μm was fabricated using a lithographic mask and liquid electrodes on the +*c* face (0001) of the crystals; the electrodes were removed after poling. The samples used in this study were 3 x 3 x 0.5 mm^3 plane-parallel plates cut normal to the polar axis.

SKPM measurements were performed at Oak Ridge National Laboratory with a commercially available atomic force microscope (NanoMan V, Digital Instruments). The microscope was operated in "lift mode," in which topography and surface potential are measured independently in two steps.[9] First, the tip scans one line in tapping mode to acquire topographic information. Next, the tip is raised a predetermined height above the surface (~20-50 nm) and scans a line parallel to (and directly above) the first line to acquire information from the electrostatic interaction between the tip and sample. The

surface potential is obtained from a DC offset bias that is applied to the tip during the second scan in order to nullify the Coulomb force interaction between the tip and sample.[10] A conductive Pt-coated tip (MikroMasch, k = 7.5 N/m and f=210 kHz) was used for the measurements. Piezoresponse force microscopy (PFM) measurements were also performed to determine the polarity of domains.[5] All measurements were performed at room temperature (T=25ºC) under ambient conditions.

Preceding SKPM measurements, the PPLN samples were prepared using a variety of surface treatments (cleaning and passivation techniques). The surface treatments included the following: solvent cleaning, hydrofluoric acid (HF) etching, and trimethylchlorosilane (TMS-Cl) passivation. For the solvent cleaning, samples were immersed in acetone and placed in an ultrasonic bath to facilitate removal of loose debris from the surface; after several minutes, the process was repeated with methanol. The HF etching was performed using a HF dip that was a 48 % aqueous solution (52% DI water). Samples were immersed in the HF dip for several minutes and then rinsed in DI water in order to remove HF from the surface. Finally, TMS-Cl passivation of the surfaces was achieved by isolating the sample with a small drop (~50 μL) of liquid TMS-Cl in a covered petri dish. The TMS-Cl was allowed to evaporate and the sample was removed from the petri dish. An "as received" sample was also analyzed for comparison.

6.4 Results

The $-c$ surface of periodically poled lithium niobate as received from the manufacturer is free from topographic features corresponding to domains and/or domain boundaries. The surface of PPLN after solvent cleaning, TMS-Cl passivation and HF

etching are displayed in Fig. 6.1. Following solvent cleaning (Fig 6.1 (a) and (b)) and TMS-Cl (6.1 (c)) passivation, the surface remains free from topographic features associated with domains. Hydrofluoric acid, however, etches the +*c* and –*c* surfaces of lithium niobate at different rates (-*c* domains are etched at a faster rate).[11] Thus, the AFM topographic image in Fig. 6.1 (d) illustrates a height difference of ~50 nm between positive and negative domains after exposure to an HF dip.

Surface potential images corresponding to the topographic images of Fig. 6.1 are displayed in Fig. 6.2. The corresponding potential line profiles (Fig. 6.2 (d), (g), and (h)) show the potential difference between domains and domain boundaries is large (~several V). After passivation of the surface with TMS-Cl, domains of opposite polarity are visible in the surface potential image (Fig. 6.2 (c)). Bright contrast in the surface potential image of Fig. 6.2 (c) corresponds to negative (-*c*) domains, while dark contrast corresponds to positive domains. A potential difference of ~600 mV is indicated in the surface potential line profile of the TMS-Cl passivated surface (Fig. 6.2 (a)). Surface treatments of HF and solvent cleaning resulted in surface potential contrast at the domain boundaries only (there is no contrast between domains), as illustrated in Fig. 6.2 (d), (g), and (h). The as received sample, however, exhibited no contrast between domains and/or domain boundaries. It is clear from these results that surface potential contrast is independent of surface topography, but depends significantly on the passivation and the polarization.

6.5 Discussion

In previous studies in which the surface potential of lithium niobate was investigated with electrostatic force microscopy (EFM), a very small potential contrast (~2 mV) was observed between domains of opposite polarity at room temperature.[12,13] With heating (in vacuum), the surface potential contrast increased to several hundred mV and reversed upon cooling, indicating the presence of screening charges on the surface. UV-photoelectron emission microscopy (PEEM) experiments have also demonstrated that external screening (through the adsorption of charge molecules) is the predominant polarization screening mechanism in lithium niobate.[14] In perovskite ferroelectrics, which are screened primarily internally, contrast is observed between domains of opposite polarity under ambient conditions at room temperature.[15] Thus, it is probable that potential contrast was not observed on the surface of as received PPLN in our experiments due to the fact the surface was "dirty" and, therefore, any charge that may exist at the surface is completely screened.

HF and solvents, such as acetone and methanol, are commonly used to clean the surfaces of materials. Typically HF is used to remove (etch) oxide layers from surfaces;[16] in addition, exposure to HF is an effective method for the removal of contaminants from surfaces although it does result in a roughening of the surface. Acetone and methanol are non-destructive solvents that can be used to remove organic contaminants from surfaces. Previously (in Chapter 4 of this dissertation), we demonstrated that the electric field distribution is inhomogeneous at the domain boundaries of lithium niobate for the case of a surface that is completely screened externally (following the approach used in Ref. 15).[17] The results of SKPM on the

surface etched with HF and for solvent cleaned surfaces, which reveal little potential contrast between domains and strong potential contrast at the domain boundaries, are consistent with our calculation of the field distribution. This indicates HF and solvents effectively clean contaminants from the surface of lithium niobate. Although the bound polarization charge remains externally screened by adsorbates, there is a much smaller amount of screening at the domain boundaries due to the nonuniform field, which is revealed after surface cleaning (Fig. 6.3 (a)). Over time the surface becomes dirty again and potential contrast at the domain boundaries is reduced.

The same solvent cleaning procedure was used prior to SKPM measurements of the samples shown in Fig. 6.2 (g) and (h). Both samples exhibit potential contrast at the domain boundary, but the sign of the potential at the boundary is different. For an ideal lithium niobate surface, the potential contrast would result from the bound polarization charges; hence, domains of opposite polarity would exhibit corresponding potential with the potential crossing through zero at the domain boundary. The polarization charges must be compensated, however, in order for the crystal to maintain an energetically stable ferroelectric state.[18] The low concentration of defect states (10^{12} cm^{-2})[19] near the lithium niobate surface implies the polarization screening mechanism must be predominantly external through the adsorption of charged molecules. Thus, it is reasonable to expect little surface potential contrast between domains and a large drop in potential at domain boundaries where the electric field is nonuniform and changes sign, which is demonstrated in the surface potential images of Fig. 6.2 (e) and (g). The opposite contrast observed in Fig. 6.2 (f) and (h) indicates the charge distribution at the surface, especially at domain boundaries, is highly unstable.

Passivation of the surface with trimethylchlorosilane (TMS-Cl) is not a technique utilized to clean the surface, rather, it is a method used to form a layer of known composition on the surface. TMS-Cl is a molecule that reacts with hydroxyl groups via the reaction,[20]

$$OH + ClSi(CH_3)_3 \rightarrow OSi(CH_3)_3 + HCl_{(g)}. \quad (6.1)$$

Hydroxyl groups consist of a bond between a hydrogen atom and an oxygen atom; therefore, water is an obvious example of a hydroxyl group. In our calculation of the field distribution we assumed the adsorbate layer on the lithium niobate surface consists of mostly water.[17] Thus, the surface of lithium niobate can easily react with TMS-Cl forming a gaseous HCl product and a trimethylsilicon group that is bonded to the surface adsorbate layer (Fig. 6.3 (b)).[21] After the reaction, there should be some excess charge on the surface as some of the screening charges are removed during the reaction. This implies there should be surface potential contrast between domains of opposite polarity. Our measurements of a TMS-Cl passivated lithium niobate surface illustrate a contrast in the potential between positive and negative domains (Fig. 6.2 (c)), as expected. The bright contrast (positive potential) observed on the negative domains and dark contrast (negative potential) on the positive domains is indicative of the external screening charges on the surface. The measured potential difference of ~600 mV (Fig. 6.2 (a)) is also in agreement with our calculation of the field distribution, which predicts a potential of several hundred mV at a distance of ~50 nm above a screened lithium niobate surface.

Unfortunately, the reproducibility of the results presented above was poor. This can be explained by the fact that a large amount of charge is required to screen the

surface and the composition of the screening charge is unstable, meaning it can vary over time and with surface treatments under ambient conditions. The magnitude of the spontaneous polarization of lithium niobate is relatively large at room temperature, ~70 μC cm^{-2} compared to ~26 μC cm^{-2} for BTO.[18,22] The charge density (σ) at the surface is related to the magnitude and direction of the spontaneous polarization (P_s) via the equation,

$$\sigma = \vec{P}_s \cdot \hat{n}\,, \tag{6.2}$$

in which $\hat{n}$ is the unit vector normal to the surface. It is obvious from equation 6.2 a large number of free carriers (~10^{14} carriers cm^{-2}) is required to screen the polarization. In lithium niobate, which has a low concentration of intrinsic defects and thus a low concentration of free carriers, the majority of polarization screening is achieved externally through the adsorption of charged molecules. Consequently, the surface of lithium niobate becomes contaminated very easily under ambient conditions, as charged particles in the air are highly attracted to the charged surface.

6.6 Conclusion

In summary, SKPM was used to measure the surface potential on ferroelectric periodically poled lithium niobate after several different surface treatments that we utilize prior to deposition experiments. Our SKPM measurements were consistent with our model of the field distribution described in Chapter 4. The results emphasized the external screening mechanism of lithium niobate as well as the instability of the charge distribution on the surface under ambient conditions.

6. References

[1] S. V. Kalinin, D. A. Bonnell, T. Alvarez, X. Lei, Z. Hu, J. H. Ferris, Q. Zhang, and S. Dunn, Nano Lett. **2**, 589 (2002).

[2] J. L. Giocondi and G. S. Rohrer, Chem. Mater. **13**, 241 (2001).

[3] V. M. Fridkin, *Ferroelectric Semiconductors* (Consultants Bureau, New York, 1980).

[4] G. Binnig, C. F. Quate, and C. Gerber, Phys. Rev. Lett. **56**, 930 (1986).

[5] A. Gruverman, O. Auciello and H. Tokumoto, Ann. Rev. of Mat. Sci. **28,** 101 (1998).

[6] Y. Leng and C. C. Williams, Coll. Suf. A **93**, 335 (1994).

[7] M. Nonnenmacher, M. P. O'Boyle, and H. K. Wickramasinghe, Appl. Phys. Lett. **58**, 2921 (1991).

[8] S. C. Abrahams, H. J. Levinstein, and J. M. Reddy, J. Phys. Chem. Solids **27**, 1019 (1966).

[9] V. Elings and J. Gurley, US Patent Nos. 5,266,801 and 5,308,974, Digital Instruments, Santa Barbara, CA

[10] H. O. Jacobs, H. F. Knapp, S. Muller and A. Stemmer, Ultramicroscopy **69**, 39 (1997).

[11] C. L. Sones, S. Mailis, W. S. Brocklesby, R. W. Eason, and J. R. Owen, J. Mater. Chem. **12**, 295 (2002).

[12] X. Liu, K. Kitamura, and K. Terabe, Appl. Phys. Lett. **89**, 132905 (2006).

[13] D. A. Scrymgeour and V. Gopalan, Phys. Rev. B **72**, 024103 (2005).

[14] W.-C. Yang, B. J. Rodriguez, A. Gruverman, and R. J. Nemanich, Appl. Phys. Lett. **85**, 2316 (2004).

[15] S. V. Kalinin and D. A. Bonnell, Phys. Rev. B **63**, 125411 (2001).

[16] T. Deegan and G. Huges, Appl. Surf. Sci. **123-124**, 66 (1998).

[17] J. N. Hanson, B. J. Rodriguez, R. J. Nemanich, and A. Gruverman, Nanotechnology **17**, 4946 (2006).

[18] M. E. Lines and A. M. Glass, *Principles and Applications of Ferroelectrics and Related Materials* (Oxford, New York, 1977).

[19] A. M. Prokhorov and Yu. S. Kuz'minov, *Physics and Chemistry of Crystalline Lithium Niobate* (Taylor and Francis, 1990).

[20] X. S. Zhao and G. Z. Lu, J. Phys. Chem. B **102**, 1556 (1998).

[21] R. C. Anderson, R. S. Muller, and C. W. Tobias, J. Electrochem. Soc. **140**, 1393 (1993).

[22] S. V. Kalinin, C. Y. Johnson, and D. A. Bonnell, J. Appl. Phys. **91**, 3816 (2002).

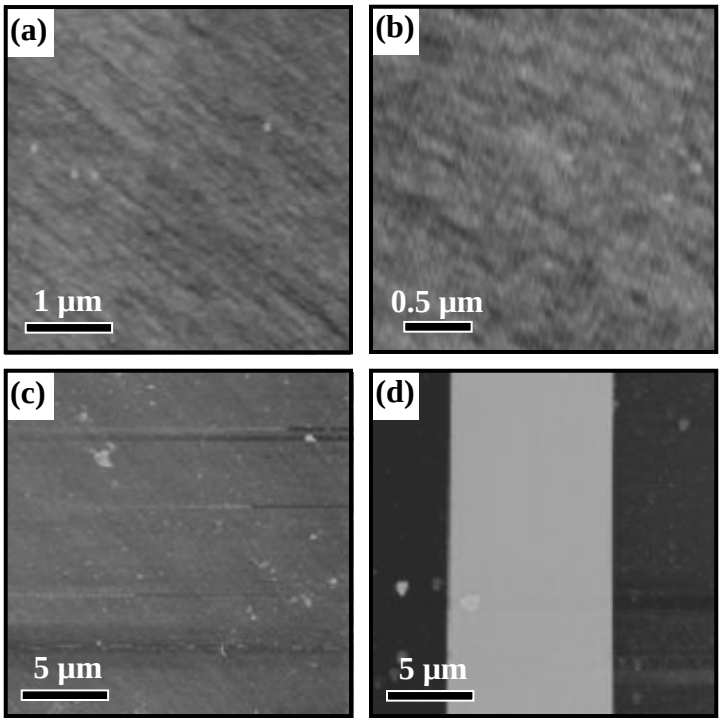


Figure 6.1 AFM topographic images of PPLN surfaces after the following surface treatments: solvent cleaning (a, b), TMS-Cl passivation (c) and an HF dip (d). After solvent cleaning and TMS-Cl passivation, there are no apparent surface features associated with domains and/or domain boundaries. The *–c* surface of lithium niobate is etched with HF, resulting in a height difference of ~50 nm between antiparallel domains. (Note: these images correspond to the surface potential images in Fig. 6.2.)

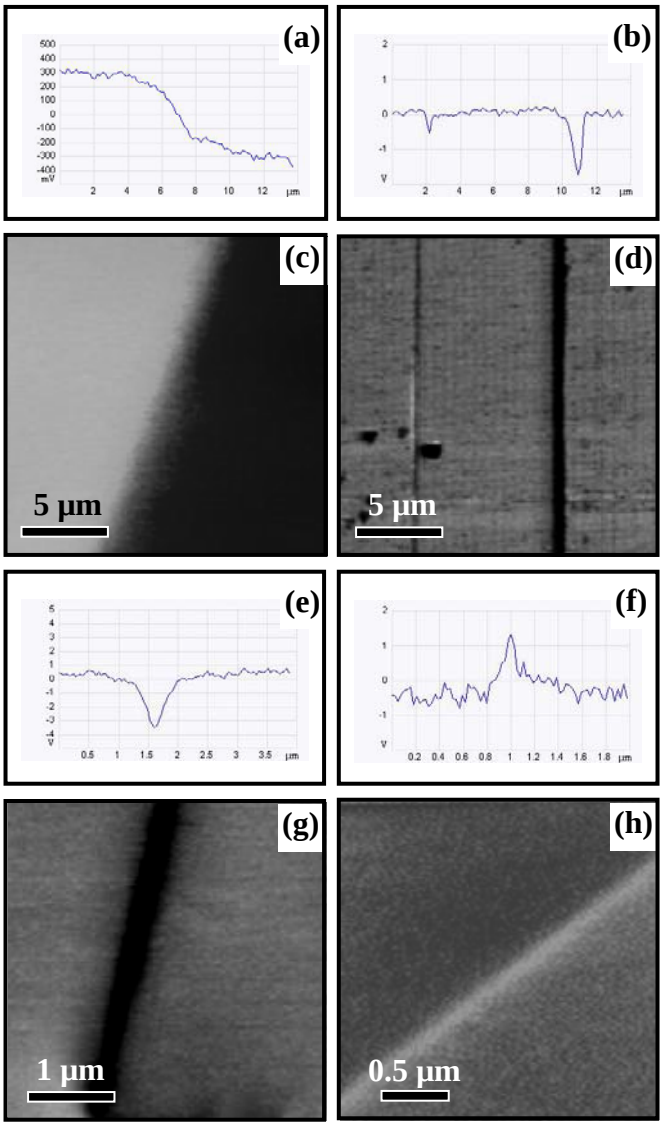


Figure 6.2 (c, d, g, h) SKPM potential images of lithium niobate surfaces after various surface treatments and (a, b, g, h) corresponding line profiles of the surface potential contrast across a domain boundary. The surface in (a, c) was passivated with TMS-Cl and (b, d) shows the surface after HF etching. The surfaces in (e, g) and (f, h) were cleaned with solvents.

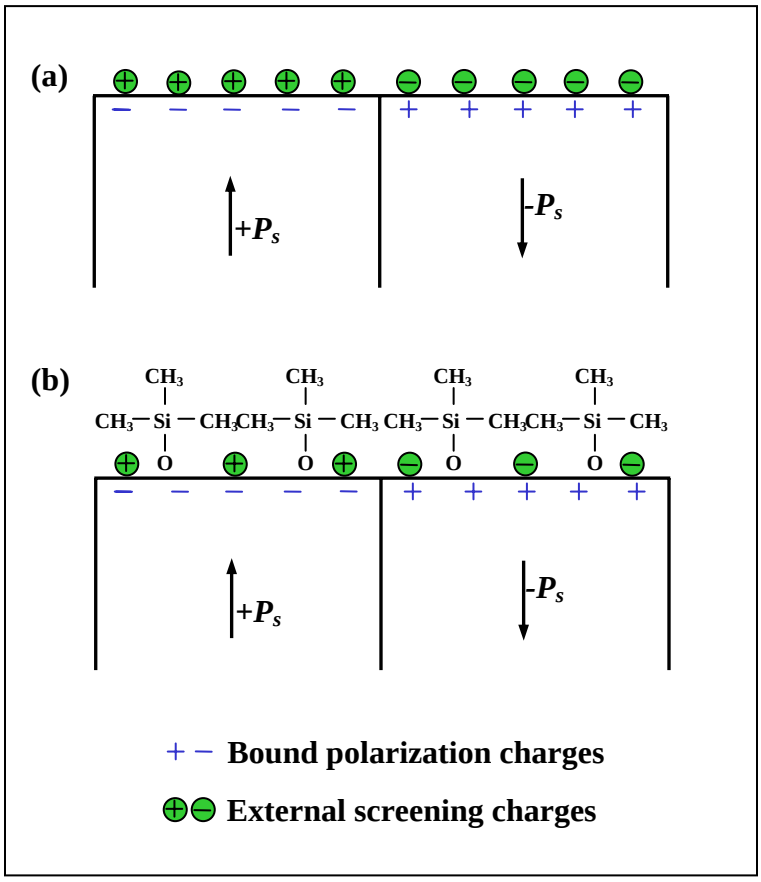


Figure 6.3 Schematic of the screening charges on the surface of lithium niobate after solvent cleaning (a) and after passivation with TMS-Cl (b).

7. Selective Molecular Adsorption on a Domain Patterned Ferroelectric Template

Jacqueline N. Hanson,[1] A. Gruverman,[1] and R. J. Nemanich[2]

[1]Department of Physics and Department of Materials Science and Engineering
North Carolina State University
Raleigh, NC 27695-8202

[2]Department of Physics
Arizona State University
Tempe, AZ 85287-1504

7.1 Abstract

The domain specific deposition of two polar molecules, stearic acid and evans blue dye, on periodically poled lithium niobate (PPLN) substrates is presented. We demonstrate a vapor deposition technique for stearic acid and a solution based deposition technique for the evans blue dye molecule. In both cases, the negative charge of the polar molecules is attracted to the positive domains of lithium niobate; thus, adsorption of the molecules begins on the positive domains. With increased exposure time to the stearic acid vapor, the entire PPLN surface is passivated with stearic acid. Upon UV irradiation of the passivated surface, photogenerated holes from the PPLN induce the decomposition of the stearic acid molecules on the surface. This process is most noticeable at the domain boundaries. X-ray photoelectron spectroscopy (XPS) data of single domain lithium niobate, which indicates the preference of evans blue dye molecules to adsorb on the surface of positive domains, is also presented.

7.2 Introduction

Ferroelectric materials possess many unique properties, the most outstanding of which is the presence of a reversible spontaneous polarization. The charge associated with the spontaneous polarization must be compensated at the surface (internally and/or externally) in order for the material to maintain an energetically stable state.[1] With a value of ~78 μC cm^{-2}, the spontaneous polarization of lithium niobate has one of the largest known magnitudes at room temperature.[2] Since the charge density at the surface is proportional to the spontaneous polarization, this implies there is a large amount of charge that requires compensation. In the preceding chapters, we have shown the bound polarization charge of lithium niobate is screened predominantly externally; thus, the external screening layer that forms on lithium niobate surfaces is dependent upon the composition of the environment outside of the crystal. The ability to reverse the polarization and create domain patterns combined with the unique electronic properties of the surface make ferroelectrics an ideal template for a bottom-up approach to the assembly of complex nanostructures.[3]

In this study, we demonstrate two techniques for the preferential deposition of polar molecules on periodically poled lithium niobate. First, we present a vapor deposition technique in which the surface of a lithium niobate crystal is exposed to stearic acid vapor. The stearic acid molecules adsorb to positive domains first and then passivate the entire surface over time. We also demonstrate selectivity of the decomposition of stearic acid molecules on lithium niobate. Illumination with UV light excites electron-hole pairs within the lithium niobate crystal which combine with stearic acid molecules adsorbed on the surface, inducing decomposition. The decomposition is

primarily observed at domain boundaries, which analogous to the formation of silver nanowires at the domain boundaries.[4]

The second technique we present is a solution-based method for selective deposition. We demonstrate the preferential adsorption of evans blue dye molecules by employing the pyroelectric nature of lithium niobate in a controlled environment (solution). Evans blue dye is a polyionic molecule with several anions that may be attracted to the positive domains of lithium niobate; this is illustrated with the adsorption of evans blue dye to positive domains via our solution-based technique. Selective adsorption of evans blue dye is also confirmed with x-ray photoelectron spectroscopy (XPS) data of single domain samples.

7.3 Stearic Acid

7.3.1 Experimental Details

Periodically poled lithium niobate (PPLN) substrates of congruent composition (Crystal Technologies) were used for these experiments. At room temperature lithium niobate exhibits a hexagonal symmetry with polarization along the *c*-axis, which arises from the displacement of cations (Li^+ and Nb^{5+}) with respect to oxygen planes along the *c*-axis in the ferroelectric phase.[5] Thus, only two domain orientations are possible in lithium niobate crystals (antiparallel 180º domains). The samples used in this study were 3 x 3 x 0.5 mm^3 plane-parallel plates cut normal to the polar axis. The periodic domain structure, which has a period of ~28 μm, was fabricated using a lithographic mask and liquid electrodes on the +*c* face (0001) of the crystals; the electrodes were removed after

poling. A Pt-coated tip (MikroMasch, k = 5 N/m) was used for visualization of the domain patterns by means of piezoresponse force microscopy (PFM).[6]

Prior to all deposition experiments, samples were immersed in acetone and placed in an ultrasonic bath to facilitate removal of loose debris from the surface; after several minutes the sample was removed and the process was repeated with methanol. Stearic acid powder was added to a small glass crucible with a depth of ~1.5 cm and placed on a hot plate which was then set to 180ºC (well above its melting point of ~70ºC).[7] The PPLN sample was attached to the center of a glass slide with double-sided tape. Once the hot plate reached 180ºC the sample was positioned over the liquefied stearic acid and the system was covered with a large petri dish in order to shield the system from air circulating in the chemical fume hood (see Fig. 7.1). Samples were exposed to the vapor for various lengths of time ranging from 30 seconds to 3 minutes. After exposure, samples were allowed to cool for several minutes and subsequently removed from the glass slide. The samples were then imaged with an atomic force microscope (AFM) operated in tapping-mode in order to preserve any structures that had formed on the surface. A pen lamp with predominant emission at 254 nm was used as a source of UV illumination. According to the manufacturer's specifications, the power density at a distance of 2 cm (the distance between the light source and sample) from the lamp is ~1-4 mW/cm^2.

A model of a stearic acid ($CH_3(CH_2)_{16}COOH$) molecule is illustrated in Fig. 7.2. Stearic acid is composed of a hydrocarbon chain with a methyl group at one end and a carboxyl group at the opposite end; thus, it has two major components: a hydrocarbon-like chain, which is non-polar and therefore hydrophobic, and a carboxyl group, which is

polar and therefore hydrophilic. It is the polar end of the molecule that is expected to adsorb to the charged surface of lithium niobate.

7.3.2 Results and Discussion

The optical microscope image in Fig. 7.3 (a) shows the surface of PPLN after a one minute exposure to stearic acid vapor. The +*c* domains are highlighted in the image by irregular shaped islands of stearic acid that are up to 10 μm in width. Elongated islands extend along the length of domains (rather than across several domains). The deposition of stearic acid on +*c* domains was also confirmed by PFM. It is clear from the topographic image in Fig. 7.3 (b) that there are layers of stearic acid on the sample and further magnification (Fig. 7.3 (c)) reveals the layers are composed of small islands. The stearic acid layers on the sample range from 4 nm to 20 nm in height; this corresponds to ~2-8 monolayers of fully extended stearic acid molecules (the fully extended length is ~2.5 nm).[8]

In a previous study by Giocondi and Rohrer, deposition of stearic acid from the vapor phase onto a $BaTiO_3$ (BTO) substrate resulted in the formation of irregular shaped islands on the surface,[8] similar to our experiment. The islands on BTO, however, did not form in a pattern specific to the underlying domain configuration. Giocondi and Rohrer heated the stearic acid powder to 85ºC, which is almost 100ºC less than the temperature of our stearic acid. This implies stearic acid was evaporating at a greater rate in our experiments, thus there was a significantly greater flux of stearic acid molecules.

In pyroelectric crystals such as lithium niobate and barium titanate, a change in temperature causes a change in the spontaneous polarization, which in turn, results in an

excess of free charges at the surface of the material.[9] For example, the magnitude of the spontaneous polarization will decrease with an increase temperature creating an excess of negative charge at the $+c$ surface. With lithium niobate, in which the polarization screening mechanism is predominantly external, the excess adsorbed negative charge can leave the surface. It is possible then, that the temperature of the sample increased resulting in a decrease in the spontaneous polarization and the subsequent decrease in the concentration of screening charges. It is unlikely, however, that this was the mechanism by which stearic acid selectively adsorbed on the surface. Because the temperature of the sample was increasing during exposure to stearic acid vapor, stearic acid molecules would have been attracted to excess positive charge on negative domains. A more likely scenario is as follows: the high temperature (180ºC) of the system could have caused some of the water molecules in the adsorbate layer on the lithium niobate surface to evaporate (desorb) from the surface[10] leaving the bound polarization charge temporarily unscreened. In this case, stearic acid molecules could have been attracted to positive domains that required screening. This also explains the lack of selectivity in Giocondi and Rohrer's experiment.

Several studies have explored the photodecomposition of stearic acid on substrates such as $BaTiO_3$,[8] TiO_2[11,12] and even water.[7] Over time, the entire surface of PPLN is passivated with layers of stearic acid molecules (Fig. 7.4 (a) and (b)), thus we investigated the photodecomposition of stearic acid on PPLN. The AFM topographic image in Fig. 7.4 (c) shows the passivated surface after exposure to UV light (254 nm) for ~60 minutes. There are trenches at the domain boundaries with a depth of ~16 nm. There are two possible mechanisms for the photodecomposition of stearic acid.[13] In the

first mechanism, hydroxide ions combine with photogenerated holes and hydroxyl radicals are produced:

$$OH^- + h^+ \rightarrow OH^\bullet . \tag{7.1}$$

Hydroxyl radical are able to migrate on the surface and they can react with stearic acid molecules or produce other oxidizing species that are capable of migration, thus the reaction with stearic acid may not occur at the location where the hole is generated. In the second mechanism, photogenerated holes combine directly with stearic acid molecules via the reaction:

$$C_{17}H_{35}COOH + h^+ \rightarrow C_{17}H_{35}COO^\bullet + H^+ . \tag{7.2}$$

It is likely that stearic acid is decomposed by both oxidation mechanisms since the entire passivation layer has changed form as evident from the difference in surface topography in Fig. 7.4 (b) and (c). Eventually the stearic acid is completely decomposed into CO_2 and H_2O.[14] The fact that the domain boundaries are free of stearic acid after UV illumination is consistent with our model for photochemical reactions at the surface of lithium niobate, which was presented in Chapter 4.

Due to a lack of control over stearic acid adsorption on the surface, this exact result could not be repeated. The ability to decompose stearic acid films via photo-oxidation on the surface of lithium niobate was reproducible, however.

7.4 Evans Blue Dye Molecule

7.4.1 Experimental Details

The same congruent periodically poled lithium niobate samples described in Section 7.3.1 were used for the evans blue dye molecule experiments. In addition, 3 x 3 x 0.5 mm^3 substrates (cut normal to the polar axis) of single domain lithium niobate (LN) of congruent composition were used. Prior to all deposition experiments, samples were cleaned following the solvent cleaning procedure described in Section 7.3.1. After cleaning, the sample was placed in a beaker and covered with ~10 mL of a 1.0 mM solution of evans blue dye dissolved in deionized water or anhydrous methanol. The beaker was then placed on a pre-heated hot plate at 50ºC for 15 minutes. The beaker was removed from the hot plate and the sample was allowed to cool in the solution for an additional 15 minutes. The sample was rinsed with deionized water or anhydrous methanol (depending on the solution that was used) and then blown dry with nitrogen. Once dry, the samples were imaged with an atomic force microscope (AFM) operated in tapping-mode in order to preserve any structures that had formed on the surface or analyzed with x-ray photoelectron spectroscopy (XPS). XPS was performed at a pressure of $2x10^{-9}$ using the 1253.6 eV Mg *K* line from a VG Microtech XR3 dual anode source and a VG Microtech Clam II electron analyzer.[15]

A model of an evans blue dye molecule ($C_{34}H_{24}N_6Na_4O_{14}S_4$) is illustrated in Fig. 7.5. Evans blue dye is a polyionic molecule, as can be seen from the four anions (SO_3^-) shown in the model. It is expected at least one of these anions will be attracted to the surface of positive domains, as anions possess a net negative charge.

7.4.2 Results and Discussion

The AFM topographic image of the PPLN surface before evans blue dye deposition (Fig. 7.6 (a)) shows no apparent surface features associated with the domain structure. After exposure to the evans blue dye solution, there is contrast between domains of opposite polarity (Fig. 7.6 (b)). Unfortunately, the height difference between domains is within the noise range (in the *z* direction) of our AFM, thus an accurate height measure could not be obtained. Subsequent imaging of the sample with PFM revealed the dye molecules were located on the positive domains. Reproducibility of this result was poor on PPLN samples. However, we were able to demonstrate the adsorption of evans blue dye on single domain lithium niobate samples.

Positive and negative faces of single domain lithium niobate were exposed to the same deposition procedure as the PPLN sample. Immediately after the sample was dry, it was analyzed with XPS. XPS data is displayed in Fig. 7.7. The spectra in Fig. 7.7 (a), which correspond to the +*c* face of lithium niobate, indicate there is sulfur present on the surface. The spectra in Fig. 7.7 (b) corresponding to the –*c* face of lithium niobate does not contain a sulfur peak. The anions associated with evans blue dye contain sulfur (SO_3^-); thus, it can be inferred from this data that evans blue dye adsorbed only on positive domains.

The pyroelectric nature of lithium niobate was discussed in Section 7.3.2. Although, this deposition was performed at an elevated temperature (50ºC) the magnitude of the spontaneous polarization probably didn't change a significant amount since the temperature difference was only ~25ºC. On the other hand, the kinetic energy of the ions

in the solution increases with an increase in temperature resulting in a greater number of collisions with the surface.[16] An increase in velocity also implies an increase in momentum, thus the ions collide with surface with a greater impact. Evans blue dye is by far the heaviest molecule used for deposition experiments in this research (molar mass = 960.809 g mol^{-1}). As we have demonstrated, the screening charges at the surface are unstable; therefore, it is possible the impact of evans blue dye at the surface could shift screening charges and replace them.

Additionally, we found the polarity of the solvent affects the deposition outcome. Deposition on positive domains was not observed when water was used as the solvent in the solution. When anhydrous methanol, which is less polar than water, was used as the solvent, deposition was observed on the positive domains. It is possible that the polar molecules in water screened the charge at the surface due to the formation of an electric double layer.[17]

7.5 Conclusion

In summary, we have demonstrated the directed assembly of polar molecules on the surface of congruent lithium niobate via a vapor deposition technique and a solution-based method. As expected, both of the polar molecules were attracted to the positive domains. It is clear thermal properties of the sample and solution affected the deposition process in both cases. We also found the polarity of the solvent used in the solution can inhibit the deposition of molecules on the surface. UV illumination the surface of lithium niobate passivated with thick films of stearic acid can induce photodecomposition of the

films. Preferential decomposition at the domain boundaries confirms our model for the mechanism of photochemical reactions on lithium niobate surfaces.

7.6 Acknowledgements

The authors would like to thank Jiyoung Choung for characterization of lithium niobate samples via XPS performed for this study.

7.7 References

[1] V. M. Fridkin, *Ferroelectric Semiconductors* (Consultants Bureau, New York, 1980).

[2] S. Ganesamoorthy, M. Nakamura, S. Takekawa, S. Kumaragurubaran, K. Terabe, and K. Kitamura, Mater. Sci. Eng. B **120**, 125 (2005).

[3] S. V. Kalinin, D. A. Bonnell, T. Alvarez, X. Lei, Z. Hu, and J. H. Ferris, Nano Lett. **2**, 589 (2002).

[4] J. N. Hanson, B. J. Rodriguez, R. J. Nemanich, and A. Gruverman, Nanotechnology **17**, 4946 (2006).

[5] S. C. Abrahams, H. J. Levinstein, and J. M. Reddy, J. Phys. Chem. Solids **27**, 1019 (1966).

[6] A. Gruverman, O. Auciello and H. Tokumoto, Ann. Rev. of Mat. Sci. **28,** 101 (1998).

[7] N. Pilpel and B. F. J. Hunter, J. Colloid Interface Sci. **33**, 615 (1970).

[8] J. L. Giocondi and G. S. Rohrer, Mat. Res. Soc. Symp. Proc. **654**, AA7.4 (2001).

[9] J. F. Nye, *Physical Properties of Crystals Their Representation by Tensors and Matrices* (Oxford, London, 1957).

[10] C. E. Nelson, J. W. Elam, M. A. Cameron, M. A. Tolbert, and S. M. George, Surf. Sci. **416**, 341 (1998).

[11] K. Kobayashi, Y. Tomita, K. Matsuhisa, and Y. Doi, Appl. Surf. Sci. **244**, 389 (2005).

[12] P. Sawunyama, A. Fujishima, and K. Hashimoto, Langmuir **15**, 3551 (1999).

[13] M. Schiavello, Electrochimica Acta **38**, 11 (1993).

[14] S. Sitkiewitz and A. Heller, New J. Chem. **20**, 233 (1996).

[15] C. C. Fulton, G. Lucovsky, and R. J. Nemanich, J. Appl. Phys. **99**, 063708 (2006).

[16] T. L. Brown, H. E. LeMay, and B. E. Bursten, *Chemistry: The Central Science* (Prentice Hall, New Jersey, 2000).

[17] N. Sato, *Electrochemistry at Metal and Semiconductor Electrodes* (Elsevier, New York, 1998).

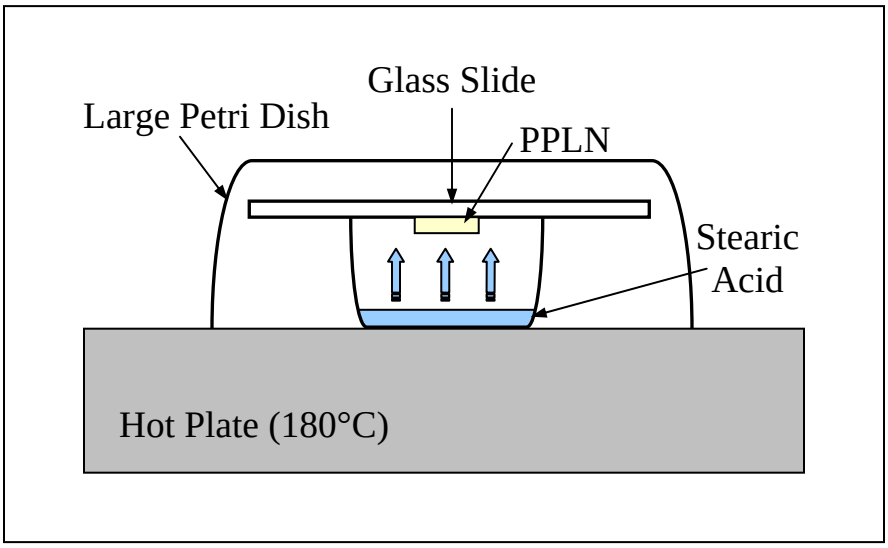


Figure 7.1 Diagram of the stearic acid vapor deposition setup. The stearic acid is melted in a small glass crucible. The PPLN sample is attached to the glass slide with double-sided tape. (Note: the objects in this diagram are not to scale.)

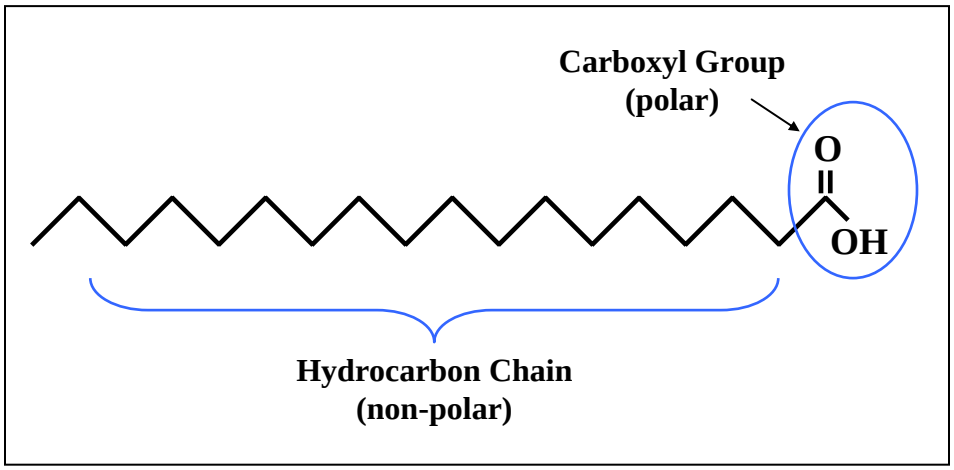


Figure 7.2 Stearic acid molecule. Due to the difference in the electronegativity of its atoms, the carboxyl group (COOH) is polar (oxygen has a net negative charge). As there are no double carbon bonds, the hydrocarbon chain is flexible.

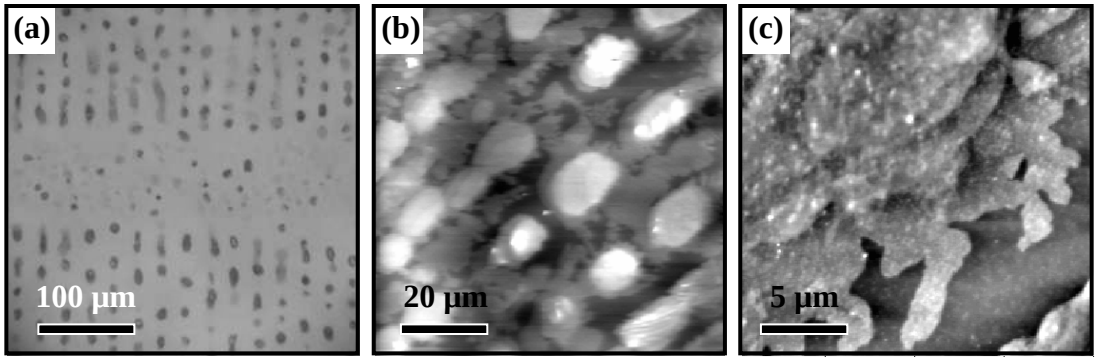


Figure 7.3 Images of a PPLN surface after exposure to stearic acid vapor. Domain contrast is apparent in the optical microscope image (a). There is a gap of ~95 µm between regions of periodically poled domains which is also visible in (a). AFM topographic images (b, c) indicate there is an average height difference of ~12 nm between domains of opposite polarity. The highest magnification image (c) shows the large islands that are visible in the optical microscope image (a) are composed of smaller islands.

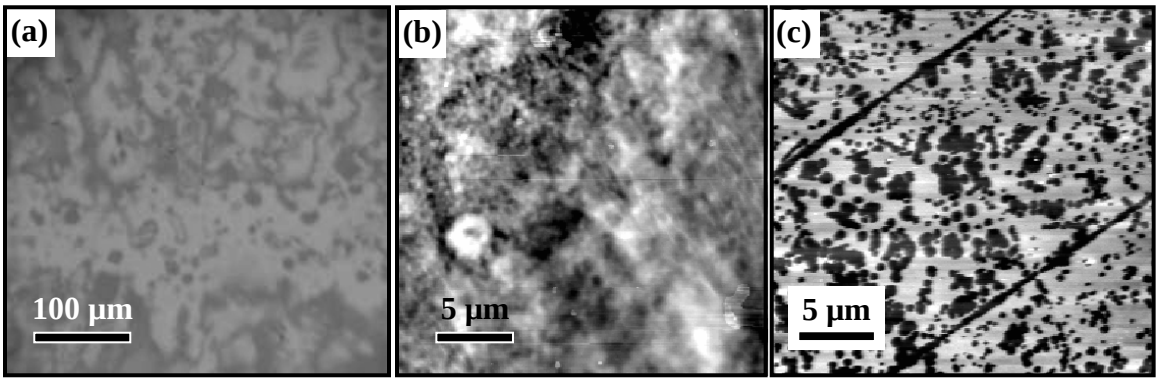


Figure 7.4 Images of a PPLN surface after exposure to stearic acid vapor. After a longer exposure time, domain contrast is no longer visible in the optical microscope image (a). The AFM topographic image in (a) shows the surface is covered with stearic acid. Domain boundaries are visible in the topographic image (c) after the stearic acid covered surface is illuminated with UV light.

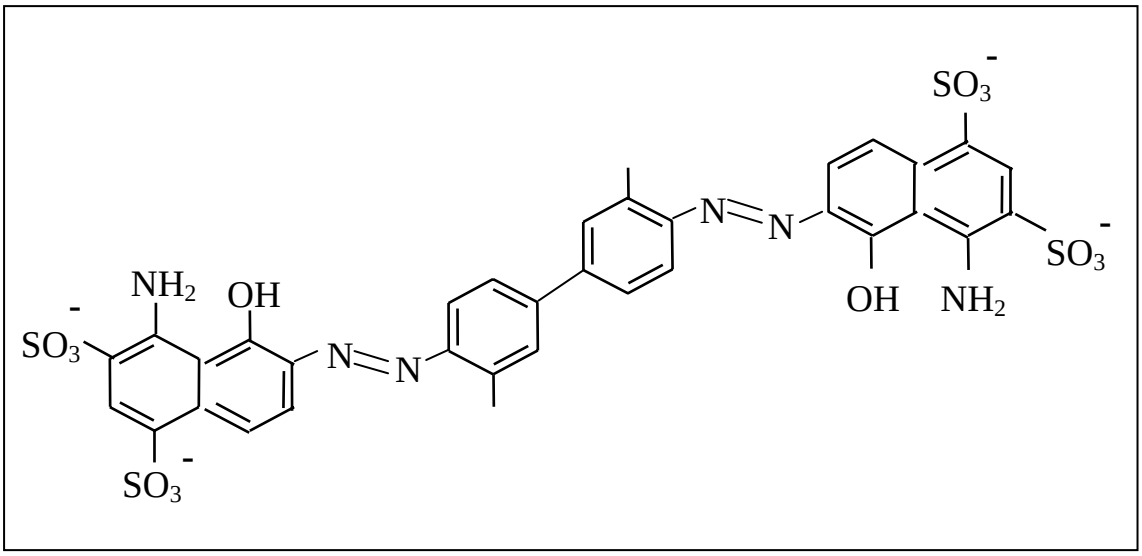


Figure 7.5 Model of an evans blue dye molecule. This molecule has four anions (SO_3^-), making it a polyionic molecule.

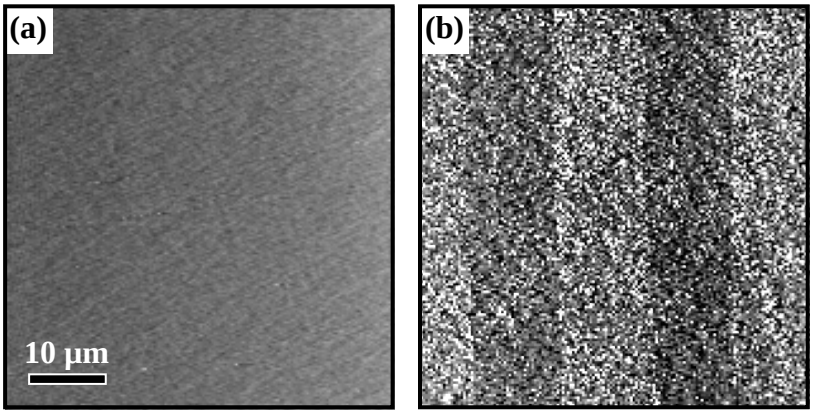


Figure 7.6 There is no apparent domain contrast visible in the topographic image before deposition of evans blue dye molecules. After deposition, there is contrast between domains (b). The +*c* domains are ~5 nm taller than –*c* domains.

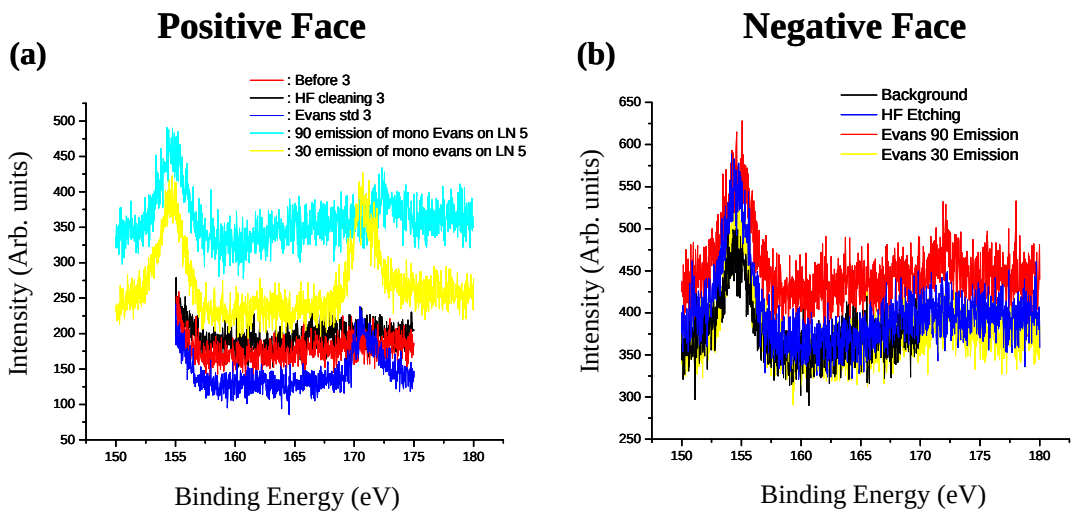


Figure 7.7 XPS data of evans blue dye adsorbed on positive (a) and negative (b) domains of single domain lithium niobate.

8. Summary and Future Work

8.1 Summary

In summary, we presented several techniques for selective deposition/adsorption on lithium niobate and lithium tantalate surfaces as well as a study of the charge distribution on the surface of lithium niobate. First, mathematical backgrounds of ferroelectric materials and scanning probe microscopy (SPM) techniques were given as a basis for understanding the SPM methods utilized and the results obtained in this research. In addition, specific properties of lithium niobate and lithium tantalate were discussed. In Chapter 4, a method for the fabrication of silver nanowires via photoreduction on lithium niobate was introduced. The field distribution of lithium niobate was calculated under the assumption of complete external screening and a model for the formation of silver on the domain boundaries was described. We extended our model to the selective photoreduction of silver and gold on lithium tantalate surfaces in Chapter 5. The differences in reactivity were attributed to composition (stoichiometry and doping) of the materials as well as variations in electronic properties. To gain a better understanding of the surface of lithium niobate, scanning Kelvin probe microscopy (SKPM) experiments were implemented. The irreproducibility of the results of the study emphasized the external screening mechanism of lithium niobate and also demonstrated the instability and screening of surface charge. Techniques for selective molecular adsorption were presented in Chapter 7. Stearic acid molecules were deposited on the sample from the vapor phase, while evans blue dye molecules were deposited from solution. The

pyroelectric nature of lithium niobate was utilized in both techniques. Furthermore, UV illumination of a lithium niobate sample completely passivated with stearic acid resulted in photodecomposition of the stearic acid and trenches formed at the domain boundaries. This was in agreement with our model for photochemical processes on the ferroelectric surfaces.

8.2 Future Work

This study has provided many opportunities for prospective experiments, the results of which may be significant in the future development of nanostructures and devices. Some of the possibilities are presented in the following sections.

8.2.1 $HAuCl_4$ Experiments

Size and shape control is important in the synthesis of nanoscale materials. As demonstrated in Chapter 5, the use of $HAuCl_4$ (gold chloride) in UV illumination experiments led to an unexpected result, the formation of gold nanoplates. Previous studies have reported the precipitation of hexagonal and triangular gold (111) nanoplates from solutions containing a reducing agent.[1] Kalinin *et al*. observed the formation of similar structures with the use of gold chloride in photochemical deposition experiments on perovskite ferroelectrics, though a detailed explanation of the formation mechanism was not provided.[2]

Characterization experiments such as x-ray photoelectron spectroscopy (XPS) and x-ray diffraction need to be performed in order to determine the true composition and crystal structure of the islands. This may be a new method, which is simple to implement

and cost effective, for the fabrication of nanoplates of specific size and shape. Since we know selective photoreduction/oxidation is possible, a method for a predetermined pattern of nanoplates may be obtainable with proper experimental conditions (photon energy, solution concentration, etc.).

Furthermore, the possibility of making gold nanowires via this process should be further explored. It is obvious selective photoreduction of gold can be achieved, but experimental parameters (time, temperature, solution concentration, etc.) of the process may need modification. Due to their much slower rate of oxidation, gold nanowires are more desirable than silver nanowires for certain applications.

8.2.2 Deposition in a Controlled Environment

In this work, have observed the instability of the surface charges on lithium niobate under ambient conditions over and over. It is very clear the surface of lithium niobate is very sensitive to its environment. Thus, in order to obtain the same, predictable surface conditions for every experiment, it may be necessary to perform the experiments in a controlled environment.

One possibility is to clean and perform deposition experiments in vacuum or a controlled gas environment. This way, the surface contamination can be kept to a minimum resulting in better reproducibility of surface conditions. In addition, polar molecules may be introduced in the form of gas or vapor. If there are no particulates in the environment competing to screen the charge at the surface, there is an increased probability for domain selective deposition to occur, especially if the pyroelectric nature of the ferroelectric material is exercised.

Another possibility is to write domain patterns in a liquid/solution environment. Rodriguez *et al*. recently demonstrated piezoresponse force microscopy (PFM) in distilled water and NaCl solutions,[3] indicating electromechanical measurements are possible in a liquid environment. Therefore, it may also be possible to reverse the spontaneous polarization of ferroelectrics in a liquid environment. Upon reversal of the spontaneous polarization, adsorbed screening charges leave the surface and charges of the opposite sign take their place. If polar molecules of the appropriate sign were present in the solution at the time of polarization reversal, it is possible they may take the place of the desorbed screening charges resulting in selective deposition of the polar molecules.

8.3 References

[1] H. Chen, J. Jia, and S. Dong, Nanotechnology **18**, 245601 (2007).

[2] S. V. Kalinin, D. A. Bonnell, T. Alvarez, X. Lei, Z. Hu, and J. H. Ferris, Nano Lett. **2**, 589 (2002).

[3] B. J. Rodriguez, S. Jesse, A. P. Baddorf, and S. V. Kalinin, Phys. Rev. Lett. **96**, 237602 (2006).